A CIRCULAR ECONOMY APPROACH - POST-CONSUMER TEXTILE WASTE RECYCLING FOR 3D PRINTING FLEXIBLE TEXTILES

HU LINGQUAN

PhD

The Hong Kong Polytechnic University

2024

The Hong Kong Polytechnic University

School of Fashion and Textiles

A Circular Economy Approach - Post-consumer Textile Waste Recycling for 3D Printing Flexible Textiles

HU Lingquan

A thesis submitted in partial fulfillment of the requirements for the degree of Doctor of Philosophy

August 2023

CERTIFICATE OF ORIGINALITY

I hereby declare that this thesis is my own work and that, to the best of my knowledge and belief, it reproduces no material previously published or written, nor material that has been accepted for the award of any other degree or diploma, except where due acknowledgement has been made in the text.

_____ (Signed)

HU Lingquan (Name of student)

Abstract

Three-dimensional (3D) printing filament has recently been producing by using recycled materials from 3D printing waste and other sources. With the developments of material recycling processes, a new source referred to as post-consumer textile waste (PCTW) can be used to produce filaments for 3D printing textiles. However, several challenges impede thermoplastic recycling from PCTW for 3D printing. The flowability of the polyester recycled from PCTW is too high to be extruded into 3D-printable filaments, which must be adjusted by additives. The mechanical method is rarely investigated for recycling thermoplastic polyurethane (TPU) films into 3D-printable filaments. Moreover, the development of 3D-printable filaments is restricted by limited applications, which should be expanded to encourage polyester textile and TPU film recycling. To address these challenges, this thesis investigates the material properties of polyester and TPU recycled from polyester textiles and TPU films. It also discusses the potential applications of polyester and recycled TPU (rTPU) filaments for 3D printing textiles.

In this study, the clean textiles were hot-pressed into a paper-thin plastic board. After air-cooling, the plastic board was ground with ADR 4468 into powders. The extruder mixed, melted, and shaped the powder into 3D printing filaments. The polyester filaments were printed into specimens for further tests to improve the mechanical properties of materials and then printed into textiles with different structures to enhance flexibility. TPU film recycling is accomplished by breaking the

film into plastic fragments, which are then extruded into filaments. After 3D printing, the specimens were tested to improve the mechanical properties of materials, and the textiles with distinct structures were tested to enhance flexibility.

The polyester mixed with 1.0 wt% of ADR4468 (rPET/ADR4468-1.0 wt%) exhibited the highest tensile and compressive strengths. The optimal content of ADR4468 improved the processability of filament extrusion and 3D printing, enhancing the mechanical properties of 3D-printed materials. The rTPU showed high chemical and thermal stability, and high elasticity. The tensile properties and processability of 3D printing products were further improved using the rTPU filaments dried at 25℃ and 25% relative humidity for 48 h. The flexibilities of rPET/ADR4468 textiles were improved by low infill density and intersection angle. The anisotropy of flexibility was observed in low-intersection-angle textiles, significantly improving the flexibility in the weft direction. The improved flexibility of the rTPU textiles was achieved with low infill density, a rotation angle of 45º, and fewer layers improved flexibility.

This study discusses the potential approach to recycling polyester textiles and TPU films into filaments for 3D printing textiles. The method is expected to enhance the value of the polyester textiles and TPU films recycled from PCTW. It would stimulate the recycling industry to identify the thermoplastics and sort them for further recycling. Due to the stimulation, thermoplastic PCTW storage would decrease rapidly via mechanical recycling instead of chemical degenerating and landfilling. Thus, the approach would provide sustainable filaments, expand the

applications, increase the recycling rate of polyester textiles and TPU films from PCTW and reduce the environmental loading for the disposal.

List of Publications

Submitted refereed journal paper

1. Hu L.; Sun J.; Zhang M.; Liu J.; Jiang S., A Filament Production Approach to Recycling Polyester Textile for 3D Printing, *Advanced Materials Technologies*, submitted.

Refereed conference presentations

1. Hu L.; Sun L., A Circular Economy Review: Conceptualizing Upcycling Post-consumer Textile Waste for 3D Printing Material, *2nd Textile & Fashion Innovation Congress*, **2022**.
2. Hu L.; Jiang S., Recycling Approach of Thermoplastic Polyurethane Films for 3D Printing Textiles, *Association of Universities for Textiles*, **2023**.
3. Hu L.; Jiang S., A Circular Economy Approach of Recycled Polyester Textiles for 3D Printing Flexible Textiles, *6th International Conference on 3D Printing & Bioprinting, AI, Digital and Additive Manufacturing*, **2023**.

Patents

1. 姜绶祥; 胡凌泉, 一种回收聚酯类纺织品生产熔融沉积 3D 打印线材的方法, 中国专利 202310363177.7.
2. 姜绶祥; 胡凌泉, 一种回收热塑性聚氨酯膜生产熔融沉积 3D 打印线材的方法, 中国专利 202310659757.0.

Acknowledgements

First, I am deeply grateful to my chief supervisor, Prof. Shouxiang Kinor Jiang, for his unwavering support and belief in me. His insightful comments and suggestions encouraged me in the most challenging time of my academic research. His advice motivated and inspired me out of rock bottom to turn the tables step by step: starting from writing patents to protect developed methods, attending international conferences to find more solutions, and publishing papers to record research achievements. At that moment, his patient guidance was to me as a lighthouse is to a lost ship. Although the research work was so demanding and stressful, my confidence has been restored to face the incoming challenges in the future.

I am greatly indebted to my co-supervisor, Prof. Jun Liu, for his suggestion and support in the research. His rigor inspired me to pay attention to every detail in my experiments, which helped me to discover and record extraordinary phenomena to reveal mechanisms. Luckily, I got a great start on my academic research.

I want to express my sincere gratitude to Dr. Lushan Sun and Prof. Jianzhong Sun for their invaluable contributions to the conceptualization, methodology design, data collection, and discussion of the current work. Their coordination efforts in the cooperation between The Hong Kong Polytechnic University and Jiangsu University are highly appreciated.

I want to especially thank Meng Zhang for his assistance in filament extrusion and 3D printing. His skilled operation improved the quality of samples and made the

experiments more effective and efficient.

My special thanks go to my wife, parents, and parents-in-law for their love, understanding, and encouragement throughout the completion of the study. Their supports make my career achievement a reality.

Finally, my gratitude extends to The Hong Kong Polytechnic University for the funding opportunity to undertake my studies and Jiangsu University for the experiment support during the special time of Covid-19.

Table of content

List of Figures

List of Tables

List of Abbreviations

3D	three-dimensional
ABS	acrylonitrile butadiene styrene
BHET	(2- hydroxyethyl) terephthalate
DEG	diethylene glycol
DMT	dimethyl terephthalate
DLS	digital light synthesis
EG	ethylene glycol
FDM	fused deposition modeling
FTIR	Fourier transform infrared spectroscopy
G’	storage modulus
G’’	loss modulus
HDI	hexamethylene diisocyanate
HDPE	high-density polyethylene
LDPE	low-density polyethylene
MDA	methylene diphenyl amine
MDI	methylene diphenyl diisocyanate
NH_3	ammonia
P&G	Procter & Gamble
PA	polyamide
PA6	polyamide 6

PCTW	post-consumer textile waste
PEG	polyethylene glycol
PET	polyethylene terephthalate
PETG	polyethylene terephthalate glycol
PG	propylene glycol
PLA	polylactic acid
PP	polypropylene
PS	polystyrene
PTMG	poly tetrahydrofuran
PU	polyurethane
PVA	polyvinyl alcohol
rHDPE	recycled high-density polyethylene
rLDPE	recycled low-density polyethylene
rPET	recycled polyethylene terephthalate
rPET/ADR4468	recycled polyethylene terephthalate composited with ADR4468 additive
rPS	recycled polystyrene
rTPU	recycled thermoplastic polyurethane
SEM	scanning electron microscope
SLA	stereolithography
SLS	selective laser sintering
TPA	terephthalic acid

TDA	toluenediamine
TDI	toluene diisocyanate
T_{cc}	clod crystallization temperature
T_g	glass transition temperature
T_m	melt temperature
TPU	thermoplastic polyurethane
TSC	textile sorting center
UV	ultraviolet
XRD	X-ray diffractometer
ω	dynamic frequency sweeps

Chapter 1. Introduction

This chapter introduces the background of the study, which introduces thermoplastic waste recycling for 3D printing, PCTW recycling, and 3D-printed textiles. The background mainly focuses on introducing the development of waste recycling for 3D printing and the current challenge for thermoplastic recycling from PCTW into 3D-printable filament for 3D-printed textiles. The rationale is to provide the motivation for the study and to explain how thermoplastics are recycled from PCTW into 3D-printable materials and used for 3D printing textiles.

1.1 Research background

3D printing has fabricated many creative and functional products according to customers' demand for personalized goods in recent years. 3D printing is additive manufacturing that directly generates products from 3D models with less waste and uses sustainable materials during processing[1]. The 3D models are digitally designed according to customization, satisfying different target customers. With the popularization of 3D printing, 3D-printed products have gradually appeared in people's daily life.

Thermoplastic recycling for 3D printing has been used for recycling different thermoplastics from other material sources, such as recycled polyethylene terephthalate (rPET) from water bottles, recycled low-density polyethylene (rLDPE) from meal-ready-to-eat pouches, and recycled polystyrene (rPS) from petri dishes.

Since these recyclable thermoplastics are designed for hollow blow modeling or calendaring, their viscosities are higher than extrusion-grade materials. The heating and shearing during the reprocessing break the polymer chains of thermoplastics, which reduces the viscosity of recycled thermoplastics and makes them suitable for the extrusion of 3D-printable filaments. Thus, these thermoplastics which are fabricated by hollow blow modeling and calendaring are suitable for recycling from other resources into 3D printing.

Currently, it is urgent to recycle the thermoplastics from post-consumer textile waste (PCTW), which prevents PCTW from landfilling and incinerating to reduce the environmental loading. As reported, 10% of the textile waste has been recycled with only 8% of it has been reused across Europe. This recycling rate for PCTW in the U.S. has been reported at 15-16%. The low recycling rate with the continuous accumulation of textile directly booms an environmental loading of textile waste disposal. The rest of PCTW has been disposed of by landfilling (57%) and incinerating (25%). It is important to increase the recovery rate of textile waste by high-value-added approaches.

Since 3D printing can provide enough commercial interest for 3D-printable materials, recycling PCTW into 3D-printable materials is a potential approach to increase the recovery rate and reduce the environmental loading. With the developments of material recycling processes, a new source referred to as post-consumer textile waste (PCTW) can be used to produce filaments for 3D printing textiles. However, several challenges impede thermoplastic recycling from PCTW for

3D printing. The flowability of the polyester recycled from PCTW is too high to be extruded into 3D-printable filaments, which must be adjusted by additives. The mechanical method is rarely investigated for recycling thermoplastic polyurethane (TPU) films into 3D-printable filaments. Moreover, the development of 3D-printable filaments is restricted by limited applications, which should be expanded to encourage polyester textile and TPU film recycling. To address these challenges, this thesis investigates the material properties of polyester and TPU recycled from polyester textiles and TPU films. It also discusses the potential applications of polyester and rTPU filaments for 3D printing textiles.

1.2 Research objectives

The study aims to recycle thermoplastic textiles into 3D-printed products. Some challenges should be overtaken according to the recycling processes including thermoplastic textile identification, 3D-printable filament extrusion, and 3D printing.

(1) To enhance the rheologic properties of polyester-textile-recycled 3D printing materials recycled from polyester textiles, thereby improving the processability of extruding filaments and 3D printing for enhancing the mechanical properties of 3D-printed recycled polyester materials.

(2) To improve the tensile property of TPU-film-recycled 3D-printable materials, thus improving the processability of filament extrusion and 3D printing.

(3) To explore the textile structure effects on 3D-printed textiles by using the filaments made from recycled polyester textiles, thus improving the flexibility of the

printed textiles for further various applications.

(4) To determine the textile structure effects on 3D-printed textiles by using filaments made from recycled TPU films to improve the flexibility of the printed textiles for further various applications.

1.3 Significance and value

This study discusses the potential approach to recycling polyester textiles and TPU films into filaments for 3D printing textiles. The method is expected to enhance the value of the polyester textiles and TPU films recycled from PCTW. It would stimulate the recycling industry to identify the thermoplastics and sort them for further recycling. Due to the development of the recycling industry, thermoplastic PCTW storage would decrease rapidly via mechanical recycling instead of chemical degenerating and landfilling. Thus, the approach would provide sustainable filaments, expand the applications, increase the recycling rate of polyester textiles and TPU films from PCTW and reduce the environmental loading for the disposal.

Chapter 2. Literature Review

This chapter presents the background of the study, which introduces 3D printing technology used in PCTW recycling. The background mainly focuses on introducing the development of 3D-printed waste recycling and the current challenge for thermoplastic recycling from PCTW. The rationale is to provide the motivation for the study and to explain how the thermoplastics from PCTW are recycled into 3D-printable materials and used in 3D printing.

2.1 Thermoplastic waste recycling for FDM 3D printing

3D printing is additive manufacturing that fabricates physical products by adding material layer by layer using digital 3D models[2]. The application of FDM 3D printing is gradually transiting from laboratory to factory, and it tends to be popular in households[3]. FDM 3D printing has gained popularity among users owing to its less waste generation, safety, user-friendly slicer software, and affordable cost (Fig. 2.1). Additionally, it uses sustainable material[1]. Commercial filaments have been developed to fit various polymers, such as acrylonitrile butadiene styrene (ABS)[4], polyvinyl alcohol (PVA)[5], thermoplastic polyurethane (TPU)[6], polylactic acid (PLA)[7], polypropylene (PP), and polyethylene terephthalate (PET). These 3D-printable materials can be recycled after 3D printing, and the recycled materials can be extruded into 3D-printable filaments for 3D printing[8]. The recycling source is from the 3D-printed waste and other thermoplastic waste.

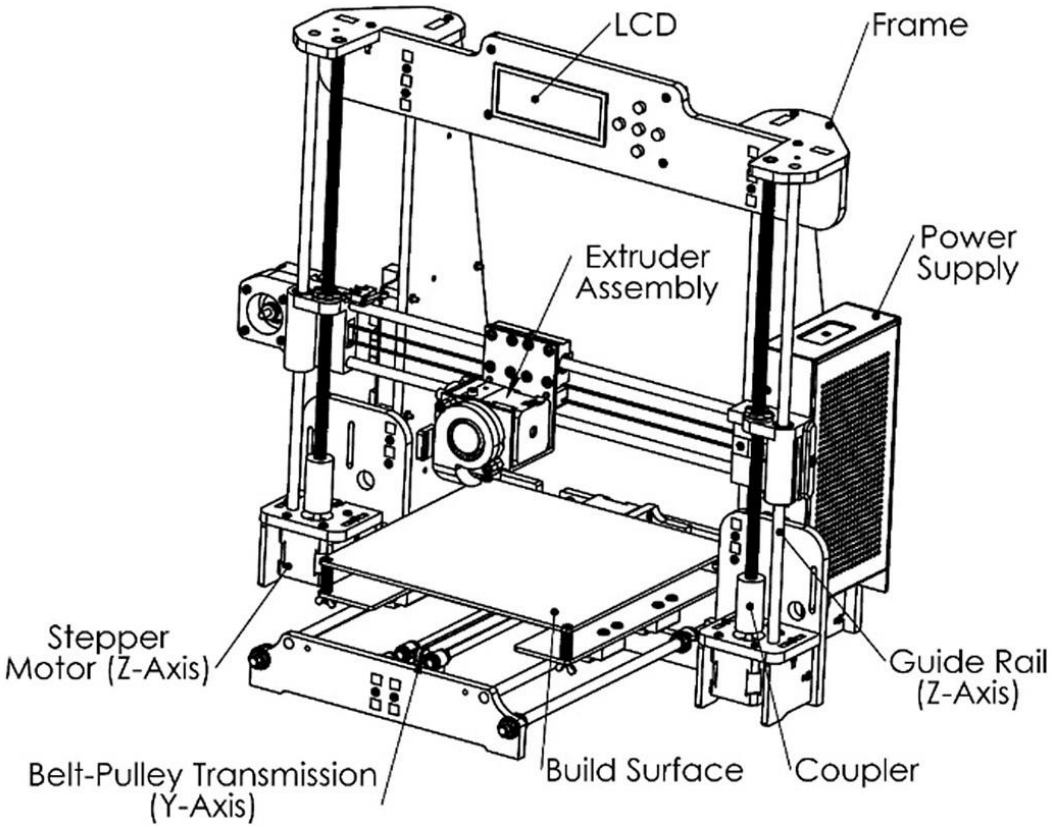

Figure 2.1. FDM 3D printer[1].

2.1.1 Thermoplastic waste recycling

With the 3D-printed products accumulating, the proper disposal of 3D-printed waste should be considered to prevent the pollution of 3D-printed thermoplastics. Studies have shown that 3D-printed PLA and ABS wastes can be recycled after granulating[9]. The granules have been directly printed using a particle-based FDM 3D printer[10]. Moreover, the 3D-printed waste granules can be melted and extruded into recycled filaments for filament-based FDM 3D printing[11]. Meanwhile, some 3D printers and recycling machines are open resources[12]. They can be 3D-printed and assembled by householders. The filament-based FDM printing can further reduce the cost of 3D printing and recycling for householders to create and recycle their

customized products.

Several materials are reportedly recycled from other resources, such as recycled PET (rPET) from water bottles[13], recycled low-density polyethylene (rLDPE) from meal-ready-to-eat pouches[14], and recycled polystyrene (rPS) from petri dishes[15]. The viscosities of the above materials are higher than extrusion-grade materials owing to their hollow blow modeling or calendaring processes. Since the polymer chains are broken during processing and reprocessing, the viscosity of recycled materials reduces. Thus, they are potentially reprocessed through extrusion for 3D-printable filaments. The natural fiber waste from PCTW is reportedly recycled using 3D printing technology. The silk, wool, and cellulose wastes have been powdered, blended, and extruded with PLA into the filaments[16]. The fiber-reinforced PLA filaments have been printed into different products. However, the thermoplastics from PCTW are rarely recycled in the 3D printing industry. Since the PCTW thermoplastics are spinning-grade polymers, their viscosities are much higher than the extrusion-grade polymers. At the end of the shaping process of the melted thermoplastic flux, it will flow like water and cannot be stretched into a fine filament. Thus, many thermoplastics from PCTW cannot directly be recycled and extruded into filaments as 3D printing materials due to their high flowability.

2.1.2 3D printing products using recycled thermoplastics

Currently, several companies have developed 3D-printable filaments with recycled thermoplastics. To prevent environmental pollution, Formfutura has

reformed filaments made from the post-industrial extrusion waste streams of PLA filaments. Moreover, GreenGate3D has introduced its new PET-G filaments that are fully recycled from PET-G waste. In addition, Nefilatek produces recycled Nefila TPU filaments using industrial waste. The gradually increasing brands attracted their attention to recycled filaments with industrial waste, meaning the market for recycled 3D-printable filaments is growing.

Maldonado-García et al. have recycled the high-density polyethylene (HDPE) and polypropylene (PP) from the ocean waste[17]. The recycled HDPE (rHDPE) and recycled PP(rPP) have been blended and extruded into rHDPE/rPP composite filaments through 3D printing. Based on the designed 3D models, the elliptical gears (Fig. 2.2a) and the spectacle frame (Fig. 2.2b) are successfully printed, which indicates that ocean plastic waste can be recycled via 3D printing technology for complex-shaped and customized products with reasonable properties.

Figure 2.2. 3D-printed products using rHDPE/rPP-based blends and composites: (a) elliptical gear with the shaft; (b) spectacle frame[17].

Audi has started the “Mission: Zero” program producing 3D-printed assembly aids for its vehicle production[18]. The assembly aids are printed using recycled materials from packaging waste. Employees collect sorted plastics, including the

sensor packaging (Fig. 2.3), and shred the plastics into granulates for 3D-printable filament extrusion. Then, the filaments are fed into a 3D printer producing the designed individual assembly aids. As assembly aids, 3D-printed pushers help workers to attach clips to the car body and some tools to improve the precision of attaching the four-ring logo part to the vehicle rear. This phenomenon suggests that 3D printing can simultaneously recycle packaging waste and enhance production efficiency in vehicle assembly.

Figure 2.3. Audi 3D-printed products for assembly aid using recycle packaging materials[18].

The Tokyo 2020 Olympic victory ceremony podium produced from recycled plastics using 3D printing (Fig. 2.4). Tokolo designed the podium based on the

sustainability concept of Tokyo 2020[19]. The plastic items were collected by the community members in the host country Japan according to Tokyo 2020 Podium Project[20]. The collections comprised shampoo and dish detergent bottles. Procter & Gamble recycled the collections with other plastic waste recovered from the ocean to fabricate the podium, which inspires consumers directly to contribute to recycling plastic waste to create the Olympic medal podium. Meanwhile, the fabrication of the podium using recycled the collections demonstrates that 3D printing technology has great potential in plastic waste recycling.

Figure 2.4. 3D-printed Tokyo 2020 Olympic victory ceremony podium using the recycled plastic[19].

2.2 Post-consumer textile waste recycling

Recently, the global consumption of textile products has steadily increased[21] due to the population boom[22]. Novel textiles with higher performance and more favorable designs than existing products are currently being fabricated. The fabrication of novel

textiles stimulates excessive consumption of the products by rapidly replacing existing textile products[23]. Consumer attractive goods are produced through the fabrication of novel textiles, attempting to replace the existing products owing to the designed durability of novel textile products[24]. The consumption of novel textiles will render existing textiles waste. Additionally, some parts of products are subjected to harsh conditions during their serving period, which damages the specific part of products, thus shortening the life span of the textile at specific parts[25]. This damage caused by harsh conditions will rapidly reduce the function of the products, even almost the other fresh parts. Furthermore, the shortened lifetime of the textile products accelerates the replacement of the textile products, directly increasing PCTW waiting for disposal[26]. The rapid replacement of the existing products aggravates the environmental load from both textile production and disposal[27]. Because the textile consists of synthetic and natural fibers, the continuous use of the textile can decrease petroleum reserves and negatively impact the environment.

Synthetic fibers are produced as novel textiles with special functions and high durability, covering the insufficiency of natural fibers from petrochemicals. Due to the properties of synthetic fibers, they are mainly used to produce sport-related textile products. Moreover, industrial textiles are fabricated using functional synthetic fibers. Due to the cost reduction of natural fibers, polyester fibers are gradually replacing natural fibers. In addition, polyester fibers are currently used to blend with natural fibers for functionalization. As reported, the production of 1 kg of PET required 62 kg of water and 125 MJ of energy with the emission of 2.8 kg CO_2 [28], which is an eco-

friendly and win-win development for the textile industry. However, synthetic fibers are nonbiodegradable, causing environmental problems during waste disposal processing. In addition, they are nonrenewable. These disadvantages will be directly exposed when the accumulation of synthetic fibers reaches that of natural fibers. As a projection, the textile industry used 98 million tons of nonrenewable resources in 2015, which would increase to 300 million tons in 2050[29]. Therefore, thermoplastic recycling from PCTW is greatly important for the sustainable development of the textile industry.

Studies have shown that 10% of the clothing waste has been recycled using 8% of the reused clothes across Europe[30]. The recovery rate of textiles in the U.S. has been reported to be 15-16%[31]. The low recovery rate with the increasing quantity of textiles directly increases the environmental loading of PCTW disposal. The rest of PCTW are being disposed of through landfill (57%) and incineration (25%)[30]. During the landfilling, the toxic emissions from the chemical residues degraded from dyes and polymers of PCTW pollute the solid[32]. The residues absorbed by crops can threaten our health if contaminated crops are consumed. Additionally, some nonbiodegradable dyes and polymers can significantly reduce the disposal capacity of landfills due to their high durability[33]. Meanwhile, the increase in PCTW with long disposal time would require a large proportion of landfills, thus wasting valuable and limited land resources. Incineration is an effective method to generate energy from waste. However, it emits green gas, toxic gas, and particulates, which causes air pollution, thereby potentially posing health risks[34]. Therefore, increasing the recovery

rate of textiles is urgent for reducing environmental impact. Novel applications are necessary to recover the textile market, thus reducing the environmental impact of PCTW disposal.

Currently, the PCTW is mainly collected by non-profit organizations in Europe[35]. Annually, tons of PCTW are donated into the drop-in bins (Fig. 2.5). The PCTW is gathered at the textile sorting center through the network of transport and bins for further processing[35]. The PCTW collections comprise shoes, bags, soft toys, and textile-related accessories.

Figure. 2.5. The drop-in bins collecting clothes[36].

The PCTW collections are sorted before reprocessing. According to their sorting manuals, the trained sorters separate the different categories of textiles for specific applications. The collected textiles are roughly classified into several categories, including “reusable”, “recyclable”, and “unrecyclable” (Fig. 2.6). The high-quality PCTW is sorted professionally and sold in textile secondhand markets[37]. Then, the non-reusable PCTW should is separated from recyclable textiles and unrecyclable waste. The recyclable textiles are further sorted into subcategories, including nonfabric, fabric, yarn, fiber, and “plastic.” After sorting, the packaged PCTW is sent to the factory as the raw materials for further reprocessing and fabricating new products.

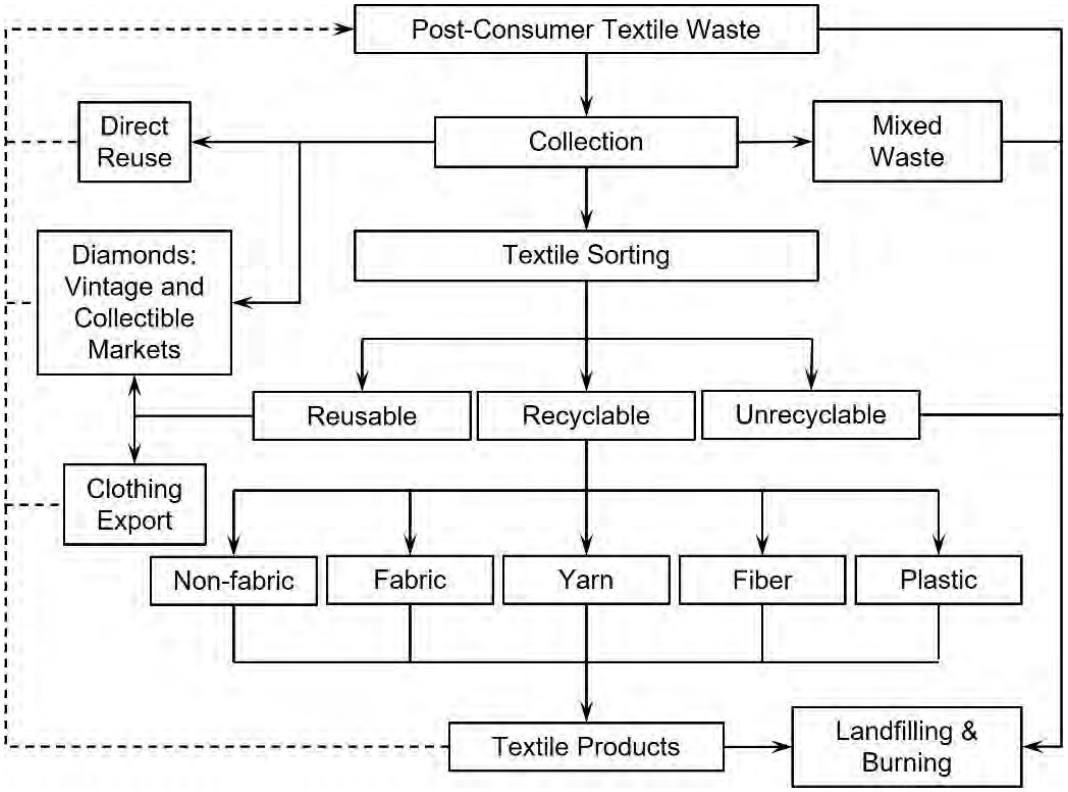

Figure 2.6. Conventional recycling system[37].

2.2.1 Thermoplastic recycling from PCTW

The recyclable PCTW is usually ignored due to its application limitation and low interest, especially the recyclable thermoplastics. As reported, the number of recyclable textile subcategories is currently fewer than reusable textile[35]. The recyclable textiles include white and colored cotton, knitted, and other recyclable textiles. Cotton recycling has gained more attention owing to its industrial recyclability development process. However, polymer textiles are roughly classified into other recyclable textiles, making it challenging for the recycling industry to effectively and efficiently distinguish and sort recyclable polymers. These sorts of polymers increase environmental loadings more than natural degradable textile waste. As a result, increasing the recycling rate of the polymers from PCTW is important, reducing the environmental loading. According to the market-driven system for recycled textiles, the applications of high-value-added products recycled from PCTW can effectively lead to the development of the textile industry.

2.2.3.2 Polyester textile recycling

PET is semi-crystalline polyester material used in many industries, such as fashion, drinks bottles, and packaging. PET is used to fabricate a high-performance textile such as a polyester textile owing to its excellent chemical resistance and mechanical properties. Because of the high volume of polyester textiles produced annually, the disposal problem of polyester textile waste has gradually increased. The nondegradable property of PET advances its durability during usage. However, the

nondegradibility of the PET makes the disposal of polyester PCTW challenging. Thus, exploring effective and efficient recycling methods for polyester PCTW disposal is urgent to reduce its environmental impact.

2.2.3.2.1 Structure of polyester

The structure of PET determines its application and recycling in the textile industry, including chemical and semi-crystalline structures.

Chemical structure: The high mechanical properties of PET can be attributed to the combination of terephthalate and ethylene glycol ester in the main chain. The PET polymer chain is rigid due to the inflexible benzene ring of terephthalate. The rigidity of the polymer chain is mainly controlled by ethylene glycol ester parts, which exhibit slight flexibility for PET, thereby preventing the main chain from breaking and improving the mechanical properties. To fabricate the PET fibers, the chain length of spinning-grade PET can be designed to be lower than the extrusion grade, increasing the flowability.

Semi-crystalline structure: The PET can be crystallized further to improve the mechanical properties and prevent crack propagation in the structure. The crystallization of PET increases the energy barrier during structural damage. PET tended to crystallize and orient during melt spinning, the cooling, and drawing processes, improving the mechanical performance of fibers.

The fashion industry selects PET material based on the PET structure to fabricate polyester textiles for wearable products. Therefore, the recycling process of polyester

textiles (from PCTW) is similar to that of PET textiles.

2.2.3.2.2 Conventional chemical recycling

Chemical recycling is a practical and conventional method of recycling PET materials[38]. The chemical recycling method can depolymerize the PET PCTW into monomers for recycling[39]. The degraded monomers are further separated, purified, and recycled into chemicals, such as terephthalic acid (TPA), ethylene glycol (EG), dimethyl terephthalate (DMT), and other monomers. According to different recycling mechanisms, the rPET chemical recycling process is categorized into alcoholysis, hydrolysis, ammonolysis, and glycolysis methods.

Alcoholysis is a trans-esterification-based reaction that uses alcohol to depolymerize the PET at high temperature and pressure to produce DMT and EG monomers[38].

Hydrolysis is an effective chemical recycling method that hydrolyzes the ester functional groups in PET at high pressure and temperature. In neutral hydrolysis of PET, high-purity TPA and EG monomers are produced[40].

Ammonolysis is a method designed to digest PET with ammonia (NH_3) to reduce the reaction temperature and produces terephthaldiamide (TPA di-amide) as an intermediary product and EG. Then, the TPA di-amide is further converted into TPA, p-xylylene di-amine, or 1, 4-bis(amino-methyl) cyclohexane[38].

Glycolysis is a glycolysis-based depolymerization chemical recycling method that uses excess glycol, including EG, diethylene glycol (DEG), and propylene glycol

(PG), to produce bis (2- hydroxyethyl) terephthalate (BHET), dimer, and oligomers[40]. It is widely used on a commercial scale to depolymerize PET. The generated molecules can be used for various industrial applications stimulating the rPET chemical recycling market.

2.2.3.2.3 Mechanical recycling

Mechanical recycling is another practical available method for recycling PET material[41]. The method is used to recycle the polyester PCTW maintaining the chemical and physical structures[42]. The polyester textile with its fiber structure can be directly reused by mixing recycled polyester textiles or fibers with the concrete, thus reinforcing the concrete[43] and improving the mechanical properties of concrete (Fig. 2.7).

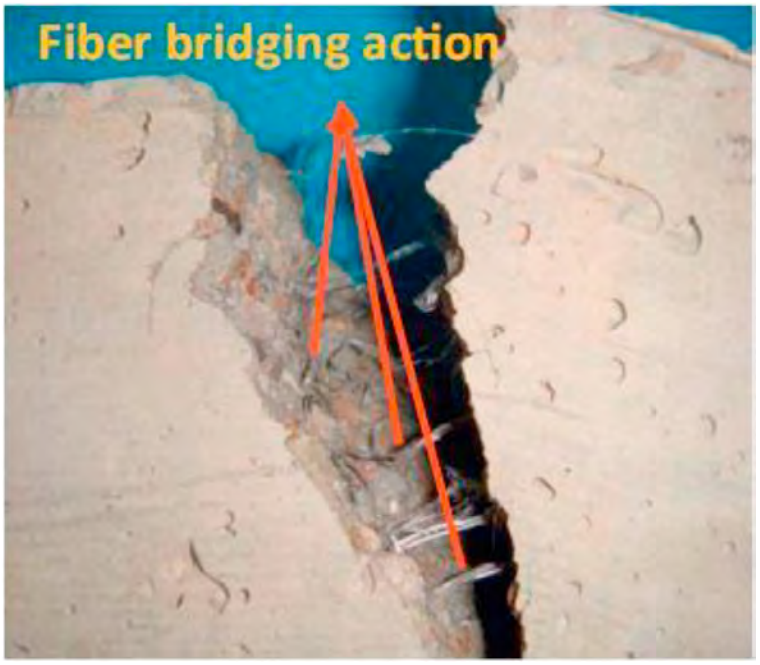

Figure 2.7. Fiber bridging action improving the mechanical properties of concrete[43].

Another method is to destroy the fiber structure of polyester PCTW and retain the polymer chains (chemical structure). Though the mechanical method is rarely applied in polyester textile recycling, the success of PET bottle recycling indicates the potential application in polyester PCTW recycling. The recycled PET (rPET) is melted and extruded into granules for further reprocessing[44]. After the granules are washed and dried, the additives can be added and mixed to improve the performance or adjust the flowability of rPET for specific applications. Then, the polyester PCTW is fed into the extruder, melted (at high temperature and pressure), extruded, and shaped into the filaments using cooling water for the first time. After the cooling of the filament, the filaments are directly granulated. The granules are mixed with virginal PET granules for second-time extrusion. The blended granules are melted, extruded, and granulated into rPET granules to produce new products. As reported[45], the rPET granules can be spun into new fibers used in the textile industry.

The rPET has been applied as the substrate in the composite materials[46]. In recent years, rPET-based composites have been reinforced using different fibers, such as glass[47], carbon (Fig. 2.8)[48], and natural fibers[49]. The fibers enhance the mechanical properties of rPET composites. In addition, rPET materials can be reinforced using particles, including $CaCO_3$[50], fly ash[51], and graphene[52]. rPET can be blended with other polymer materials as additives to improve the mechanical performance of rPET[46] to meet the mechanical requirements, thereby broadening the rPET composite application. Moreover, rPET has been functionalized with modified ZnO particles to absorb ultraviolet (UV) and infrared[53]. The functionalization of rPET can expand its

application in different fields to further stimulate rPET usage with high value.

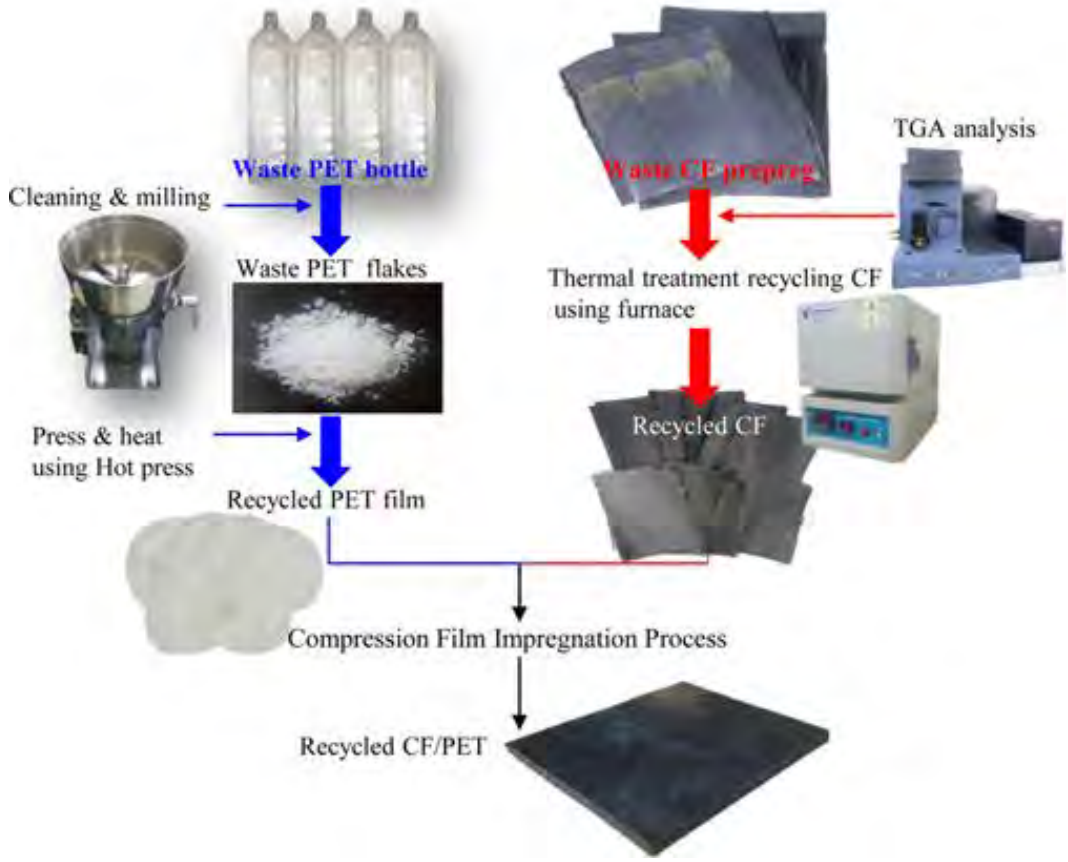

Figure 2.8. PET recycling using carbon fibers[48].

2.2.3.3 TPU film recycling

Thermoplastic polyurethane (TPU) is the elastic material used in various industries, such as textile, automotive, and medical[54-57]. The textile industry is the largest end-user of TPU, including footwear, waterproof costumes, and hats. This increasing market increases the demand for the disposal of TPU post-consumer textile waste (TPU PCTW). With the increasing yield and usage of TPU, TPU PCTW storage increases. TPU PCTW needs to be disposed of due to its nondegradable property. Therefore, exploring effective and efficient recycling methods of TPU PCTW is crucial to reduce the environmental loading and energy waste of TPU disposal.

2.2.3.3.1 Structure of TPU

The structure of TPU PCTW determines the reprocessing methods. The elasticity of TPU can be attributed to the block-copolymer structure, which consists of the isocyanate hard segment with polyether or polyalcohol-based soft segments. The hard segments can commercially use hexamethylene diisocyanate (HDI)[58], toluene diisocyanate (TDI)[59, 60], and methylene diphenyl diisocyanate (MDI)[61] to improve the mechanical properties of TPU. The soft segments can commercially use polyethylene glycol (PEG)[62], butanediol-based polyester, and poly tetrahydrofuran (PTMG)[61] to improve the elasticity. Due to the principle of polymer self-assembly and the compatibility difference of block-copolymer segments, the hard segment chains rearranged themselves to form the crystalline regions[63]. The crystalline regions prevent crack propagation in the structure, thereby increasing the energy barrier during structure damage and improving the mechanical performance of TPU. However, the soft segments form amorphous regions. Because the polymer chains of soft segments can spontaneously be assembled into random coils in amorphous regions, they can be easily deformed under the force field, thus improving the elasticity of TPU. The block-copolymer structure endows TPU with outstanding mechanical performance and high elasticity, widely used in sports engineering. In addition, the large area of amorphous regions in TPU allows visible light to pass through with fewer influences, which contributes to the transparency of TPU. TPU is used as a transparent soft textile in the fashion industry owing to its transparency.

2.2.3.3.2 Conventional chemical recycling

Chemical recycling is a conventional method of recycling TPU materials. This method depolymerizes the TPU polymer chains into monomers. TPU is a type of non-cross-linking PU material; as a result, TPU has chemical structures similar to PU materials and uses similar chemical recycling methods as PU. During chemical recycling, the TPU polymer chains are degraded into monomers. The degradation products are separated, purified, and recycled into chemicals, such as toluenediamine (TDA), polyol, methylene diphenylamine (MDA), and other monomers. TPU chemical recycling has been divided into hydrolysis, aminolysis, and glycolysis methods according to different recycling mechanisms[64].

According to the reaction of the urethane with water steam, the hydrolysis recycling breaks the urethane functional groups that connect hard and soft segments at a high temperature and pressure and converts PU to a two-phase liquid system. The upper layer consists of an aqueous solution of TDA, while the lower layer is formed by recovered polyol[65].

Aminolysis is a reaction in which the amine groups of the urethane replace the ester groups. The MDI-based PU is decomposed into polyester polyol, MDA, and alkanolamine derivatives, such as 2-hydroxyethyl carbamic acid ester[66].

Glycolysis is the most widely used chemical recycling process for PU, which interchanges the ester group with the hydroxyl group of glycols, such as DEG and EG. The MDI and polyether polyol-based TPU can be decomposed and converted into

a liquid for recycling polyester polyol[67].

2.2.3.3.3 Mechanical recycling

Mechanical recycling is the practical method for recycling TPU material. This retained the chemical structure and even the physical structure of TPU PCTW. The TPU PCTW can be shredded into flakes and granules used to fill pillows or toys owing to its elasticity[64].

Another method of mechanical recycling is the reshaping of TPU PCTW without altering the chemical structure of TPU polymer chains. The TPU PCTW is melted, extruded, and granulated into granules for further reprocessing[68]. The additives can be added and mixed with granules to improve the performance of recycled TPU (rTPU) for specific applications. Then, the TPU PCTW is fed into the extruder and melted at high temperature and pressure (Fig. 2.9). The melted rTPU is extruded into a cooling water bath and shaped into rTPU filaments. The rTPU filaments are directly granulated. The rTPU granules can be mixed with virginal TPU granules. The mixture is melted and further blended to uniform the quality of rTPU. The blended rTPU is extruded and granulated for further reprocessing. As reported[68], the rTPU has been melted and blow-spuned into nonwoven textiles. In addition, TPU PCTW can be recycled with polyamide 6 (PA6) waste to hybrid fibers to reduce the cost of separating different materials from PCTW[69]. Moreover, TPU PCTW has been used as raw materials for polyurethane (PU) foams using polyol components[70].

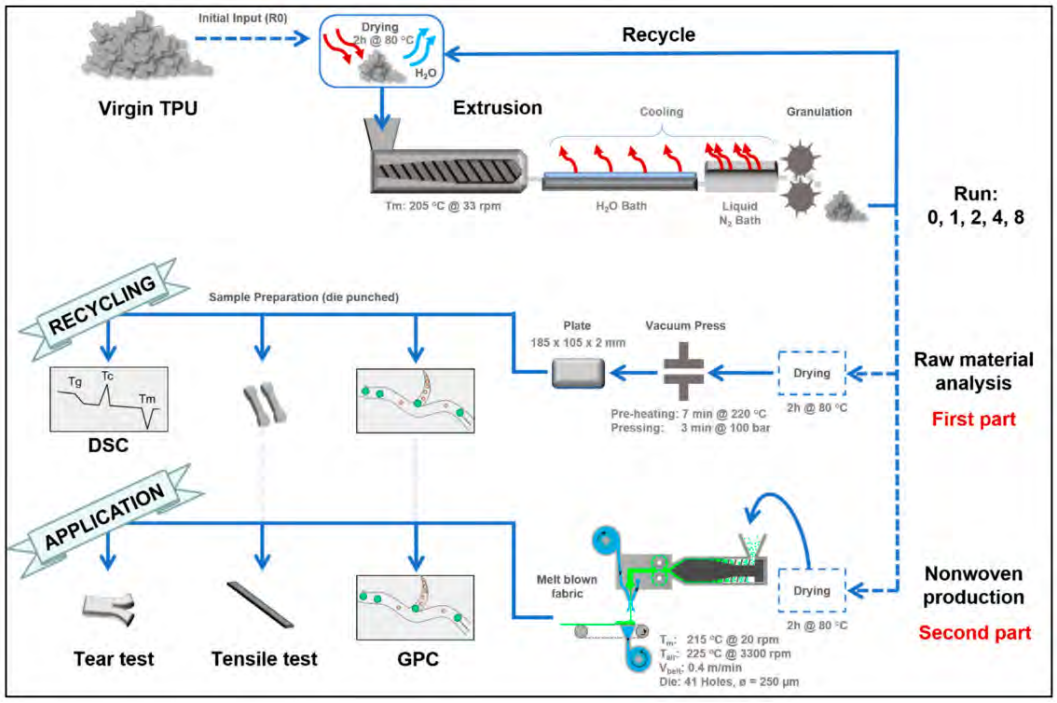

Figure 2.9. TPU recycled into nonwoven products[68].

2.2.2 Products using recycled thermoplastic from PCTW

H&M launched Autumn 2021 recycled denim collections[71]. The collection was fabricated using 100% recycled textiles, threads, labels, pocketing, metal zippers, and trims (Fig. 2.10). This closed loop is based on the H&M in-store recycling system[72]. It shreds the cotton-made, polyester-made, and cotton/polyester blended textiles into recyclable cotton and polyester fibers. Another way is to decompose the cotton into powders and then separate the fine polyester fibers from the blended textiles[73]. After separating, filtering, carding, and drawing the powders, the recycled polyester fibers are spun into a single yarn thread. The equipment twists the threads to increase the strength. The polyester yarns are knitted or woven into new textiles for the collection. H&M provides solutions to the close loop of the fashion industry using polyester fibers recycled from textile waste into new textiles for denim collections.

Figure 2.10. H&M recycled denim collection[71] and shredding equipment of H&M Looop in-store recycling system[72].

Nike has explored the Space Hippie footwear collection (Fig. 2.11) and transformed scrap materials into new products[74]. The upper contains 90 wt% of recycled materials, and the sole blends standard Nike foams with 15 % of Nike Grind Rubber, reducing the usage of virgin materials with unique colorful patterns. The Nike Grind Rubber is a chopped rubber and thermoplastic elastomer material with various granulate sizes. It is recycled from end-of-life shoes. These rubber granules are mixed with different colors to form random color 3D patterns and endow the unique aesthetics for the functional forms. Nike recycles rubber and thermoplastic elastomer materials and adds a high aesthetic value to them, motivating customers to recycle aesthetic products.

Figure 2.11. Nike Space Hippie constructed with recycled materials[74].

2.3 3D-printed textiles using FDM 3D printing

2.3.1 Conventional textile structures

Many 3D-printed textiles use conventional textile structures, including weaving and knitting.

The woven textiles have been printed using FDM 3D printing (Fig. 2.12)[75]. Warp pillars are fused layer by layer, and weft threads are extruded through an S-shaped path to weave the pillar. As the printed layers increase, the woven textiles are grown in the warp direction. The weft threads can print various woven textile structures and generate different patterns in the woven textiles by changing the shapes of the pillars and the paths of the weft threads. This method uses the nozzle to directly stimulate shuttle weaving to extrude threads in the weft directions. The threads exhibit high flexibility in the weft direction due to the weave structures. Moreover, the strengths of textiles are different in the two directions because the warp pillars are printed layer by

layer with low tensile strength, and the weft threads are continuously extruded at high tensile strength. The structural design forms an anisotropy of mechanical properties in the two directions.

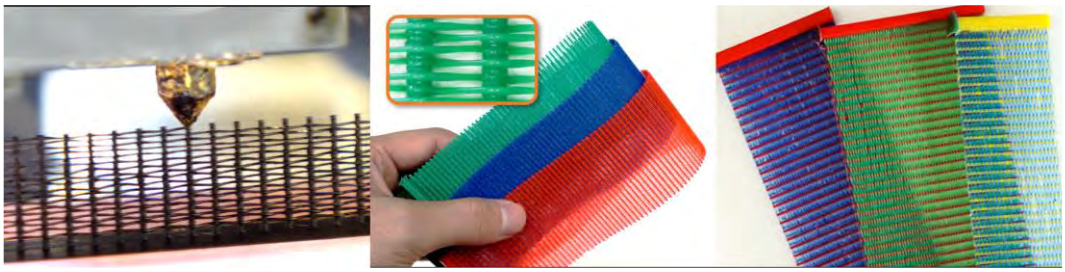

Figure 2.12. 3D-printed woven textiles[75].

The knitted textiles are developed using FDM 3D printing, as shown in Fig. 2.13[76]. The textile is printed with a soft PLA material without support structures. Stitches are printed layer by layer in the normal direction of the plane of the knitted textile. The stitches of the textile are almost separated, with less undesirable connections formed by the movement of nozzles. Due to the fine-printed stitches of the textile, the flexibility of the textile is similar to SLS 3D-printed textiles. However, the printing accuracy restricts the diameters of the stitches to print thinner stitches at a high density of the knit structure using FDM 3D printing.

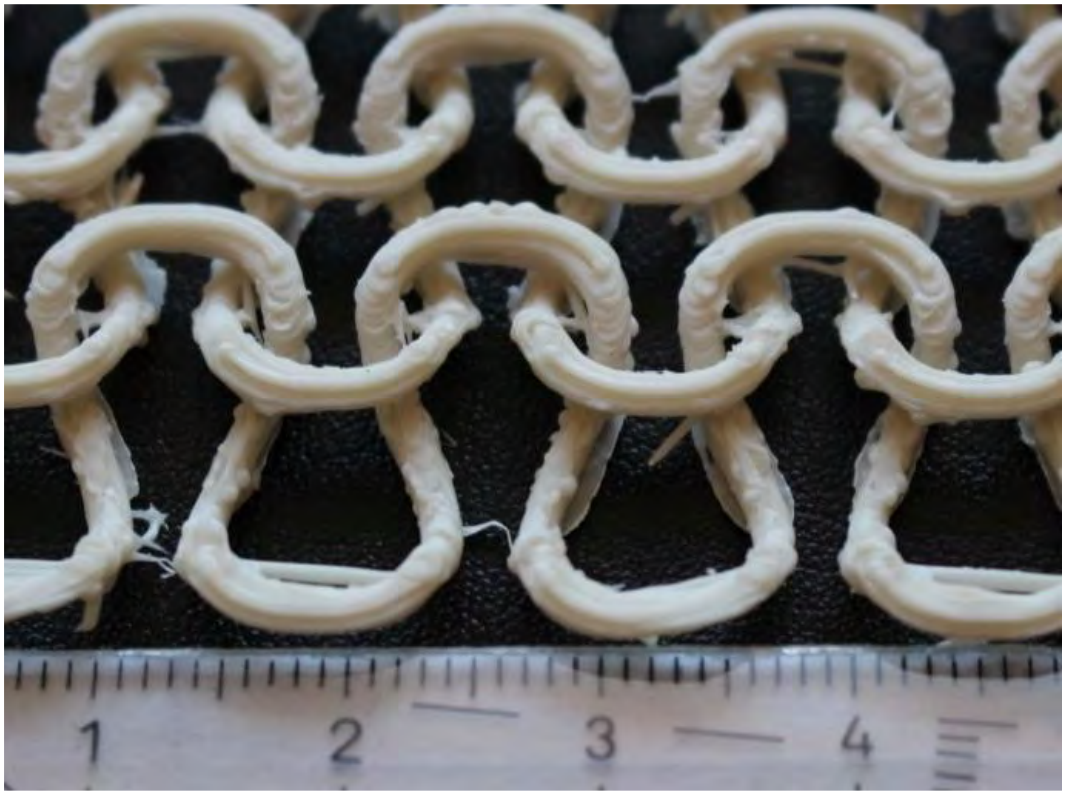

Figure 2.13. 3D-printed knitted textiles[76].

2.3.2 3D-printed textile for fashion design

In recent years, digital fabrication used 3D printing technology in the hands-on producing wearable products, such as textiles and dresses.

The bodice portion provides a new idea to combine conventional designs with 3D-printed textiles (Fig. 2.14)[77]. The 3D-printed textiles were integrated as insets in the bra front of the bodice portion. Similarly, the bra back inserted the 3D-printed textiles. The textiles deformed with their gray and pink color shifting, achieving an ombre effect. This phenomenon inspired the sense of stereoscopy and movement during the exercise. The functional and aesthetic combination plays a significant role in the symmetrical design incorporating knitted and 3D-printed textiles. In addition, it compensated for the limitation of maximum printing dimension. This bodice portion

suggests the great potential in 3D-printed textile development.

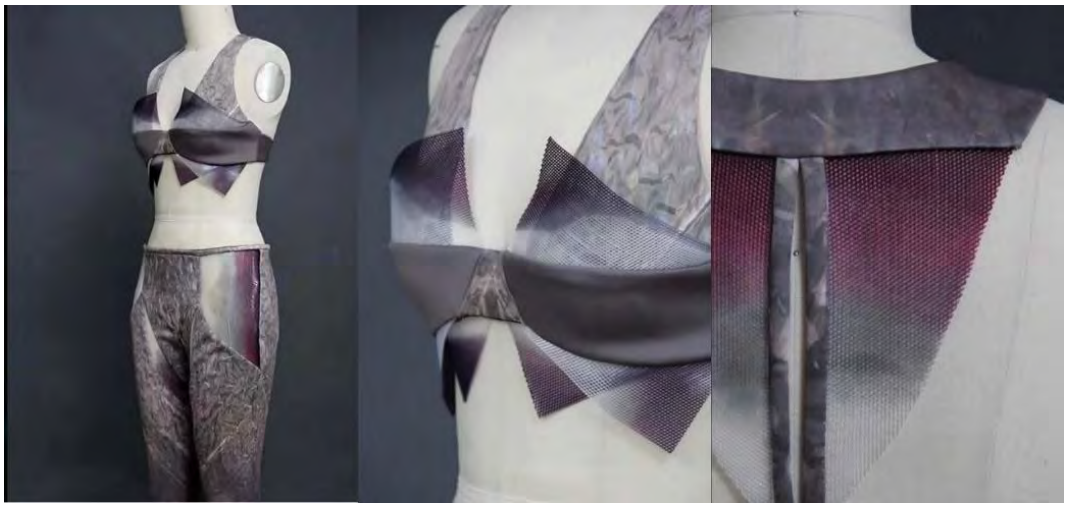

Figure 2.14. 3D-printed textile designed for bodice portion[77].

Danit Peleg in Shankar College Israel printed her entire final collection using home FDM 3D printers[78] (Fig. 2.15). The FilaFlex filament, an elastic TPU filament, was used to print the flexible black and white dress[79]. To further increase the flexibility of the dress, Danit Peleg designed the stretchable pattern with a structural aesthetic. This representative work presents the prospective FDM application in fashion design and will encourage people to print their designed garments at home via FDM 3D printing technology.

Figure 2.15. Danit Peleg's 3D-printed dress[79].

2.4 Research gaps

The extensive literature review shows the development of polyester and TPU recycling processes from PCTW and 3D-printed textiles. The problems limiting the developments are as follows:

(1) The flowability of polyesters from textiles is relatively high and unstable to be directly extruded into fine filaments. The lack of techniques in the rheological adjustment for polyester textiles restricts the development of the mechanical recycling method of polyester textiles from PCTW.

(2) Although recycled TPU materials exhibit high chemical and thermal stabilities in the mechanical recycling method, the lack of high-value applications limits the development of the mechanical recycling process of TPU film from PCTW

(3) Conventional textiles contain many voids, making printing difficult using FDM 3D printing without support structures.

(4) The complicated 3D modeling and 3D printing path design restrict the development of 3D-printed textiles.

To solve these problems, this study developed approaches for recycling polyester textiles and TPU films into 3D-printable filaments used for 3D printing textiles and investigated the structural effect on 3D-printed textiles.

2.5 Summary

Thermoplastic waste has been recycled for FDM 3D printing in recent years. Maldonado-García suggests the possibility of recycling waste into customized products. Audi applies the technique to improve industrial assembly. The Tokyo 2020 podium was produced by recycling thermoplastic using 3D printing technology. These cases demonstrate that thermoplastic waste can be recycled for FDM 3D printing in different areas, including customized products, industrial assembly aids, and the victory podium. Meanwhile, the recycled materials are not only from 3D-printed waste but also from other sources. Thermoplastics from textile waste might be a new source of recycled materials for FDM 3D printing.

The recycling process of thermoplastics from PCTW remains a challenge for the fashion industry. Many companies take responsibility for recycling them. H&M has established a recycling system for recycling cotton, polyester, and combined blended textiles into new clothes. Fine polyester fibers can be recycled effectively and efficiently from shredded mixtures.

However, the thermoplastics from PCTW are conventionally decomposed into

monomers using the chemical recycling method. Less thermoplastic PCTW has been recycled using the mechanical recycling method. This method saves energy and chemicals. Nike has attempted to use a novel collection of elastic thermoplastics from the footwear industry in the shoe upper and sole to form 3D colorful patterns, which explores the mechanical recycling method for thermoplastics from PCTW.

Because FDM 3D printing can provide enough commercial interest for 3D-printable materials, recycling PCTW into 3D-printable filament is a potential approach to increase the recovery rate and reduce the environmental impact associated with PCTW. The recycling of PCTW into 3D-printable filament can reduce the storage of thermoplastics from PCTW, thus reducing the cost of the mechanical recycling method.

The conventional woven and knitted textiles are printed using FDM 3D printing technology, which attempts to simulate the weaving and kitting structures to enhance the flexibility of 3D-printed textiles. To further add value to recycled thermoplastics from PCTW and complete a circular approach, novel textiles with various flexible structures should be developed.

Chapter 3. Methodology

This chapter describes the experimental outline and methods for this study. It provides the preparation of FDM 3D-printable filaments using polyester textiles and TPU films and 3D-printed textiles using polyester and rTPU filaments. The methods were used to optimize the mechanical properties of recycled polyester and TPU material, improve the processibility of the rPET/ADR4468 and rTPU filament extrusion, and enhance the flexibility of 3D-printed rPET/ADR4468 and rTPU textiles.

3.1 Experimental outline

Fig. 3.1 shows an approach for recycling polyester textile waste and TPU film waste into 3D-printable filaments for 3D-printed textiles. This research aimed to apply the approaches, optimize recycling processes to improve the mechanical properties of 3D-printed materials, explore potential applications in 3D-printed textiles, and enhance the flexibility of 3D-printed textiles. The possibility of recycling polyester textiles and TPU films was investigated in this study. The polyester textiles and TPU film waste were initially transformed into powders and fragments to ease their transfer into the filament extruder. The extruder melted and shaped polyester powders and TPU fragments into rPET/ADR4468 and rTPU filaments. To enhance the mechanical properties of 3D-printed rPET/ADR4468 and rTPU materials, the polyester was mixed with different contents of ADR4468 additives, and the rTPU

filament was dried before 3D printing. After the enhancement of the material, the filaments were printed into rPET/ADR4468 and rTPU textiles with various structures. The different structures affected the mechanical properties and changed the flexibility of 3D-printed textiles.

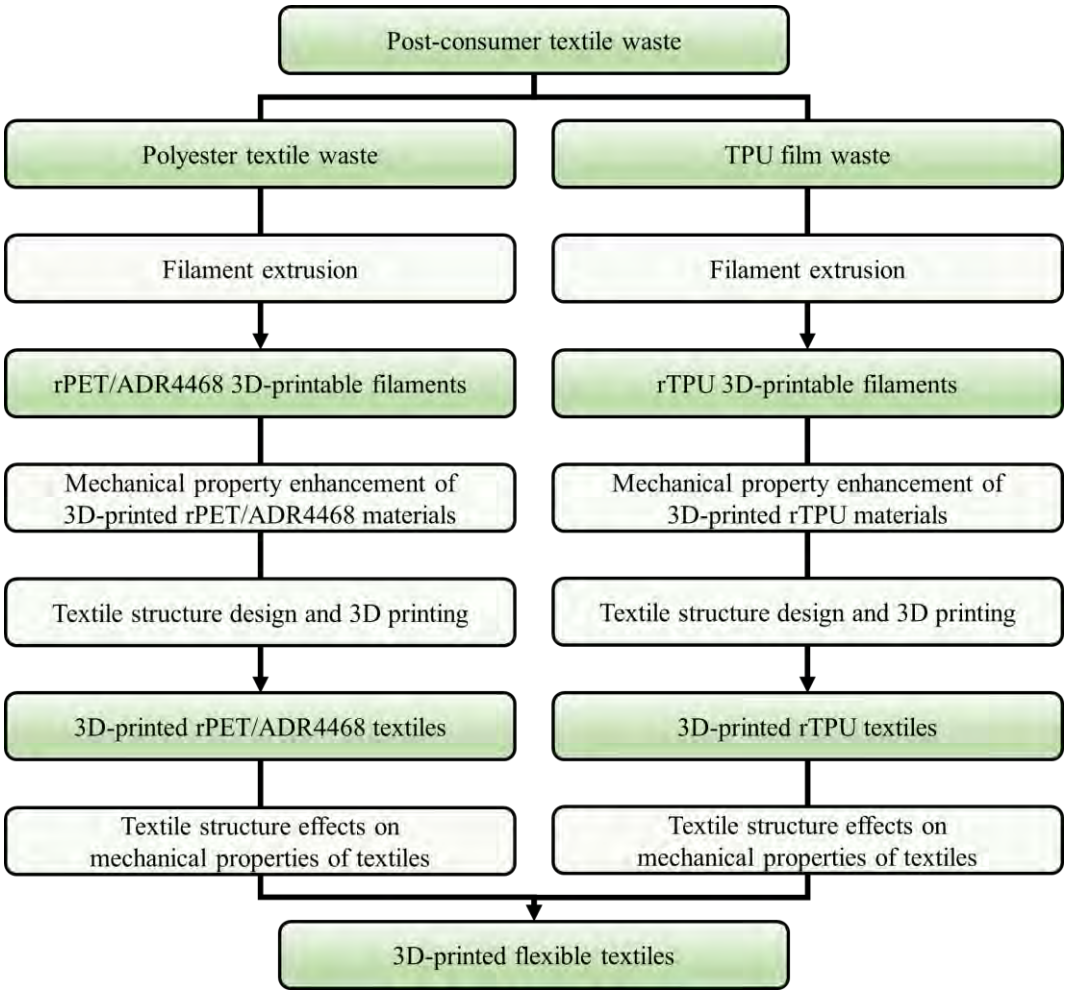

Figure 3.1. Scheme of experimental process.

3.2 Experimental materials

The polyester textile was purchased from Zhaoxin Xinbojin Textile Co. and used as polyester textile waste. Joncryl ADR 4468 was purchased from BASF. The TPU film was purchased from Dongguan Chang An Chun Pin Insulating Materials

Business Department and used as TPU film waste.

3.3 Polyester textile and TPU film recycling processes

3.3.1 Polyester textile recycling processes

Heat-pressure process using additives is different from the conventional mechanical recycling of polyester textiles. The details of these methods are illustrated in the subsequent chapter of rPET/ADR4468 filament production.

The polyester textiles were heat-pressed into thin boards. The heat-pressure process melted the polyester and removed air bubbles from textile voids, preventing the bubbles from breaking the melt in the extrusion process to improve the mechanical properties of filaments for high-quality 3D printing. Since the study focused on enhancing material properties of the 3D-printed polyester with additives, the heat-pressure process effects were optimized for polyester textile recycling.

To successfully extrude the polyester, the ADR4468 additive was mixed with polyester powders. The polyester from textiles was designed for fiber spinning using spinning-grade PET materials with higher flowability rather than extrusion-grade PET when the materials were melted. The high flowability reduced the recycled polyesters at the end of the filament extrusion, which could not be drawn and shaped into fine filament. The ADR4468 increased the viscosity of polyesters[80]. This improvement prevented the melt from dropping and forming fine filaments. Thus, ADR4468 was selected as an additive for polyester textile recycling.

3.3.2 TPU film recycling processes

The shattering method of TPU film into fragments is different from the conventional mechanical recycling process. The shattered fragments were extruded directly into fine filaments, which are illustrated in detail in the subsequent chapter of rTPU filament production.

The TPU film was shattered into fragments and fed into the filament extrusion. Due to the high elasticity of TPU film, the large size of the film could not be cut by the extruder screw and blocked the inlet to stop feeding TPU for the filament extrusion. To prevent blocking the inlet, the TPU film was shattered into small fragments.

The shattered TPU fragments were directly extruded into fine filaments. The viscosity of TPU melt was adjusted by the temperatures and screw speed of the extruder. Because this study focused on the enhancement of tensile properties of the 3D-printed rTPU, the rheological effects were controlled to the optimal extrusion conditions for TPU film recycling.

3.4 3D-printed textiles

3D-printed textiles were modeled from a thin board, and patterns of the thin board were program-generated using slicers, which are illustrated in detail in the subsequent chapters of 3D-printed rPET/ADR4468 and rTPU textiles. The infill density, rotation angle, and intersection angle were changed to investigate the structural effects on the flexibility of 3D-printed rPET/ADR4468 textiles. The infill

density, rotation angle, and layer number were changed to investigate the structural effects on the flexibility of 3D-printed rTPU textiles. The structural changes were different in rPET/ADR4468 and rTPU due to the load limitation and precision of the KES-F system. Moreover, the default textile was set at an infill density of 50%, rotation angle of 45º, intersection angle of 90º, and 2 layers to amplify the difference in the mechanical properties of textiles.

3.5 Summary

This study designed the approach of recycling polyester textile waste and TPU film waste into 3D-printable filaments for 3D-printed textiles. This research aimed to apply the approach, optimize recycling processes to improve the mechanical properties of 3D-printed materials, explore potential applications in 3D-printed textiles, and enhance the flexibility of 3D-printed textiles.

The heat-pressure condition and additive selection were controlled in the polyester textile recycling process to focus on the processability of filament extrusion and improve the mechanical properties of 3D-printed materials. In TPU film recycling, the shattering process was used to prevent blocking in the inlet of the extruder, and the viscosity was adjusted and controlled to the extrusion conditions to focus on enhancing the tensile property.

Due to the limitation of the KES-F system, the textile structural changes were different in 3D-printed rPET/ADR4468 and rTPU textiles, and the default textile was set at an infill density of 50%, a rotation angle of 45º, an intersection angle of 90º, and

2 layers to amplify the difference of the mechanical properties of textiles.

Chapter 4. A Filament Production Approach to Recycling Polyester Textile for 3D Printing

This chapter discusses the characterization results of 3D-printed rPET/ADR4468 samples. The rPET/ADR4468 materials were recycled from polyester textiles and advanced by ADR4468 additive. To evaluate their mechanical performance and demonstrate the advancement of the additive, the mechanical properties, thermal performance, morphology, crystal structure, and bonding configurations were analyzed.

4.1 Introduction

Recycling polyester textiles has become a critical item of discussion for many stakeholders in the environmental protection field[81]. Polyester textile waste has reached its storage limit because polyester cannot be easily recycled yet it is the most popular fiber used in fabrics. Textile waste is mostly landfilled (57%) or incinerated (25%)[30]. Unfortunately, landfilling and incinerating increase environmental loads, and are unsustainable methods of disposing polyester textiles. Thus, developing a high value-added approach to recycling polyester textile waste is timely and important.

3D printing might be the most viable method to realize a high value-added recycling approach. Since 3D printing has captured commercial interest for printable materials, it is potentially a good option to recycle polyester textile waste. However, several challenges are found in recycling polyester textile waste into 3D-printable

materials. Their low viscosity is designed for high-speed spinning, which during 3D printing, causes the polyester to buckle when passed through the extruder and filaments cannot be formed. In order to overcome this challenge, Singh et al.[46] used a chain extender to increase the viscosity of polymers to an appropriate value. The functional groups of the chain extenders bond the polymer chains to limit their mobility, thus increasing the melt flowability during reprocessing. Accordingly, chain extenders might be the solution for recycling polyester textile waste into 3D printing filaments.

In this work, polyester textile waste is recycled into 3D-printable materials by using a polymeric chain extender called ADR 4468 to modify the melt flow. To investigate the optimal usage of this additive, polyester textile waste is mixed with different amounts of ADR 4468 and extruded into filaments. Then, the filaments are 3D-printed into samples for mechanical performance tests. Meanwhile, the mechanism of how ADR 4468 contributes to realizing the recyclability of polyester textile waste is examined through various characterization methods, including differential scanning calorimeter (DSC), X-ray diffraction (XRD), Fourier-transform infrared spectroscopy (FTIR) analyses, rheological tests, and scanning electron microscope (SEM) observations.

4.2 Method

4.2.1 Polyester textile recycling

Fig. 4.1 shows the recycling approach which transforms polyester textile waste

into 3D printing filaments. Before the reprocessing commenced, the textile waste was washed and dried at 60℃ overnight, which removed dust from the textile surface. Then, the clean textiles were pressed, melted, and hot-pressed into a paper-thin plastic board with heat-pressure equipment at a temperature of 270℃ under a load of 10 MPa for 1 min. After air-cooling the plastic board down to 25℃, it was mixed with 1.0 wt%, 1.5 wt%, and 2.0 wt% of ADR 4468 (hereinafter rPET/ADR 4468-1.0 wt%, rPET/ADR 4468-1.5 wt%, and rPET/ADR 4468-2.0 wt%, respectively). The mixture was ground into powder by using a high-speed grinder at 8000 rad/min for 1 min. To transform the powder into 3D printing filaments, the powder was fed into a WSJ-12 filament extruder (Xinsuo, Shanghai, China). The extruder further mixed and melted the powder into a thermoplastic fluid. The thermoplastic fluid was then pushed out of the extruder, pulled through the die, and into the water tank and cooled in deionized water (50℃). The largest diameter of the filaments is 1.91 mm and the smallest diameter is 1.32 mm at the cross-section, which corresponds to 3D-printable filament diameters that range from 1.25 mm to 2.00 mm. Table 4.1 lists the parameters for optimal filament extrusion of polyester-based thermoplastics. In Table 4.1, Zones I to IV are the die, metering, compression, and feeding zones, respectively, marked on the extruder in Fig. 4.1. After rolling, the filaments with 1.0 wt%, 1.5 wt%, and 2.0 wt% of ADR 4468 (i.e., rPET/ADR 4468-1.0 wt%, rPET/ADR 4468-1.5 wt%, and rPET/ADR 4468-2.0 wt%, respectively) were obtained for 3D printing.

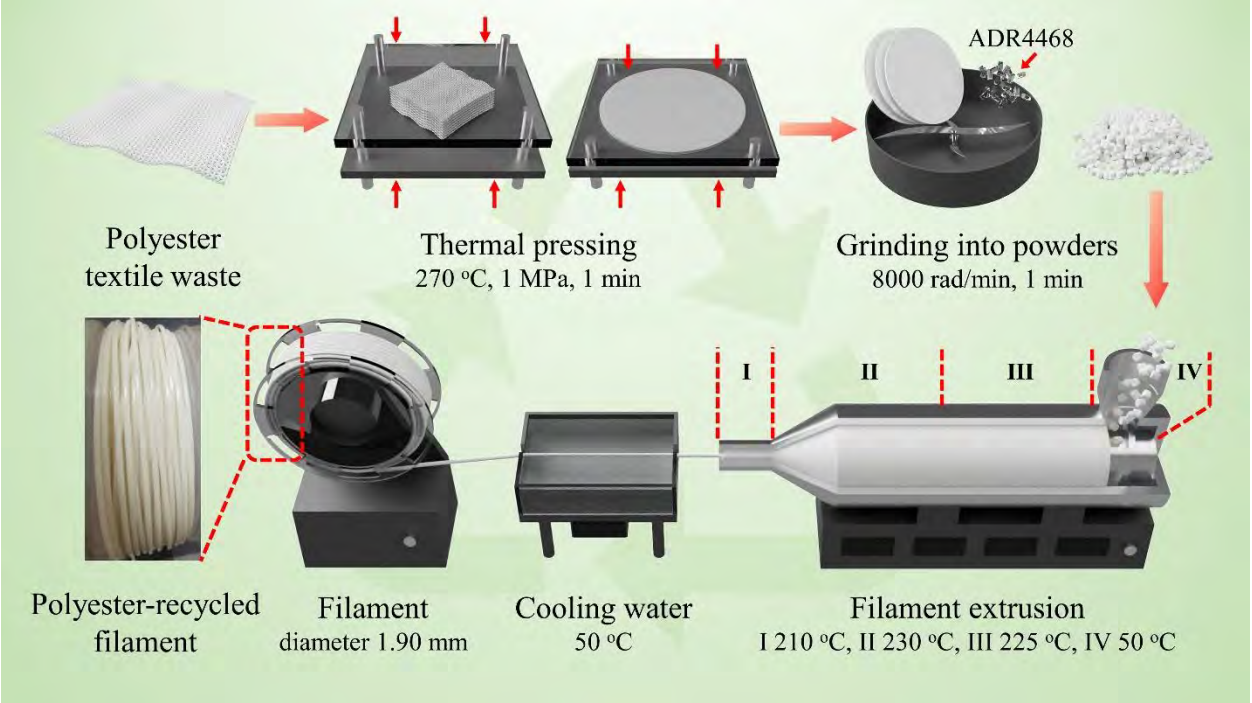

Figure 4.1. Fabrication of rPET/ADR 4468 filaments.

Table 4.1. Major parameters of rPET/ADR 4468 filament extrusion

Extrusion parameter	Value
Zone I temperature	210°C
Zone II temperature	230°C
Zone III temperature	225°C
Zone IV temperature	50°C
Cooling water temperature	50°C
Screw speed	60 rad/min

Notes: Zones I, II, III and IV denote die, metering, compression, and feeding zones.

4.2.2 3D printing using polyester filaments

To determine the material properties, the filaments were 3D-modeled and 3D-

printed into standard samples as illustrated in Fig. 4.2. The 3D models were designed and built with Pro/Engineer, a 3D modeling software (Parametric Technology Corporation Creo, Massachusetts, USA) according to testing standards. The Pro/Engineer software exported the 3D models into STL files for the 3D printing slicer software - Cura (Ultimaker B.V., the Netherlands) which sliced the models into layers. However, the 3D-printed parts were not entirely dense with empty space, so an infill pattern was needed. Patterned lines were used to fill the parts that were the 3D printing or nozzle extrusion path. Moreover, the slicer software sets the 3D printing parameters based on the material characteristics of the filaments. These parameters directly determine the quality and outcome of the 3D printing, as shown in Table 4.2. After setting the parameters, the slicer software converted the modeled parameters into GCODE files. GCODE is a programming language that controls the filament-based FDM 3D printer (JGMaker-A6, JG AURORA, Shenzhen, China) to print the samples according to the sliced models. After printing, the samples were cooled down to 25℃ and removed from the print plate to reduce potential deformation of the samples. To explore the possibility of using 3D printing techniques for the fashion industry, a flexible mesh (Fig. 4.2) was printed as a novel prototype to determine the implications for the industry.

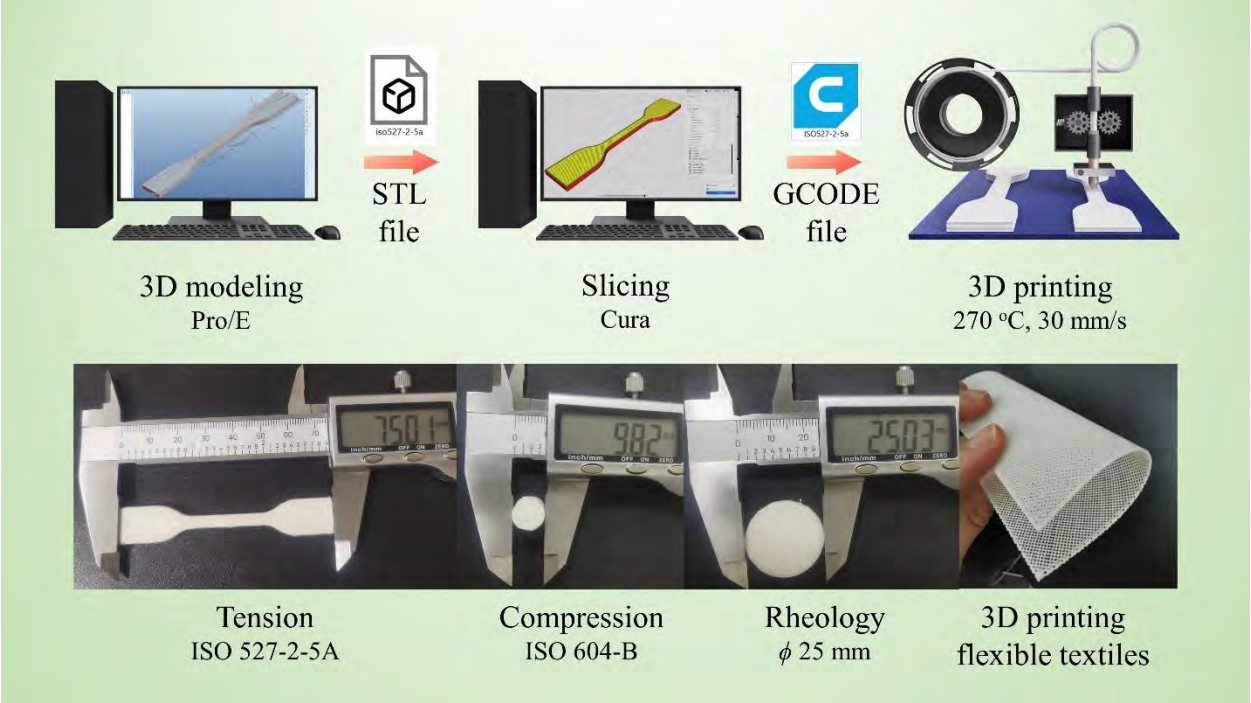

Figure 4.2. 3D printing and 3D-printed samples using rPET/ADR 4468 filament.

Table 4.2. 3D printing parameters for rPET/ADR4468 3D-printed samples

3D printing parameter	Value
Layer height	0.2 mm
Wall thickness	0.8 mm
Infill density	100%
Infill pattern	Lines
Printing temperature	270°C
Build plate temperature	70°C
Flow	110%
Printing speed	30 mm/s

4.2.3 Characterization

Several characterizations were done to investigate the effect of the weight ratio of ADR 4468 on the material properties, including the crystal and chemical structures, thermal performance, morphology, rheology, and mechanical performance.

The crystal structures of the 3D-printed samples were analyzed by using an XRD system (D8 ADVANCE, Bruker Co., Massachusetts, USA) with Cu Kα as the radiation source at λ=1.54056 Å over an angular range of 10º and 60º. The chemical structures of the polyester textiles and filaments, and 3D-printed samples were identified by using an FTIR spectrometer (ALPHA II, Bruker Co., Massachusetts, USA). The thermal performance of the polyester textiles and filaments, 3D-printed samples, and ADR 4468 were examined by using a DSC (DSC4000, PerkinElmer, Massachusetts, USA) at temperatures from 30℃ to 300℃ at a heating rate of 10℃/min under a nitrogen gas flow of 20 ml/min. The morphology of the cross sections of the 3D-printed samples was observed under an SEM (S3400, Hitachi High-Tech Co., Tokyo, Japan) at 20 kV for tensile stress. The rheological performance of the textile-compressed plates and 3D-printed plates was evaluated by using a rheometer (Haake MARS III, Thermo Fisher Scientific co., Waltham, USA) with a plate diameter of 25 mm from 10^{-1} to 10^{2} rad·s^{-1} with dynamic frequency sweeps (ω) at 270℃ under 1% strain. The mechanical performance of the 3D-printed samples was tested by examining the tension and compression (E43, MTS System Co., Minnesota, USA). The tensile tests were conducted in accordance with ISO 527 standard at a displacement rate of 10 mm/min. The compression tests were based on

ISO 604 standard at a rate of 2 mm/min.

4.3 Results and discussion

4.3.1 Crystal structure analysis

The crystal structures of the rPET/ADR 4468 samples were analyzed through XRD (Fig. 4.3). The three characteristic peaks of rPET/ADR 4468 at 2θ values of 17.5°, 22.8°, and 25.8° correspond to the (0 1 0), (1 -1 0), and (1 0 0) crystal planes of polyethylene terephthalate (PET)[82, 83]. The broad peaks and noisy XRD patterns are attributed to the semi-crystallization of the PET chains. When the PET chains rapidly cooled down, small crystalline regions formed during the 3D printing. The randomly distributed crystalline regions resulted in larger characteristic peaks and amplified the XRD noise level. Compared with rPET/ADR 4468-1.5 wt% and rPET/ADR 4468-2.0 wt%, rPET/ADR 4468-1.0 wt% has the highest peak intensity at 25.8° of the (1 0 0) crystal plane. The higher intensity indicates that this sample has more crystalline regions. Moreover, the peaks at the (0 1 0) and (1 -1 0) planes of rPET/ADR 4468-2.0 wt% are slightly larger towards a high 2θ angle. This phenomenon might be due to the internal compressive residual stress[84]. According to Bragg's law $2d\cdot\sin\theta = n\lambda$, the peaks that shift towards a high 2θ angle means that the spacing between the crystal planes of rPET/ADR 4468-2.0 wt% (d in Bragg's law) is reduced under X-ray irradiation at a constant λ. The smaller planes suggest that the crystal regions are compressed by the internal compressive residual stress. Therefore, internal compressive residual stress might be present in rPET/ADR 4468-2.0 wt%.

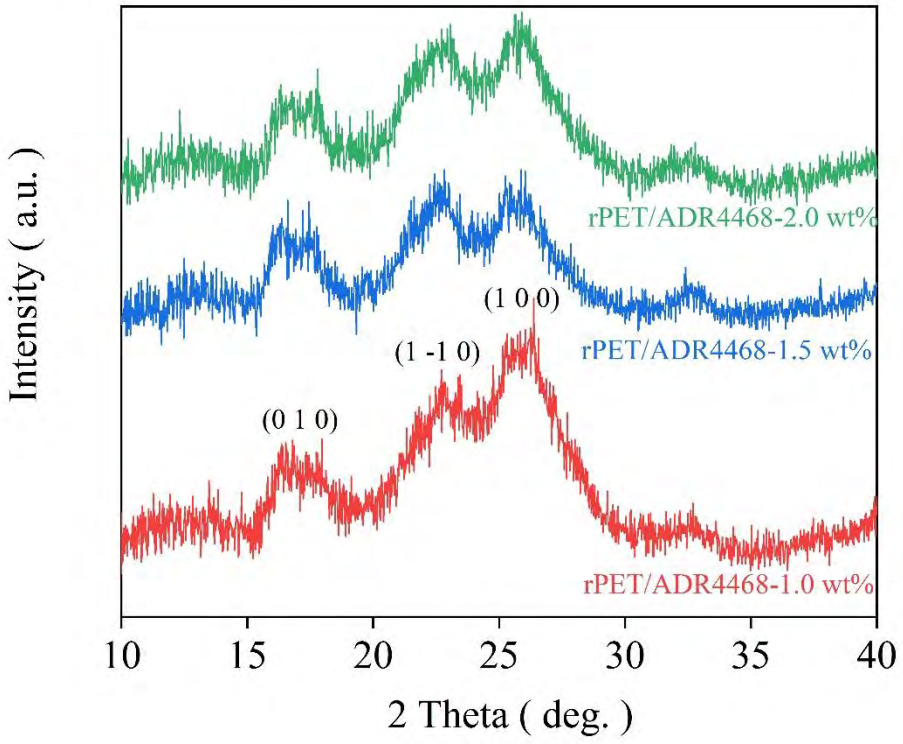

Figure 4.3. XRD of rPET/ADR 4468 (1.0 wt%, 1.5 wt%, and 2.0 wt%.

4.3.2 Chemical structure analysis

The chemical structures of the polyester textile, rPET/ADR 4468 samples (1.0 wt%, 1.5 wt%, and 2.0 wt%), and ADR 4468 were identified by using FTIR spectroscopy (Fig. 4.4a). The polyester textile and rPET/ADR 4468 curves have PET characteristic peaks that reflect the hydroxyl end groups. Meanwhile, the ADR 4468 curve shows the characteristic peaks of the epoxy groups.

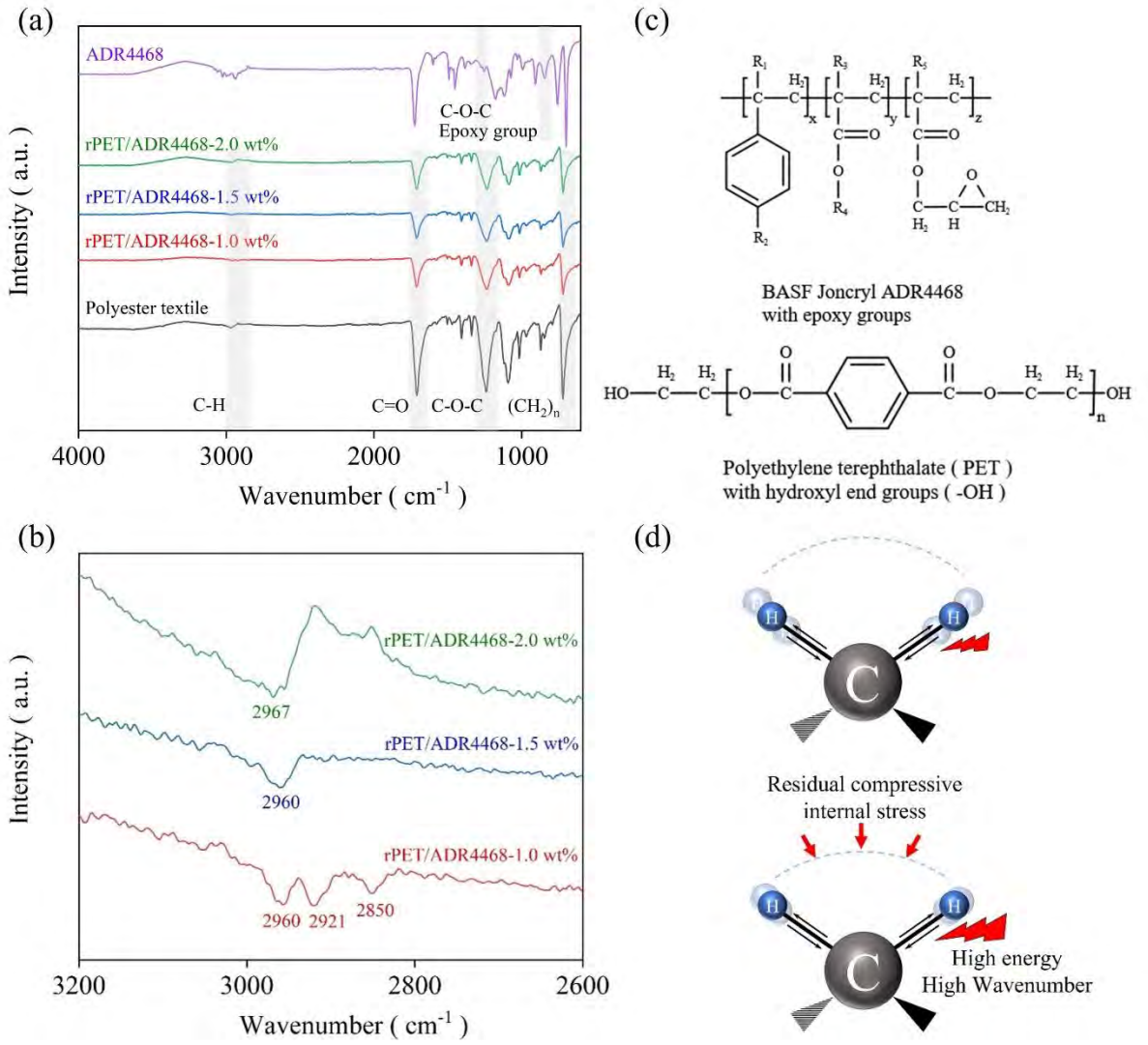

Figure 4.4. (a, c) FTIR of chemical structures of polyester textile, rPET/ADR 4468, and ADR 4468, and (b, d) internal compressive residual stress that shifts C-H stretching vibration of rPET/ADR 4468 samples.

The polyester textile and rPET/ADR 4468 samples have similar polymeric chains, which contain terephthalic acid repeat units with ethylene glycols (to form the terephthalates) and hydroxyl end groups (Fig. 4.4c). There are several characteristic peaks of the terephthalates. A single peak of the C=O stretching vibration is found at

1712 cm^{-1}, which is smaller than that of the aliphatic and olefinic esters (near 1744-1739 cm^{-1})[85]. Simultaneously, a split peak of C-O-C appears at 1238 cm^{-1}, which is larger than that of the ethers (near 1225-1060 cm^{-1}). These peaks indicate that one side of C=O is connected to the C-O-C forming ester groups and the other side is attached to the C atoms of the benzene ring (benzoate esters near 1735-1720 cm^{-1}). Moreover, the attached benzoates are 1,4-disubstituted, owing to their C-H wagging vibration of the ring hydrogens near 860-800 cm^{-1}. Since none of the weak peaks of ring deformation vibration was observed, the two 1,4-substituents are both the C=O of the ester groups. These characteristic peaks show that the terephthalates produce the polyester textile and rPET/ADR 4468. As diol monomers, ethylene glycols form the ester groups with the terephthalic acids specifically forming the ester groups. A single high peak of the CH_2 rocking vibration is found at 722 cm^{-1}, due to the $(CH_2)_2$ (alkane) of ethylene glycol in the crystalline state, which suggests the presence of PET crystalline regions based on the XRD analysis. Simultaneously, hydroxyl groups of the ethylene glycols are the end groups of the PET chains. Characteristic peaks appear including the O-H stretching vibration (3600 cm^{-1}) and O-H deformation vibration of alcohol (1409 cm^{-1} and 1372 cm^{-1}). Since no characteristic peaks of carboxylic acid were observed, the hydroxyl groups are the main end groups of the PET chains.

The ADR 4468 polymer chains contain 1,4-disubstituted benzene rings, ester groups, epoxy groups, and long-chain alkyl groups (Fig. 4c). The R_1, R_2, R_3, R_4, and R_5 might be H, CH_3 or a long-chain alkyl group[86]. Since characteristic peaks of the

1,4-disubstituted benzene ring were observed, including C-C stretching vibration and C-H bending deformation, the R_2 could be the alkyl group. A single high peak of the C=O stretching vibration (1724 cm^{-1}) and a split peak of the C-O-C stretching vibration (1180 cm^{-1}) appear, which suggests that ester groups are present and their C=O is attached to the C atoms of the alkyl groups. The two characteristic peaks of the epoxy groups (1256 cm^{-1} and 843 cm^{-1}) point to the presence of epoxy groups in the side chains. Meanwhile, some of the epoxy groups are ring-opened and produce diols (3600 cm^{-1} and 1384 cm^{-1}). To improve the elasticity, ADR 4468 is added because this additive contains long-chain alkyl groups and the CH_2 rocking vibration of long-chain alkyl groups with a large sharp peak appears at a low wavenumber (699 cm^{-1}). This low wavenumber suggests that the polymer chain contains many long-chain alkyl groups in the branched chains. Based on the epoxy groups and long-chain alkyl branches, ADR 4468 could improve the extrusion flow of rPET/ADR446.

The internal compressive residual stress shifts the C-H stretching vibration peak to a high wavenumber as shown by the rPET/ADR 4468-2.0 wt% curve. Fig. 4.4b shows that the C-H stretching vibration peak integrates the split peaks (2960 cm^{-1}, 2921 cm^{-1}, and 2850 cm^{-1} in rPET/ADR 4468-1.0 wt%) into a single peak (2960 cm^{-1} in rPET/ADR 4468-1.5 wt%) and then shifts to high wavenumber (2967 cm^{-1} in rPET/ADR 4468-2.0 wt%). According to the Planck relation $E = hc\tilde{\nu}$, when the peak shifts to a higher wavenumber $\tilde{\nu}$, the C-H bonds absorb more energy E for their stretching vibration. The vibration is restricted by local groups and its space is reduced for high activation energy. This phenomenon might be attributed to the

internal compressive residual stress. The residual stress compresses and reduces free space in the crystalline and amorphous regions. With the amount of free space reducing, the residual stress further restricts the C-H stretching vibration for high activation energy and shifts the peak to a high wavenumber.

4.3.3 Thermal performance

To investigate how ADR 4468 affects the flow of the filament extrusion, the thermal performance of the rPET/ADR 4468 samples and ADR 4468 was examined by using DSC (Fig. 4.5a). The initial DSC heat curves show the effects of ADR 4468 on the recycling of the polyester material through the glass transition temperature (T_g), cold crystallization temperature (T_{cc}), melt temperature (T_m), and reaction temperature of the samples.

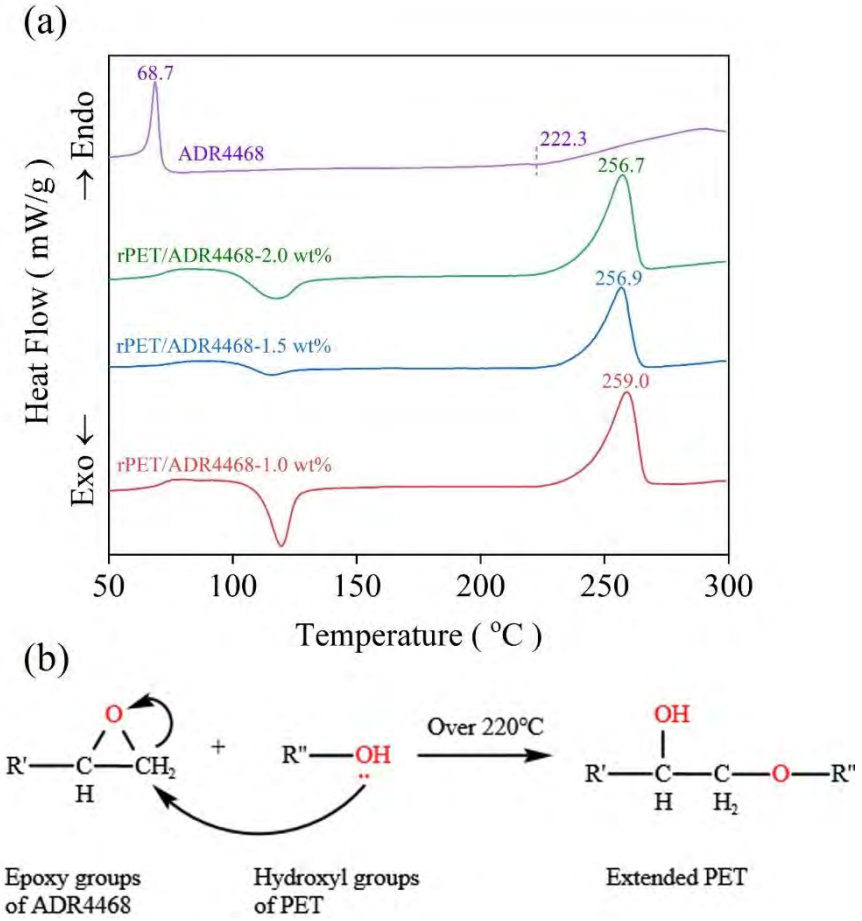

Figure 4.5. (a) Initial DSC heat curves of PET PCTW, rPET/ADR 4468 (1.0 wt%, 1.5 wt%, and 2.0 wt%), and ADR 4468, and (b) Oxirane ring opening via nucleophilic addition reaction in rPET filament extrusion

The local mobility of the polymer chain, as well as the T_g of rPET/ADR 4468, is affected by the amount of ADR 4468. The T_g of rPET/ADR 4468-1.5 wt% appears near 75.0°C, which is higher than the 72.5°C of rPET/ADR 4468-1.0 wt%. The high T_g of rPET/ADR 4468-1.5 wt% could be attributed to the limitations of the local mobility of the polymer chains with more crosslinked structures. The crosslinked structures are formed by the ring-opening reaction of the epoxy groups of ADR 4468 with the -OH end groups of the PET polymer chains. Since the PET chains are

connected to the networks that restrict their mobility, the crosslinked chains need more activation energy due to their local mobility which is shown as an increase in T_g. With the ratio of ADR 4468 further increasing, the T_g of rPET/ADR 4468-2.0 wt% declines and reverts back to a similar temperature as that of rPET/ADR 4468-1.0 wt%. This lowering of the T_g indicates a decrease in crosslinked structures, owing to the limited number of -OH end groups of the PET chains. The end groups might connect with the epoxy groups of ADR 4468 to extend the PET chains, and ADR 4468 might only react with one or two end groups due to the large number of epoxy groups in the free ADR 4468. The dominance of the epoxy groups reduces the likelihood of crosslinking and ratio of ADR 4468. With the crosslinking ratio reducing, the chain mobility of rPET/ADR 4468-2.0 wt% increases with T_g, thus returning to a similar value as that of rPET/ADR 4468-1.0 wt%.

Due to the trough-like crosslinks, the T_{cc} and T_m peaks exhibit similar trends with increase in ADR 4468. The intensity of the T_{cc} and T_m peaks of rPET/ADR 4468-1.5 wt% decreases and then increases with rPET/ADR 4468- 2.0 wt%. These two types of peaks are related to the crystallization of the polymer. The higher T_{cc} peak of rPET/ADR 4468-1.0 wt% and rPET/ADR 4468-2.0 wt% means that the polymer chains tend to crystallize due to the high chain mobility and low crosslinking ratio. The high chain mobility allows the chains to move faster and cold crystallize more rapidly during heating. Meanwhile, their higher peak for T_m indicates that they have more crystalline regions than rPET/ADR 4468-1.5 wt%, which corresponds to their higher intensity and area of crystal planes in the XRD results. Accordingly, the low

crosslinking ratio of rPET/ADR 4468-1.0 wt% and rPET/ADR 4468-2.0 wt% might increase chain mobility and crystallization with higher peak intensity of T_{cc} and T_m.

Remarkably, a downward trend of T_m was observed, from 259.0℃ for rPET/ADR 4468-1.0 wt% to 256.9℃ for rPET/ADR 4468-1.5 wt% and 256.7℃ for rPET/ADR 4468-2.0 wt%. This downward trend demonstrates that there might be residual internal stress in rPET/ADR 4468-1.5 wt% and rPET/ADR 4468-2.0 wt%. Since the residual stress declined before the crystalline regions melted, the stress decline would cause the chains to unfold earlier than their melting threshold and reduce the T_m with increase in internal stress. The reduced T_m suggests that the residual internal stress increases with increased amount of ADR 4468, which corresponds to the blue-shifting of the C-H stretching vibration in the FTIR results.

The endothermic broad peak of ADR 4468 (from about 222.3℃ to 290.6℃) indicates that the epoxy groups of ADR 4468 are activated and reacted during the extrusion (Zones II and III have a temperature over 225℃). The opened epoxy groups react with the hydroxyl end groups (-OH) of the PET polymer chains based on oxirane ring-opening via a nucleophilic addition reaction in an epoxide system (Fig. 4.5b)[87]. Since no free acid is available to protonate the oxygen of the epoxy groups before the ring opened, the oxygen of -OH group which acts as a nucleophile would attack the less inhibited epoxide C atom[88]. After chain extension, the PET polymer chain is linked with the less inhibited epoxide C atom of ADR 4468, and the hydroxyl group form connections with another C atom of the epoxy group. Since ADR 4468 contains two or more two epoxy groups, the PET polymer chains would be extended

and crosslinked after the oxirane ring-opening reaction[89]. The oxirane ring-opening reaction of the epoxy groups means that ADR 4468 could extend and crosslink with the PET chains during filament extrusion, thus increasing the extrusion flow of rPET/ADR 4468.

4.3.4 Rheological properties

The rheological properties of polyester textile, rPET/ADR 4468-1.0 wt%, rPET/ADR 4468-1.5 wt%, and rPET/ADR 4468-2.0 wt% were measured by using dynamic rheological tests including complex viscosity, storage modulus G', and loss modulus G'' (Fig. 4.6).

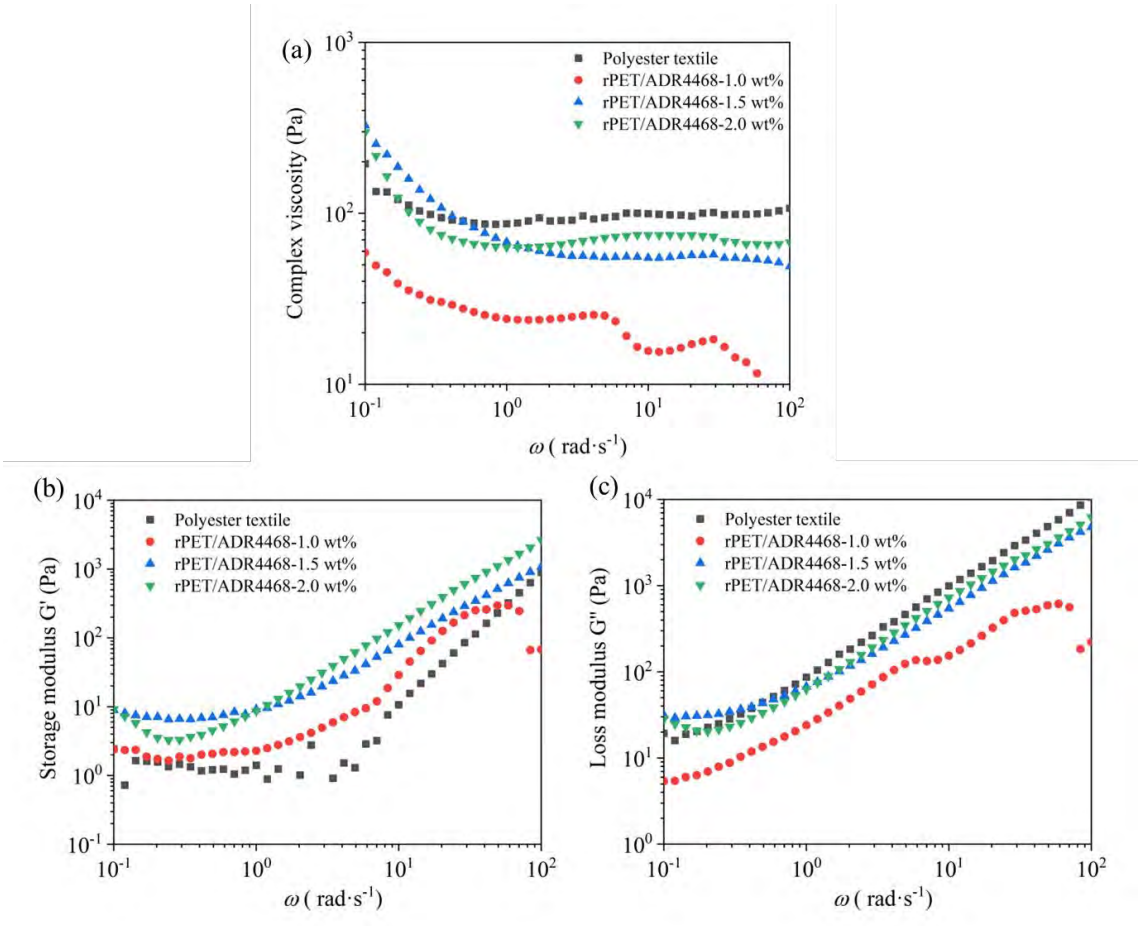

Figure 4.6. Complex viscosity-ω (a), storage modulus G'-ω (b), and loss modulus

G''-ω (c) curves of polyester textile, rPET/ADR 4468-1.0 wt%, rPET/ADR 4468-1.5 wt%, and rPET/ADR 4468-2.0 wt%.

The complex viscosity measures the total resistance to flow with isothermal measurements of the shear frequency (ω). Fig. 4.6a shows that the complex viscosity of the polyester textile and the rPET/ADR 4468 samples almost decreases with increases in ω due to the shear thinning characteristics of the pseudoplastic behavior of the polyester textile and rPET/ADR 4468. At the beginning of ω at 10^{-1}, the complex viscosity of rPET/ADR 4468-1.5 wt% and rPET/ADR 4468-2.0 wt% is higher than that of the polyester textile, owing to the existence of crosslinked structures. The crosslinked structures connect the polymer chains into networks, which inhibit the mobility of the polymer chain and increase the complex viscosity at the beginning of their flow. In the regions with a low ω value (10^{-1} to 10^{0}), the complex viscosity of the rPET/ADR 4468 samples is greatly decreased, and their rate of decrease increases with more ADR 4468. This steep reduction in the complex viscosity might be attributed to the relaxation of the internal compressive residual stress, which would relax and deform the polymer chains, thus causing further extension of the polymer chains under the shear stress. This further extension enhances the material response and reduces the mechanical resistance (complex viscosity) to the shear stress. Due to the high internal compressive residual stress, the complex viscosity of rPET/ADR 4468-2.0 wt% is further reduced to less than 1.5 wt% in the region with low ω values. In other words, the rPET/ADR 4468-2.0 wt% sample exhibits a higher flowability than the rPET/ADR 4468-1.5 wt% under a low

shear stress (region with low ω values). In the regions with a high ω values (10^0 to 10^2), all the rPET/ADR 4468 samples have a lower complex viscosity than the polyester textile. Moreover, the rPET/ADR 4468-1.0 wt% sample exhibited the lowest complex viscosity with a fluctuating trend of decrease. On the other hand, the complex viscosity of rPET/ADR 4468-2.0 wt% showed a slight upward trend from 10^0 to 10^1 and then declined. Due to the slight upward trend, the complex viscosity of rPET/ADR 4468-2.0 wt% is higher than that of rPET4468-1.5 wt%. This phenomenon is attributed to the increase in the resistance of the long-chain alkyl groups after the relaxation of the internal compressive residual stress. The extended chains are tangled up with the neighboring chains which resist mobility under shear stress, thus increasing the complex viscosity of rPET/ADR 4468-2.0 wt%.

The storage modulus G' represents the elasticity of the visco-elastic polymer melts. Fig. 4.6b shows that the storage modulus G' of the polyester textile and rPET/ADR 4468 samples almost increases with higher ω values, except for the trough of rPET/ADR 4468-2.0 wt% in the region with low ω values. The trough and plateau point to the presence and relaxation of internal compressive residual stress, respectively[90]. The latter induces extra strain and reduces the G', which corresponds to the dip at the beginning of the complex viscosity-ω curves. In the region with high ω values, the G' increases with increasing ω values due to the slow material response, thus exhibiting a solid-like mechanical performance with high rigidity. Remarkably, the G' of all of the rPET/ADR 4468 samples is higher than that of the polyester textiles. Meanwhile, the G' of the polyester textile shows an upward trend with more

ADR 4468, except for the region with lower ω values caused by the residual stress relaxation of rPET/ADR 4468-2.0 wt%. These increases in the G' suggest that ADR 4468 enhances the melt elasticity of PET which affects the filament extrusion to reduce the melt dropping behavior. At the end of the extrusion (Zone IV in Fig. 4.1), the rPET/ADR 4468 sample flowed through the narrow extrusion nozzle when it absorbed the compressive energy which converted the sample into melt and increased its elasticity. Before the sample increased in elasticity, it had to be cooled down to prevent the gravity-induced melt dropping. Due to higher elasticity, the rPET/ADR 4468 samples were successfully extruded and shaped into 3D-printable filaments.

The loss modulus G'' demonstrates the viscosity of visco-elastic polymer melts. Similar to the G' trends, the G'' of the polyester textile and rPET/ADR 4468 samples showed a slight upward trend with higher ω values (Fig. 4.5c), except for the trough of rPET/ADR 4468-2.0 wt% in the region with low ω values. The trough could be attributed to the relaxation of the residual stress, which induces extra strain and material response that reduces the viscosity. In the regions with higher ω values, the G'' of the rPET/ADR 4468 samples is lower than that of the polyester textile, which shows that the long-chains in the polyester respond slowly to the shear stress due to the tangled long-chains which restrict their mobility. The low viscosity means that the polymer chains of rPET/ADR 4468 samples might be shorter than those of the polyester textile, although ADR 4468 extends the chains. The shorter chains of rPET/ADR 4468-1.0 wt% might affect filament extrusion and effectively prevent the relaxation of the internal compressive residual stress after 3D printing.

4.3.4 Morphology observations

The fractured sections of the rPET/ADR 4468 samples show the fracturing mechanism and quality of the 3D printing. The morphology of the samples was analyzed by using an SEM (Fig. 4.7). Fig. 4.7a shows the continuous fractures in a section of rPET/ADR 4468-1.0 wt%. The continuous fractures indicate that the printed polymer is very much fused into printed lines without voids (implies high 3D printing quality), which means that rPET/ADR 4468-1.0 wt% offers a high mechanical performance. To explore the enhancement mechanism from the use of the material, Fig. 4.7d shows a rough morphology that is fish scale-like in the fractured section of rPET/ADR 4468-1.0 wt%. The fish-scales are produced and propagate during tensile fracturing which suggests that the material is irreversibly deformed and begins to yield when tension leads to the breaking point of the sample. The slight yielding uses more energy and improves the tensile performance.

With increased amounts of ADR 4468, the fractured section of rPET/ADR 4468-1.5 wt% shows obvious voids between the printed lines, especially at the connecting areas (overlapping zone) between the 3D-printed wall and infill (Fig. 4.7b). The increasing number of voids could be attributed to the high complex viscosity (Fig. 4.6a) of rPET/ADR 4468-1.5 wt% which reduces the flow of the melt when pushed through the printing nozzle. The low flow of the melt reduces the bond of the materials and produces the voids. Tensile stress is concentrated in the voids and

fractures are initiated. Upon further observing the surface of rPET/ADR 4468-1.5 wt% (Fig. 4.7e), a smaller fish-scale-like morphology appears and expands to the edge of the lines, which indicates that the voids inhibit the expansion of the morphology through energy absorption of the tension. Accordingly, the increasing number of voids greatly deteriorates the mechanical performance of rPET/ADR 4468-1.5 wt%.

When the amount of ADR 4468 was increased to 2.0 wt%, the printed lines merged again, and the number of voids was reduced, which means low complex viscosity in the region with low ω values. The low complex viscosity of rPET/ADR 4468-2.0 wt% increased the flow of the melt and allowed the melt to fuse with the printed lines. Moreover, this phenomenon suggests that the shear strength obtained through 3D printing might be similar to that at the regions of low ω values (10^{-1} to 10^{0} rad·s^{-1}) in the rheological test. This means that the internal compressive residual stress might be generated by compression of the melt at the nozzle (substantial shrinking from 2.0 mm to 0.4 mm) and relaxation of the stress after extrusion of the melt through the nozzle, which increases the flow of the melt and reduce the voids on rPET/ADR 4468-2.0 wt%. With fewer voids, the fish-scale morphology increases and expands on the fractured surface (Fig. 4.7f), at a scale in between that of the rPET/ADR 4468-1.0 wt% and rPET/ADR 4468-1.5 wt% samples. Therefore, fewer voids enhance the mechanical performance of rPET/ADR 4468-2.0 wt%.

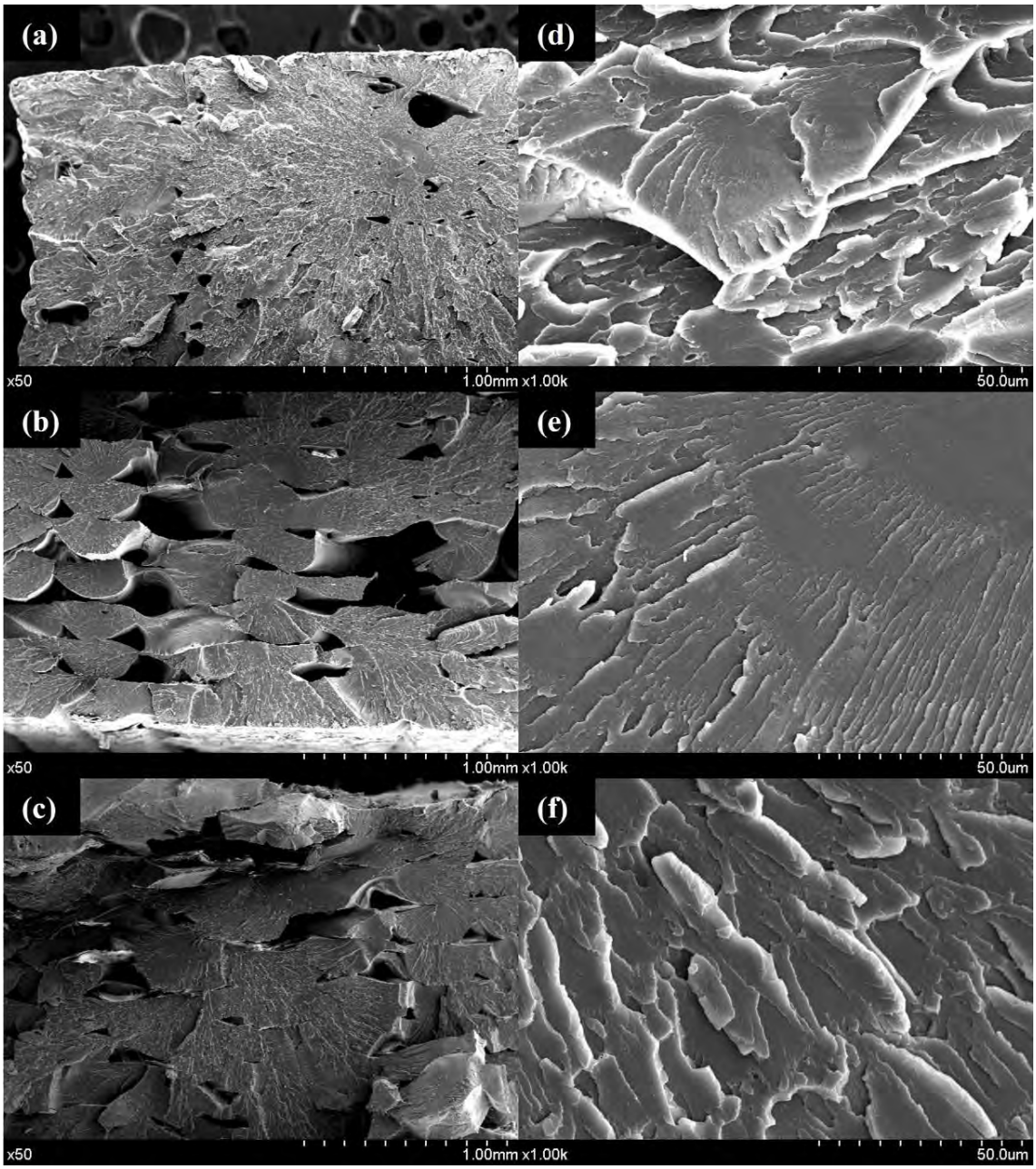

Figure 4.7. Fractured surface SEM image of 3D-printed tensile test samples: (a,d) rPET/ADR 4468-1.0 wt%, (b, e) rPET/ADR 4468-1.5 wt%, and (c,f) rPET/ADR 4468-2.0 wt%.

4.3.5 Mechanical performance analysis

To analyze the effect of the amount of ADR 4468 on mechanical performance, and tensile and compressive properties, testing was done in accordance with ISO 527-

2 / 5A / 10 and ISO 604 / B / 2, respectively. Fig. 4.8a shows the tensile properties with tensile strength, fracture elongation, and Young's modulus of rPET/ADR 4468-1.0 wt%, rPET/ADR 4468-1.5 wt%, and rPET/ADR 4468-2.0 wt%. Meanwhile, Fig. 4.8b shows the compressive properties with compressive strength, fracture elongation, and Young's modulus.

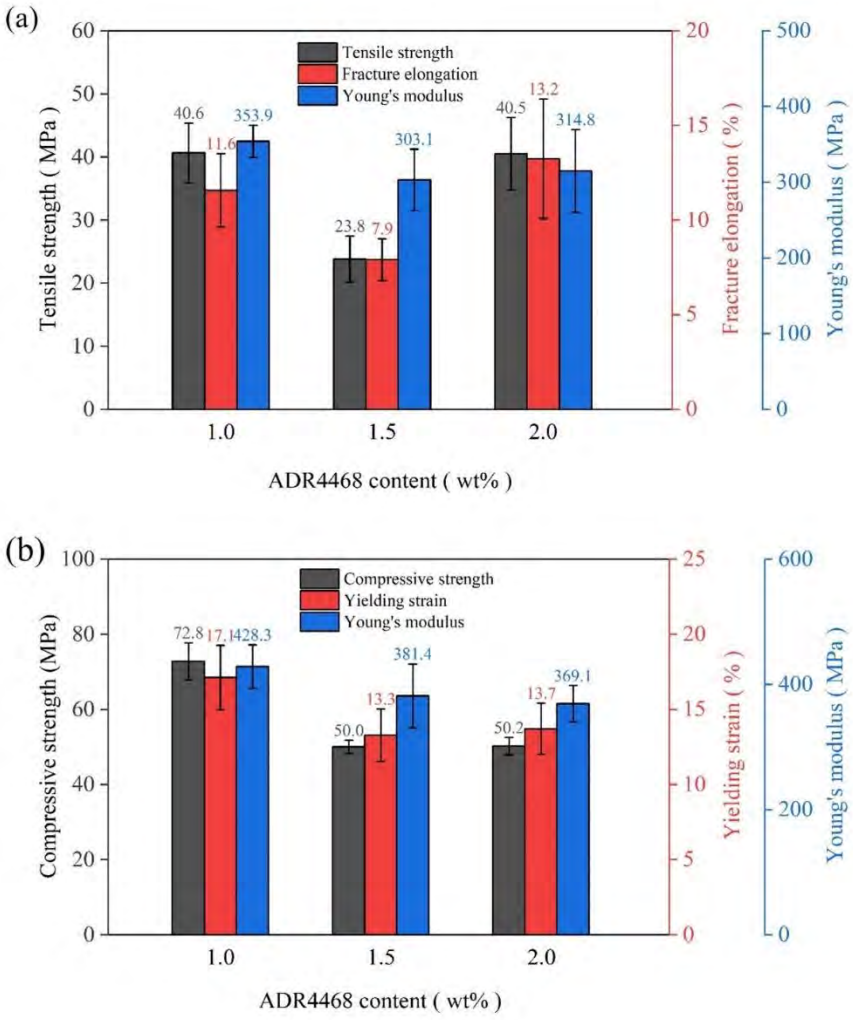

Figure 4.8. (a) Tensile and (b) compressive properties of rPET/ADR 4468-1.0 wt%, rPET/ADR 4468-1.5 wt%, and rPET/ADR 4468-2.0 wt%.

rPET/ADR 4468-1.0 wt% has the highest tensile (tensile strength of 40.6 MPa,

fracture elongation of 11.6%, and Young's modulus of 353.9 MPa) and compressive (compressive strength of 72.8 MPa, fracture strain of 17.1%, and Young's modulus of 428.3 MPa) properties, which correspond to the SEM analysis that the continuous and expanded fish-scale morphology of the fractured sections enhances the mechanical performance of the samples. Since the melt of the rPET/ADR 4468-1.0 wt% sample flows with ease (low complex viscosity), the melt could fill the printed area and merge with the printed lines to form a continuous section of fractures. Under tension, the continuous section of fractures allows the fish-scales to expand. The fish-scale morphology exemplifies the increase in polymer yield. During the straining, the polymer chains exhibit slight flexibility, owing to the chain extension induced by ADR 4468 with flexible long-chain alkyl branches. The chains non-reversibly deform to produce the fish-scales which impart toughness, thus absorbing tensile energy. The tensile energy could also be used through the propagation of the fractures in the amorphous regions to enhance mechanical performance. According to the high intensity of the characteristic peak at 25.8° of the PET (1 0 0) crystal plane (XRD results) and endothermic peak (melting) at ~259.0°C (DSC results), the rPET/ADR 4468-1.0 wt% contains many crystalline regions that are connected to the amorphous regions[91]. These crystalline regions resist the propagation of the fractures with less strain and bypass the extended propagation path of the fractures in the amorphous region to increase the energy absorption, thus increasing the mechanical strength and Young's modulus[92]. Thus, the propagation of the fractures in the amorphous regions and the slight surface toughness (fish-scales) improve the tensile properties of

rPET/ADR 4468-1.0 wt%.

Unfortunately, with increased ADR 4468 content, rPET/ADR 4468-1.5 wt% has a poor mechanical performance in terms of the tension and compression due to a high complex viscosity and poor crystallization. The high complex viscosity reduces the polymer melt in the printed areas and produces obvious voids between the printed lines. Fewer materials in the cross-section of 3D-printed samples directly deteriorate the mechanical performance. The generated voids lead to accumulation of stress and limit the spread of the fish-scales (material yielding), thus reducing energy absorption. Moreover, due to the low intensity of the crystal peaks (XRD results) and melting peak (DSC results), poor crystallization reduces and shrinks the crystalline regions, which deteriorate the resistance to fracturing, thus further reducing energy absorption. Therefore, high complex viscosity and poor crystallization erode the mechanical performance of rPET/ADR 4468-1.5 wt%.

rPET/ADR 4468-2.0 wt% exhibits high tensile strength (40.5 MPa) and low compressive strength (50.2 MPa), with enhanced mechanical performance owing to the internal compressive residual stress. According to the G' plateau in the region with lower ω values (Fig. 4.6b) and shifts of the C-H stretching vibration peak (red color) (Fig. 4.4b), internal compressive residual stress is found in rPET/ADR 4468-2.0 wt%[84, 90, 93-96]. The residual stress offsets the tensile forces and gradually relaxes (Fig. 4.9) when the tensile stress causes the 3D-printed samples to stretch. With increasing tensile stress, the polymer chains are even more elongated, thus resisting the tensile stress. When the tensile stress reaches the limitation for the deformation of the

polymer chains, the chains are broken, fractures propagate, and the samples are damaged. Although the rPET/ADR 4468-2.0 wt% samples contain voids, their tensile strength returns and increases with high strain due to the internal compressive residual stress. At the same time, this phenomenon lends support to the fact that the internal compressive residual stress decreases the compressive strength with less strain. Therefore, the internal compressive residual stress enhances the tensile properties and deteriorates the compressive properties of rPET/ADR 4468-2.0 wt%.

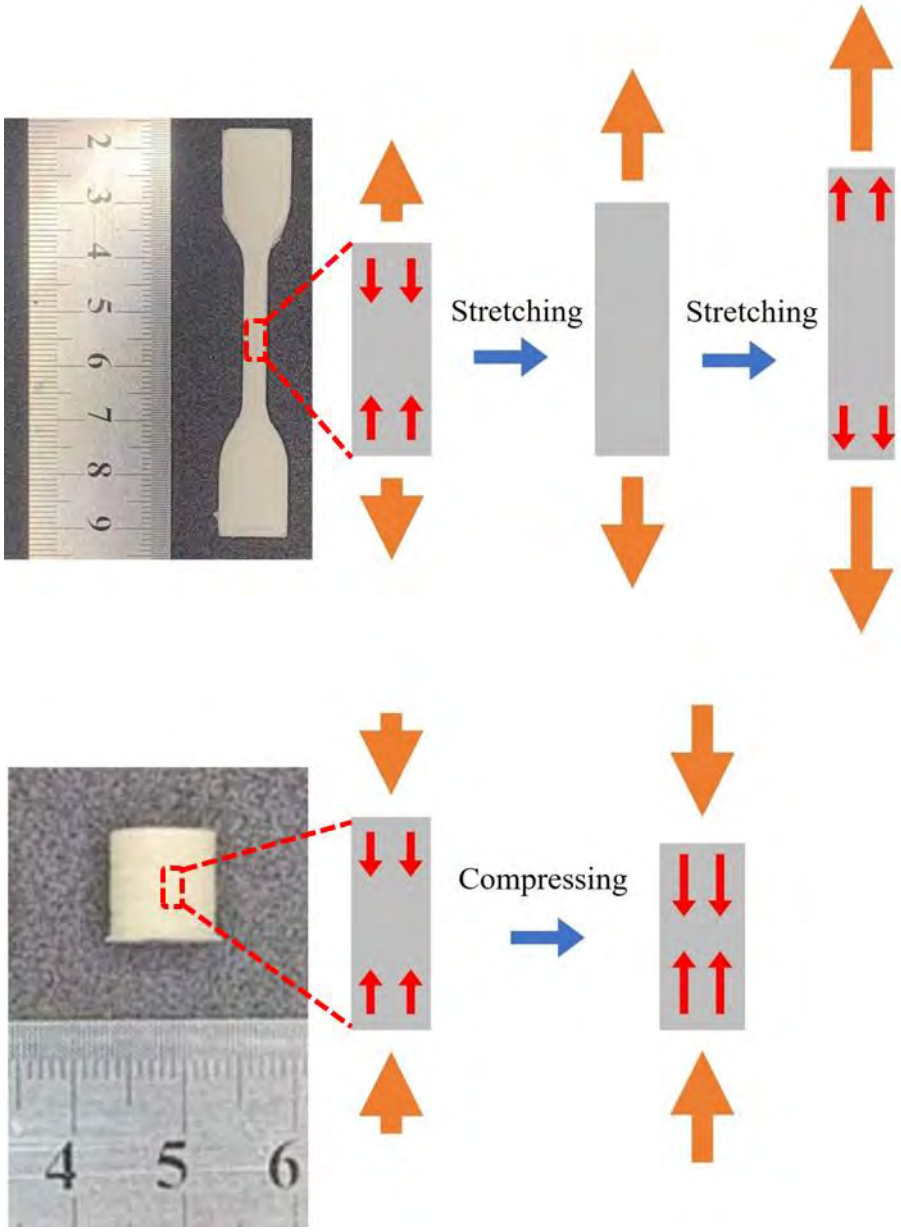

Figure 4.9. Stretching and compressing rPET/ADR 4468-2.0 wt% with internal compressive residual stress

4.4 Commercial competitiveness of rPET/ADR4468

Attractively, the rPET/ADR4468 3D printing products exhibited great flexibility compared with the commercial rigid 3D printing products including polyethylene terephthalate glycol (PETG), PLA, and PA in the FDM 3D printing market (Fig.

4.10). The low tensile strength and moderate elongation of rPET/ADR4468 3D-printed products indicated that they could deform larger than the commercial materials under low loading. They could be stretched over two times of the commercial rigid materials under similar or lower forces. It demonstrates that the rPET/ADR4468 has greater flexibility than the commercial rigid 3D printing materials. Accordingly, compared with the commercial rigid 3D printing materials, the rPET/ADR4468-1.0 wt% filaments might be suitable and have high competitiveness for 3D printing flexible products.

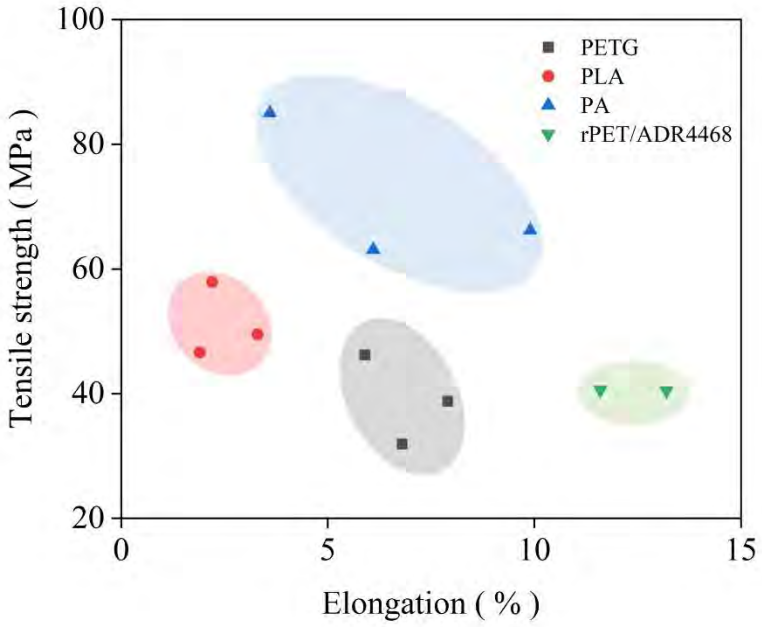

Figure 4.10. Mechanical properties of commercial filaments and rPET/ADR4468 filaments.

4.5 Summary

In this work, an approach to recycling polyester textiles into 3D printing filaments for 3D-printed textiles has been designed and implemented. As an important

additive for recycling polyester textiles, ADR 4468 extends the polyester chains and enhances the visco-elasticity of rPET/ADR 4468 melt in rPET/ADR 4468 filament extrusion. rPET/ADR 4468-1.0 wt% offers optimal mechanical performance under tension and compression for higher-loading products. With more ADR 4468, crosslinked structures are produced, thus inhibiting the mobility of the polymer chains, and causing internal compressive residual stress. The stress enhances the flowability of rPET/ADR 4468-2.0 wt% to fill the printed areas, thus directly increasing the material in the cross-section to resist tension and compression. Furthermore, the internal compressive residual stress enhances the tensile strength and reduces the compressive strength of rPET/ADR 4468-2.0 wt%. This result might be useful for presetting the loadings to improve the uniaxial tensile strength of 3D-printed products. Meanwhile, due to the stress relaxation under heating, rPET/ADR 4468-2.0 wt% could be applied to 4D printing. According to the results of this study, the approach is a practical way to recycle polyester textiles into 3D printing filaments to 3D print textiles, which would increase the recycling rate of polyester textiles to not only reduce material use and waste but also prevent environmental pollution with reduced disposal of polyester textile waste.

Chapter 5. A Filament Production Approach to Recycling Thermoplastic Polyurethane Film for 3D Printing

This chapter discusses the characterization results of TPU and 3D-printed rTPU samples. The rTPU was directly recycled by TPU films. To evaluate their mechanical performance and investigate the recycling stability of TPU films, the mechanical properties, thermal performance, morphology, and bonding configurations were analyzed.

5.1 Introduction

Thermoplastic polyurethane (TPU) films have been widely applied as highly elastic and waterproof fabrics for raincoats, umbrellas, and shower curtains. As a result of these fabric applications, TPU film waste is found in post-consumer textile wastes with other textiles. With the rapid development of TPU fabrics, TPU film waste will increase in the coming years.

Recycling TPU films is a sustainable method of disposing TPU films from textile waste, which increases the recycling rate of textile waste and reduces the environmental load caused by the landfill disposal (57%) or incineration (25%)[30] of textile waste. To stimulate TPU recycling, a high-value-added approach is critical, timely, and essential to face the oncoming challenges.

Three-dimensional (3D) printing may be the most viable method to realize high-value-added recycling. As 3D printing has captured commercial interest for printable

materials, it is a potential option for recycling TPU film waste. Although TPU is a thermoplastic and easily reprocessed by mechanical methods, most TPU materials are depolymerized into oligomers via chemical methods for new products. These chemical methods use chemicals and solvents that result in lower recyclability and an increased risk of secondary pollution. Accordingly, mechanical methods may be more suitable for recycling TPU film waste into 3D printing filaments.

In this work, TPU film waste was recycled into 3D-printable materials by direct filament extrusion without any additives. To evaluate the filament storage environment effect on the 3D printing of recycled TPU filament, the recycled TPU filaments were stored under open-air and dry conditions. The filaments were then 3D-printed into samples for mechanical performance tests. Meanwhile, the recyclability of TPU film waste was evaluated through various characterization methods, including differential scanning calorimetry (DSC), Fourier-transform infrared spectroscopy (FT-IR) analyses, rheological tests, and scanning electron microscopy (SEM) observations.

5.2 Method

5.2.1 TPU film recycling

Fig. 5.1 shows the recycling approach where TPU film waste is transformed into 3D printing filaments. Before the reprocessing commenced, the film waste was washed and dried at 50℃ overnight to remove dust from the film surface. The clean films were then shattered into plastics. To transform the TPU plastics into 3D printing

filaments, the plastics were fed into a WSJ-12 filament extruder (Xinsuo, Shanghai, China), which further melted the plastics into a thermoplastic fluid. The thermoplastic fluid was then pushed out of the extruder, pulled through the die into the water tank, and cooled in deionized water (25℃). The diameter of the filaments was 1.75 mm with good roundness, which corresponded to 3D-printable filament diameters that ranged from 1.25 to 2.00 mm. Table 5.1 lists the parameters for the optimal filament extrusion of TPU-based thermoplastics. In Table 5.1, Zones I to IV are the die, metering, compression, and feeding zones, respectively, marked on the extruder in Fig. 5.1. After rolling, the rTPU filaments were obtained for 3D printing.

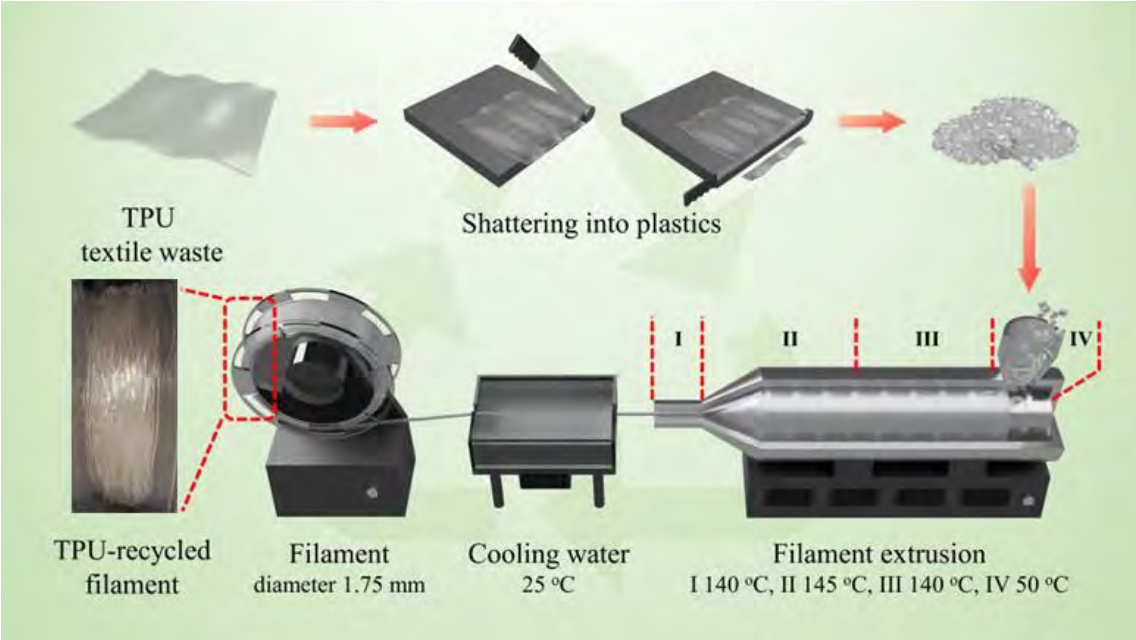

Figure 5.1. Fabrication of rTPU filaments.

Table 5.1. Major parameters of rPET/ADR 4468 filament extrusion

Extrusion parameter	Value
Zone I temperature	140℃
Zone II temperature	145℃
Zone III temperature	140℃
Zone IV temperature	50℃
Cooling water temperature	25℃
Screw speed	60 rad/min

Note: Zones I, II, III, and IV respectively denote the die, metering, compression, and feeding zones.

5.2.2 3D printing using rTPU filament

To determine the material properties, the rTPU filament was 3D-modeled and 3D-printed into standard samples (Fig. 5.2). The 3D models were designed and built with Pro/Engineer, a 3D modeling software (Parametric Technology Corporation Creo, Massachusetts, USA) according to testing standards. The Pro/Engineer software exported the 3D models into STL files for the 3D printing slicer software - Cura (Ultimaker B.V., The Netherlands), slicing the models into layers. However, the 3D-printed parts had empty spaces, so an infill pattern was needed. Patterned lines were used to fill the parts that were 3D-printed and the nozzle extrusion path. Moreover, the slicer software sets the 3D printing parameters based on the material characteristics of the filaments, which directly determine the quality and outcome of the 3D printing (Table 4.2). After setting the parameters, the slicer software converted

the modeled parameters into GCODE files. GCODE is a programming language that controls the filament-based FDM 3D printer (JGMaker-A6, JG AURORA, Shenzhen, China) to print the samples according to the sliced models. After printing, the samples were cooled to 25℃ and removed from the print plate to reduce the potential deformation of the samples. To explore the use of 3D printing techniques for the fashion industry, a flexible textile was printed as a prototype (Fig. 5.2).

Figure 5.2. 3D printing and 3D-printed samples using rTPU filament.

Table 5.2. 3D printing parameters for rTPU 3D-printed samples

3D printing parameter	Value
Layer height	0.2 mm
Wall thickness	0.8 mm
Infill density	100%
Infill pattern	Lines
Printing temperature	180℃
Build plate temperature	60℃
Flow	110%
Printing speed	30 mm/s

5.2.3 Characterization

Several characterizations were performed to investigate the effect of the filament storage environment on the 3D-printed TPU filament and the recyclability of TPU film waste, including the chemical structures, thermal performance, morphology, and mechanical performance of TPU.

The chemical structures of the TPU films and the 3D-printed samples were identified using an FT-IR spectrometer (ALPHA II, Bruker Co., Massachusetts, USA). The thermal performance of the TPU films and 3D-printed samples were examined by DSC (DSC4000, PerkinElmer, Massachusetts, USA) from 0℃ to 200℃ at a heating rate of 10℃/min under a nitrogen gas flow of 20 ml/min. The cross-sectional morphology of the 3D-printed samples was observed by SEM (S3400, Hitachi High-

Tech Co., Tokyo, Japan) at 20 kV for tensile stress. The mechanical performance of the 3D-printed samples was tested by comparing the tension and compression strengths (E43, MTS System Co., Minnesota, USA). The tensile tests were conducted in accordance with the ISO 527 standard at a displacement rate of 10 mm/min, while the compression tests were based on the ISO 604 standard at a rate of 2 mm/min.

5.3 Results and discussion

5.3.1 Chemical structure identification

The bonding configurations of the TPU film and rTPU 3D-printed samples were characterized by FT-IR spectroscopy (Fig. 5.3a). The TPU film and rTPU curves had characteristic TPU peaks of diphenylmethane diisocyanate (MDI, hard segments) and polyester (soft segments).

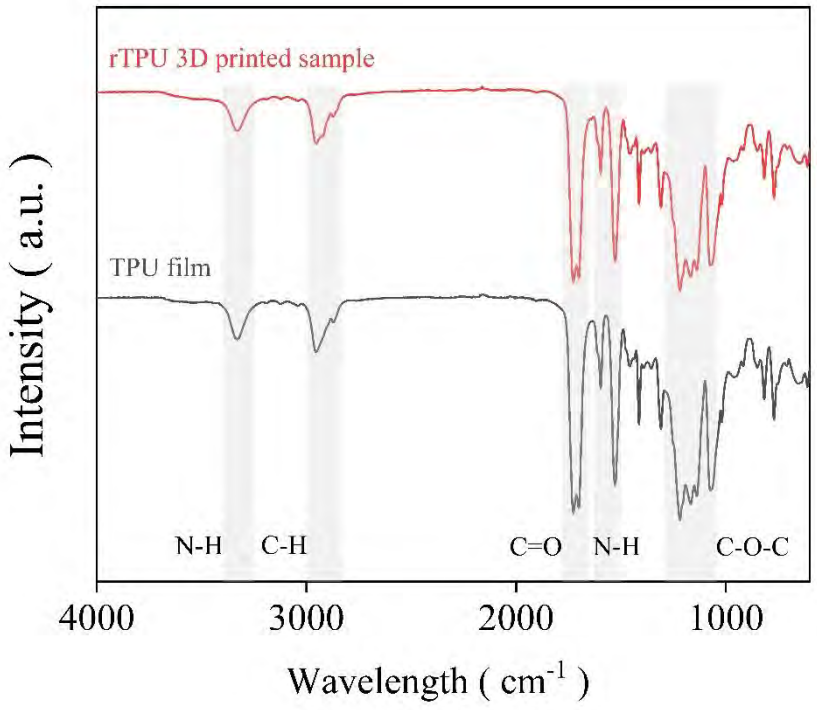

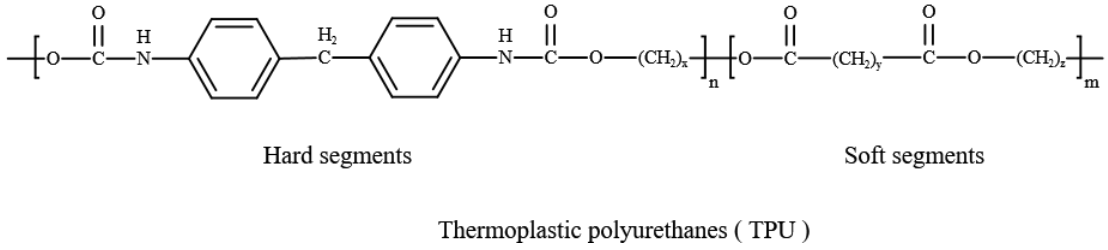

Figure 5.3. (a) FT-IR spectra and (b) chemical structure of the TPU film and rTPU 3D-printed sample.

Fig. 5.3a shows the characteristic peaks of the TPU film and rTPU 3D-printed samples. A broad N-H stretching vibration peak appeared at 3330 cm^{-1}, and C-H stretching vibration peaks were found at 2954 cm^{-1} and 2873 cm^{-1}. A split peak at 2920 cm^{-1} was observed in rTPU 3D-printed curves, which can be attributed to the internal tensile residual stress red-shifting of the C-H stretching vibration after filament extrusion and 3D printing. C=O stretching vibrations at 1726 cm^{-1} (ester groups) and 1701 cm^{-1} (carbamate groups) appeared as sharp shoulder peaks. N-H in-plane deformation vibration (N attached to the C of an aromatic ring) was located at 1610 cm^{-1} and 1596 cm^{-1}. A combination of N-H deformation and C-N stretching vibration appeared at 1528 cm^{-1}. The C-H bending vibrations of CH_2 or CH_3 asymmetric bending (overlaps band) were located at 1458 cm^{-1}, 1438 cm^{-1}, and 1413 cm^{-1}; the C-H bending vibration of CH_3 symmetric deformation appeared at 1390 cm^{-1}; and the C-H wagging vibration of CH_2 out-of-plane deformation was found at 1355 cm^{-1}. Mixed N-H bending and C-N stretching vibrations were found at 1310 cm^{-1}, and the C-O-C stretching vibrations of esters were observed at 1248 cm^{-1}, 1219 cm^{-1}, 1167 cm^{-1}, 1139 cm^{-1}, and 1073 cm^{-1}. Peaks corresponding to the C-H bending deformation

of ring hydrogens were located at 1019 cm^{-1} and 961 cm^{-1} (in-plane bending) as well as at 916 cm^{-1} (out-of-plane bending), while the C-H wagging vibrations of ring hydrogens were found at 848 cm^{-1}, 817 cm^{-1}, and 769 cm^{-1}. The CH_2 in-plane rocking vibrations of $(CH_2)_n$ ($n \geq 3$) resulted in a peak located at 750 cm^{-1}. The ring deformation vibration of 1,4-disubstituted benzene was detected as a weak peak at 710 cm^{-1} due to differences between the two substituents, while the N-H out-of-plane deformation vibrations of an amide group were found at 652 cm^{-1} and 610 cm^{-1}.

According to these characteristic peaks, the polymeric chains (Fig. 5.3b) of the TPU film and rTPU 3D-printed samples consisted of the esters which were synthesized using MDI (hard segments) blocked with polyester (soft segments).

Diphenylmethane diisocyanate (MDI, hard segments): The N-H stretching vibration at 3330 cm^{-1} suggests that -NH- exists in the TPU polymer chains (-NH_2 peaks near 3500 cm^{-1} and 3400 cm^{-1})[85]. The very strong intensity of the C=O stretching vibration at 1701 cm^{-1} without characteristic carboxylic acid peaks demonstrates that C=O combined with -NH- to form carbamate groups (amide C=O stretching vibration at 1680-1650 cm^{-1}). The high peaks of N-H deformation and mixed C-N stretching vibrations at 1610 cm^{-1} and 1596 cm^{-1} indicate that the N atom attached to the C atom of the aromatic ring as R-Ph-NH-(C=O)-O- (characteristic peaks near 1650-1590 cm^{-1}). In addition, the C-H wagging and ring deformation vibrations of 1,4-disubstituted benzene were observed, suggesting that the benzene ring connected two different substituents. Based on the reported TPU synthesis[61], MDI exists in the hard segments. Considering the reported FT-IR spectra of MDI-

based TPU[97], the TPU, rTPU filament, and 3D-printed rTPU samples contained MDI-based hard segments.

Polyester (soft segments): The very strong intensity of the C=O stretching vibration at 1726 cm^{-1} without the characteristic carboxylic acid peaks was attributed to the ester groups[85]. Considering the structure of commercial TPU, the polyesters consisted of soft segments. The CH_2 rocking vibration at 750 cm^{-1} suggests that the *x*, *y*, and *z* values of the CH_2 chains were similar and are greater than or equal to 3. Since the CH_2 rocking vibration is at ~720 cm^{-1} when the carbon chain is in the crystalline state, the CH_2 chains of soft segments are in the amorphous area to increase the elasticity of TPU.

Based on the FT-IR spectra, the chemical structures of the TPU film and rTPU 3D-printed samples were identified as MDI-b-polyester. These blocked polyesters contained long alkane chains, which endowed the polymer with high elasticity. Additionally, the similar spectra of the TPU film and rTPU 3D-printed samples suggests that the MDI-b-polyester of the TPU film was stable during filament extrusion and 3D printing, which is suitable for mechanical recycling.

5.3.2 Thermal performance

The thermal performance of the TPU film and 3D-printed rTPU samples were examined. The first heating DSC curves include the respective melt temperatures of the soft and melt hard segments (Fig. 5.4). The soft segments of the TPU film and 3D-printed rTPU samples were melted at ~58.0℃, which were observed as broad peaks

in the DSC curves. The low melting point of the soft segments caused feeding problems. As the temperature approached the first melting point of TPU, the TPU became sticky and over-elastic. It could not be shattered by the screw of the filament extruder and would stick at the feeding area, blocking the feed port and causing the extrusion to fail. For this reason, the Zone IV temperature was set 50℃ below the soft segment melting point. The hard segments melted at ~153.3℃ with a board peak in the DSC curves. When the temperature was below the hard segment melting point, the hard segments would self-assemble with nearby hard segments of other polymer chains and form crosslinked structures to stabilize the polymer melt as a continuous fluid for filament shaping. Accordingly, the filament extrusion temperatures were lower than the second melting point to produce fine rTPU filaments. However, this property blocked the narrow nozzle of the 3D printer. For this reason, the 3D printing temperature was set 180℃ above the hard segment melting point to print high-quality products.

Additionally, the DSC curves of TPU film and rTPU 3D-printed samples were similar, which indicated that the TPU film was stable in the filament extrusion and 3D printing without any side reactions at temperatures ranging from 0℃ to 200℃. The TPU film was suitable for mechanical recycling, and its processing temperature could range from 140℃ (for filament extrusion) to 180℃ (for 3D printing).

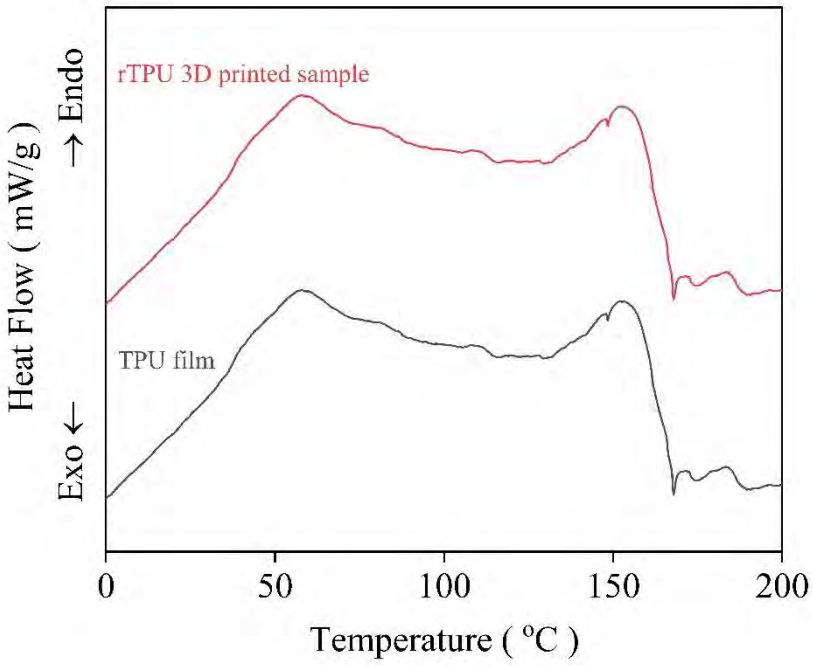

Figure 5.4. First heating DSC curves of the TPU film and rTPU 3D-printed samples.

5.3.3 Morphology observation

The morphology of the fracture surface of the rTPU 3D-printed ISO527-2/5A sample was analyzed by SEM (Fig. 5.5). The fracture surface contained rTPU lines merged as a continuous cross-section (Fig. 5.5a).

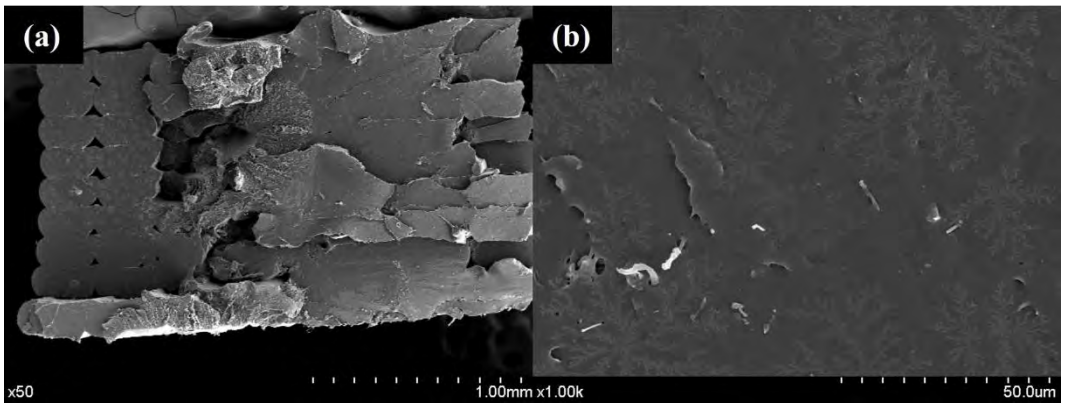

Figure 5.5. Fracture surface SEM of rTPU 3D-printed specimens after tensile test.

Small voids appeared between the printed wall lines, and their size gradually grew with increasing layers. This phenomenon can be ascribed to the lower surface temperature. When the rTPU was printed at higher layers, the cooling speed of the printed layers was faster than that of the lower layers[96]. The high cooling speed restricted the relaxation of the rTPU melt in the printing area, which quickly froze without merging with the nearby frozen lines and generated bigger voids than the lower layers. Since the cooling speed of the infill area was lower than the wall area, the inner area avoided void generation and formed a continuous cross-section.

The wall lines fractured, forming smooth surfaces, and the infill lines contained fish-scale-like structures on their surfaces. The smooth fracture surface suggests that brittle fracture occurred on the wall lines, via stress concentrations. Stress became concentrated on the wall lines when the tensile force was applied, as the voids hindered the force spread across the wall lines. Thus, the concentrated stress increased rapidly with less time for the polymer to respond or yield to fracture wall lines with smooth surfaces. Additional dendritic crystals formed in the wall lines, which had bigger voids nearby due to the rapid crystal growth in the dominant direction of concentrated stress (Fig. 5.5b). In the infill area, the stress spread in the continuous cross-section, which allowed the polymer to deform and yield. This also generated fish-scale-like structures on the fracture surfaces, causing ductile fracture.

5.3.4 Tensile properties

The tensile properties of the rTPU 3D-printed samples were examined according

to the ISO 527-2 / 5A / 500. Fig. 5.6 shows the tensile strength, fracture elongation, and Young's modulus of rTPU printed using undried filament and 48h-dried filament.

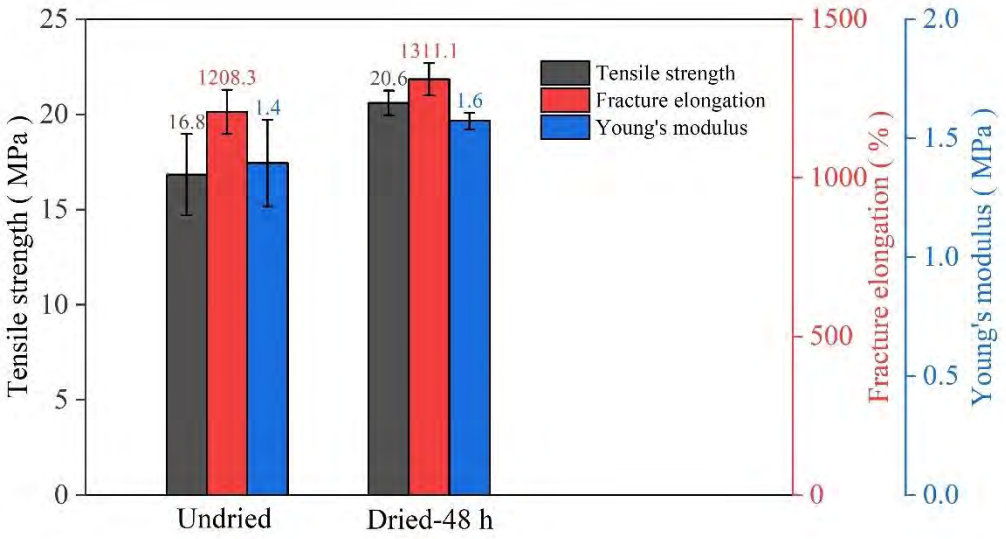

Figure 5.6. Tensile properties of rTPU printed using undried filament and 48h-dried filament.

The rTPU 3D samples printed using undried rTPU filaments had tensile strength, elongation at break, and Yong's modulus values of 16.8 MPa, 1208.3%, and 1.4 MPa, respectively, with medium standard deviation. Using dried filament, the tensile strength improved to 20.6 MPa, the elongation increased to 1311.1%, and Young's modulus rose to 1.6 MPa with low standard deviation. The high mechanical performance and low standard deviation demonstrate that the filament drying process can improve the quality of the 3D-printed products, which can be attributed to the higher modulus of the filament stabilizing the feeding of the 3D printer. The drying process increased the modulus of the TPU filament[98], reducing the deformation when the filament was drawn by the feeding gears of the 3D printer. Since the feed rate was

calculated by the filament diameter, the low filament deformation allowed the shape and diameter of the filaments to be maintained to stabilize the feed rate of the materials. Accordingly, the dried TPU filaments have a higher Young's modulus and deform less, improving the stability of gear feeding during the 3D printing process. The high feed stability enhanced the mechanical performance and reduced its standard deviation, improving the 3D printing quality. Therefore, drying the filament before 3D printing improved the mechanical performance and quality of the rTPU 3D-printed products.

5.4 Commercial competitiveness of rTPU

Remarkably, the rTPU 3D-printed products exhibited high flexibility compared with commercial TPU products in the fused deposition modeling 3D printing market (Fig. 5.7). The low tensile strength and high elongation of rTPU 3D-printed products revealed that they could undergo more extensive deformation, as they can be stretched over three times longer than commercial TPU materials under similar or lower forces. It demonstrates that the rTPU has greater flexibility than the commercial TPU 3D printing materials. Compared with commercial 3D-printed TPU materials, the rTPU filaments are more suitable and have high competitiveness for flexible 3D-printed textiles.

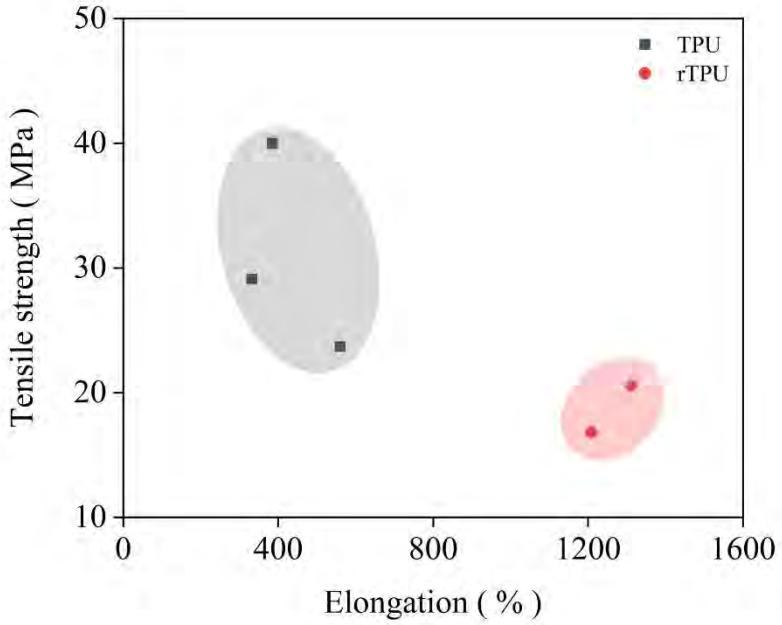

Figure 5.7. Mechanical properties of commercial TPU filaments and rTPU filaments.

5.5 Summary

The MDI-polyester-based rTPU filament can be directly produced by TPU films without additional additives, which suggests that the material of the TPU film has high filament extrusion processability and is suitable for mechanical recycling. The high elongation at break of the 3D-printed products demonstrates the elasticity of rTPU still has attractive elastic properties with high competitiveness after recycling and 3D printing processes. The similar FTIR and DSC results of the TPU film and TPU 3D-printed samples also demonstrate their thermal stability to maintain their chemical structures stable during filament extrusion and 3D printing. Additionally, the 3D-printed samples using 48-hour-dried TPU filament presented higher tensile strength and lower standard deviation with undried filament. Therefore, drying the filament before 3D printing can improve the mechanical performance and quality of

the rTPU 3D-printed products. Additionally, the small voids between the printed lines (SEM results) support the high quality of the rTPU 3D-printed products using dried filaments. Thus, the TPU film is suitable for mechanical recycling into filaments for 3D printing, while the filament drying process can further improve the mechanical performance and quality of the rTPU 3D-printed products. Moreover, the high competitiveness of the soft rTPU 3D-printed products can stimulate the recycling of TPU films from post-consumer textile waste, saving material resources and reducing the environmental load of waste disposal.

Chapter 6. 3D Printing Flexible Textile Using Polyester-Textile-Recycled Filaments

This chapter discusses the mechanical performance of 3D-printed flexible textiles using rPET/ADR4468-1.0 wt% filament. The polyester filament was printed into flexible textiles according to the designed textile structures. The textile structures were program-generated by changing the infill pattern parameters of Cura slicer software. To evaluate the mechanical performance and demonstrate the relationship between the 3D-printed structure and the mechanical properties, the effects of infill densities, rotation angles, and intersection angles on 3D-printed textiles were investigated.

6.1 Introduction

The circular economy approach involves recycling polyester textiles into polyester filaments and applying polyester filaments to fabricate 3D-printed textiles, forming a circular approach for polyester textiles. To close the loop of polyester recycling, the use of polyester filament in 3D printing textiles should be investigated.

3D-printed textiles are produced using 3D printing techniques to reproduce essential textile properties, such as elasticity, flexibility, strength, and porosity[99]. The techniques use structure design and 3D modeling to simulate the traditional woven or knitted structures and develop novel textile structures having similar properties to the traditional textile[100]. The development of 3D printing techniques and the high

resolution, high precision, and novel materials of 3D printing allow designers to overcome the challenge of small-size and complicated textile structures and explore the possibility of functionalization, thereby enhancing essential textile properties[101-109].

However, the cost and the technical requirements limit the production and development of 3D-printed textiles. The weaving and knitting textiles contain many voids, thus requiring supports to be printed layer by layer. The selective laser sintering (SLS) 3D printing technique has been widely used for producing 3D-printed textiles to eliminate or minimize the post-processing supports[110]. Compared with traditional textiles, the cost of SLS remains relatively high for producing 3D-printed textiles with essential structures. Thus, SLS 3D printing technique is currently used to produce prototypes with complicated textile structures.

FDM 3D printing technique is a promising cost-effective technique for producing customized printing on spectacle frames[17], tools, accessories, garage kits, and gears[111]. In addition, FDM 3D printing farms can significantly reduce supply chain costs, thus attracting factories to build FDM 3D printing farms for fabricating customer-designed products. This affordable technique can be used to produce cheap 3D-printed textiles with essential structures, which can replace traditional textiles. With the open-source 3D model and hands-on slicer software, the 3D-printed textiles are attempted at home and shared by tech geeks.

The infill pattern generation method can further decrease the technical threshold and reduce the cost of 3D-printed textiles. In Cura slicer, the infill area can be

customized using several parameters, including infill density, pattern, and line directions. These parameters automatically generate the 3D printing patterns by slicer program on the thin board models to form the 3D-printed textiles without top and bottom layers. This infill pattern program-generated method can prevent complicated 3D modeling of 3D-printed textiles, thus simplifying the processes and reducing the technical threshold.

In this work, the textile structure was program-generated by setting infill pattern parameters in the 3D printing slicer software. After the structural design of the textile, the textiles were 3D-printed using polyester-textile-recycled filaments to finish the circular approach. To investigate the effect of textile structures on mechanical performance, the KES-F system was used to evaluate the mechanical performance of textiles at different infill densities, rotation angles, and intersection angles.

6.2 Method

6.2.1 Materials

The polyester-textile-recycled filament was produced by Biofuels Institute, School of the Environment and Safety Engineering, Jiangsu University. The filament was stored at 25℃ and 65% relative humidity over two days before 3D printing.

6.2.2 Textile structure design

The textile structure was program-generated at different infill densities, rotation angles, and intersection angles using Cura 3D printing slicer software (Ultimaker B.V.,

the Netherlands), shown in Fig. 6.1. Cura optimized 3D printing paths and generated patterns on 0.6 mm high solid sheet 3D models. The model height (0.3 mm) allowed two layers to form the textile structures through 3D printing. The default textile structure was program-generated at 50% infill density, 45° rotation angle, and 90° intersection angle. The infill densities were set at 30%, 50%, and 70% to evaluate the effects of the above parameters on textile mechanical properties. The rotation angles were set as 0°, 15°, 30°, and 45° by changing the infill line directions into [0, 90], [-15, 75], [-30, 60], and [-45, 45]. The intersection angles were set as 30°, 60°, and 90° by changing the infill line directions into [-15, 15], [-30, 30], and [-45, 45].

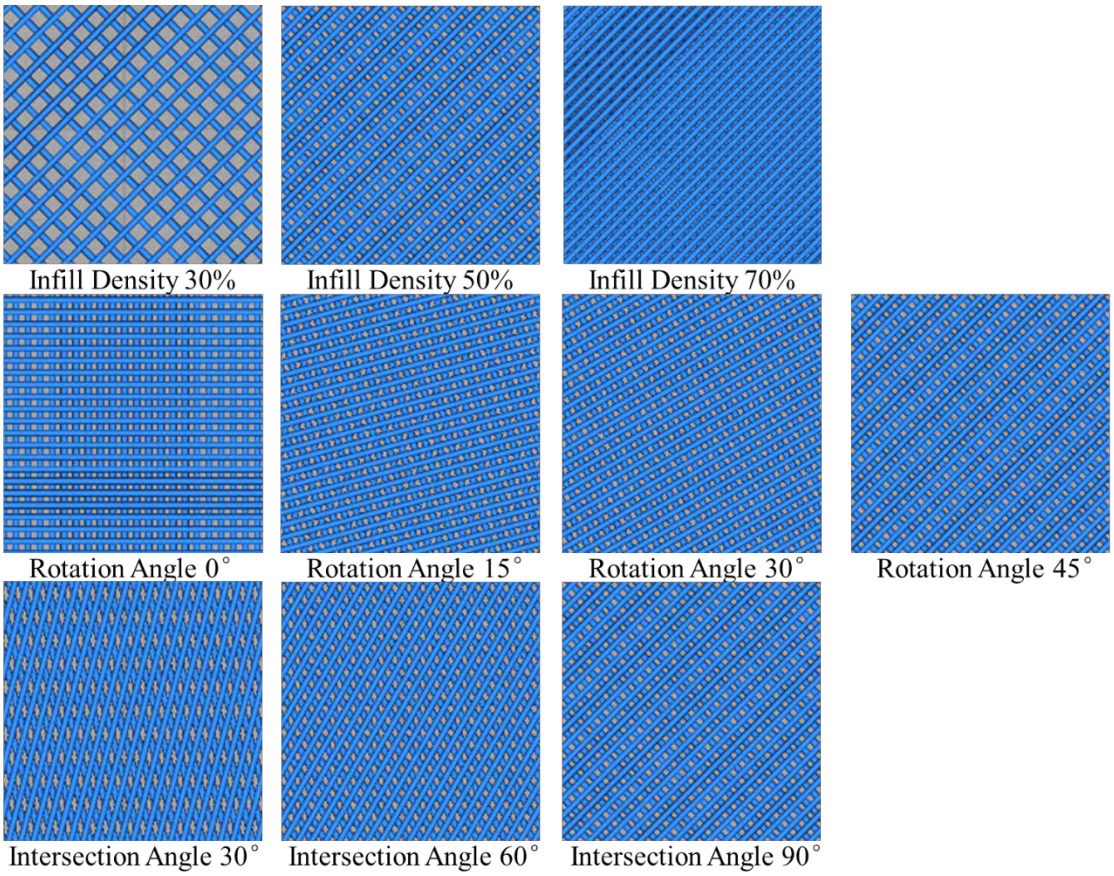

Figure 6.1. Program-generated textile structures of rPET/ADR4468 3D-printed textile samples.

6.2.3 3D printing using polyester filament

Fig. 6.2 shows the program-generated structures printed into 100 mm long, 100 mm wide, and 0.6 mm high patterned textiles. The thin solid sheet models were built with Fusion 360, a 3D modeling software (Autodesk Inc., San Francisco, USA). The Fusion 360 software exported the thin sheet models into STL files for the Cura slicer to generate the patterns in the sheets. The infill patterns were set according to structure design by changing the infill density and line directions. To focus on the structural effect, the wall line count was zero, printing the textiles without the outer wall structures. The patterned lines were used for 3D printing or nozzle extrusion path. Moreover, the slicer software sets the material parameters according to the recommended parameters of polyester filaments. These parameters directly impacted the quality of 3D-printed textiles (Table 6.1). After the parameter setting, the slicer converted the models and printing parameters into GCODE files. The GCODE files planned the printing path with printing parameters for the filament-based FDM 3D printer (JGMaker-A6, JG AURORA, Shenzhen, China) to produce the patterned textiles. After the printing of textiles, they were cooled to 25℃ to prevent deformation when removing them from the print plate.

Figure 6.2. 3D printing of rPET/ADR4468 textile samples with program-generated patterns.

Table 6.1. 3D printing parameters for rPET/ADR4468 3D-printed textile samples

3D printing parameter	Value
Layer height	0.3 mm
Wall thickness	0 mm
Top/Bottom thickness	0 mm
Infill pattern	Lines
Printing temperature	270℃
Build plate temperature	70℃
Flow	110%
Printing speed	30 mm/s

6.2.4 Characterization

Mechanical measurements were conducted to investigate the effects of the infill density, rotation angle, and intersection angle on the mechanical properties of textile structures. The textiles were stored at 20℃ and 65% relative humidity over 24 h for Kawabata evaluation (KES-F) system testing. The KES-F system was used to test the mechanical properties, including tensile, shear, bending, and compressive properties, of each textile structure in warp and weft directions at 20℃ and 65% relative humidity.

The tensile properties were measured using KESFB1-AUTO-A automatic tensile and shear tester (Kato Tech Co., LTD, Kyoto, Japan) under the optional condition. The

sample testing length and width were 5 cm and 10 cm, respectively. The maximum tensile load was 500 gf·cm^{-1}, the tensile velocity was 0.2 mm·s^{-1}, and the maximum elongation was 25 mm.

The shear properties were evaluated using KESFB1-AUTO-A automatic tensile and shear tester under the optional condition. The sample testing length and width were 5 cm and 10 cm, respectively, the shear tension was 10 gf·cm^{-1}, and the maximum shear angle was from 8° to -8°.

The bending properties were characterized using a KES-FB2 pure bending tester (Kato Tech Co., LTD, Kyoto, Japan) under the optional condition. The sample testing length and width were 1 cm and 20 cm, respectively. The maximum bending load and curvature were 5 gf·cm·cm^{-1} and 2.5 cm^{-1}, respectively.

The compressive properties were analyzed using KESFB3-AUTO-A Automatic compression tester (Kato Tech Co., LTD, Kyoto, Japan) under the standard condition. The compression velocity and area were 0.02 mm·s^{-1} and 2 cm^2, respectively, and the maximum compression load was 50 gf·cm^{-2}.

6.3 Results and discussion

6.3.1 rPET/ADR4468 3D-printed textiles

Fig. 6.3 shows rPET/ADR4468 3D-printed textiles samples with different infill densities, rotation angles, and intersection angles. These textiles were 3D-printed according to their structural design to investigate the different effects of structures on their mechanical properties, including infill density 30% (ID30), 50% (ID50), and

70% (ID70); rotation angle, 0° (RA0), 15° (RA15), 30° (RA30), and 45° (RA45); and intersection angle 30° (IA30), 60° (IA60), and 90° (IA90). The lines were extruded through the nozzle and adhered to the lower layer. The rough lines on textiles indicated that rPET/ADR4468-1.0 wt% melt had a low flowability at a printing speed of 30 mm/s, and the polyester filament had moderate quality to form many knots on the lines. The knots had a rough surface of lines and formed random knot patterns. The knots were small and did not affect the nearby lines, which impacted the mechanical properties of textile structures. These knots might be generated by the unstable melt flow with voids in polyester filaments. The sudden increase in melt flow through the nozzle increased the width of printed lines. At the first line, no printing defect was observed from the corner of the textiles after the melt was transferred through the nozzle, which suggested that the melt stored low elastic energy with low hysteresis.

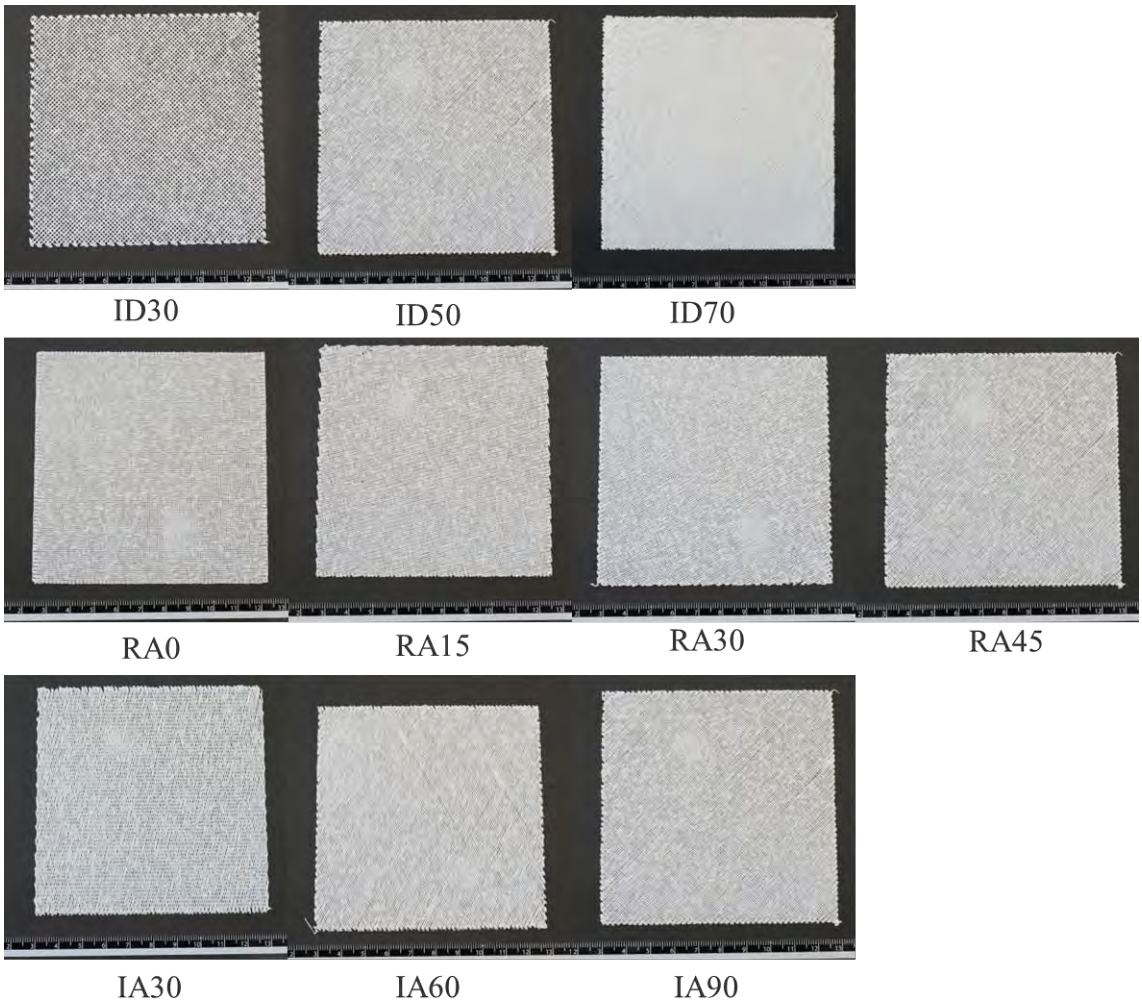

Figure 6.3. rPET/ADR4468 3D-printed textiles

6.3.2 Infill density effect on rPET/ADR4468 textiles

6.3.2.1 Tensile properties

To evaluate infill density effects on tensile properties of rPET/ADR4468 3D-printed textiles, the infill densities were set at 30%, 50%, and 70% (ID30, ID50, and ID70). Fig. 6.4a shows the round curves of the textiles under the uniaxial force. As the infill density decreases, the curves tilted to higher strain with lower slopes and higher tensile extensibility (EMT, Fig. 6.4b). The low slope and high EMT indicate that the textiles can be stretched longer under the maximum load and become more elastic.

The increase in line number in the cross-section could be attributed to the higher elasticity in ID30. Due to the low infill density, fewer lines were printed in ID30. These lines were loaded with more stress and highly deformed when the ID30 was stretched. The textile elasticity increased as the infill density decreased due to the fewer printed lines. As the elasticity of the textile increased, the tensile energy (WT Fig. 6.4c) in ID30 increased because the higher elasticity consumed more energy when the ID30 was stretched. As shown in Fig. 6.4d, the tensile resilience (RT) values of rPET/ADR4468 textiles were similar and close to 80%, which might be attributed to the elastic characteristics of rPET/ADR4468 materials. The textiles exhibited similar tensile properties in the warp and weft directions, which could be attributed to the symmetry of the textile structure. The symmetrical structures allowed the printed lines to deform similarly under the same loadings in two directions. Thus, ID30, ID50, and ID70 had similar load-strain curves, EMT, RT, and WT in two directions. These results showed that the decrease in infill density reduced the modulus and improved the elasticity of the rPET/ADR4468 3D-printed textile, and it did not affect the direction change in warp and weft.

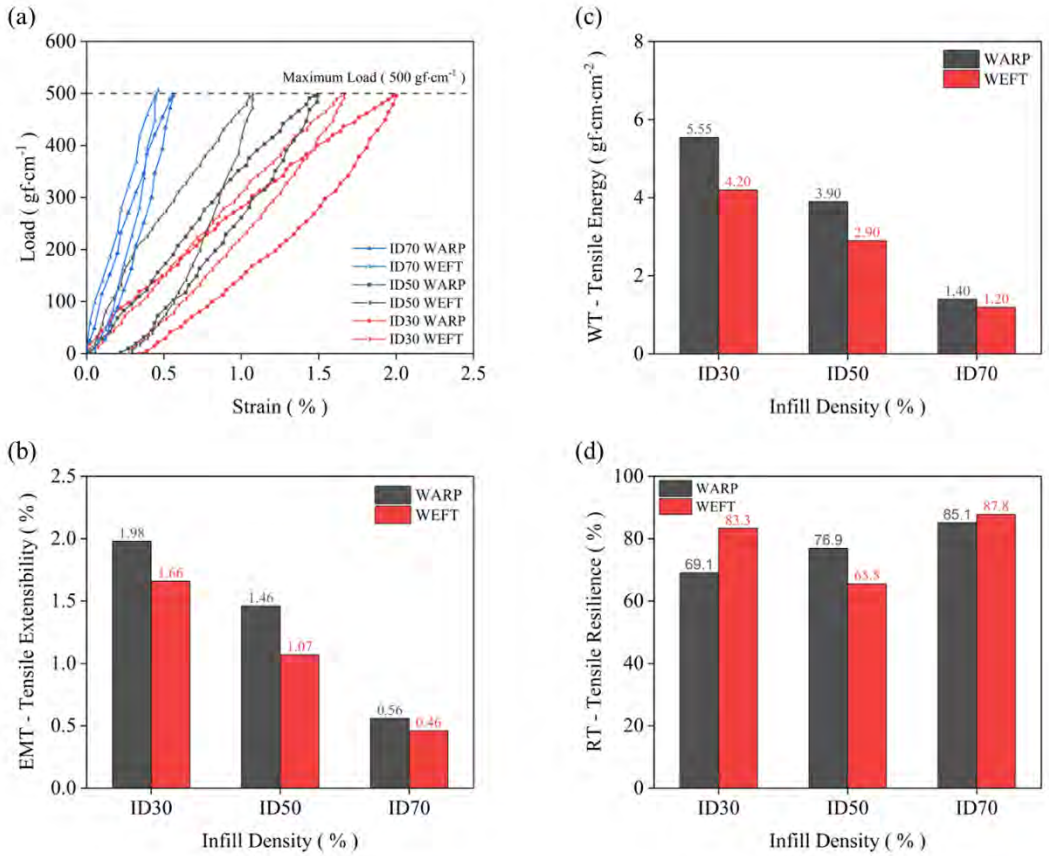

Figure 6.4. Tensile properties of ID30, ID50, and ID70 in warp and weft directions: (a) load-strain curves, (b) EMT, tensile extensibility, (c) WT, tensile energy, and (d) RT, tensile resilience.

6.3.2.2 Shear properties

To evaluate infill density effects on shear properties of rPET/ADR4468 3D-printed textiles, the infill densities of the textiles were set at 30%, 50%, and 70% (ID30, ID50, and ID70). Fig. 6.5a shows the round curves of the textiles under shear stress. As the infill density increased, the curves rose to higher stress and lower shear angle with higher shear rigidity (G, Fig. 6.5b). The high G indicates that the textiles are hard to be sheared and become more rigid with the increase in infill density. The increase in adhered and netted lines was attributable to the higher rigidity in ID70.

Due to the high infill density, more lines were printed in ID70. The netted lines were loaded with more stress in the shear direction at the same deformation. The slope of the load-shear angle curve and G increased as the infill density increased. Moreover, the out-plane deformation of textiles caused the yielding in ID30 and ID50 close to -0.5º. A bulge was formed at the top left corner when the textile started to yield for resisting high shear deformation, which reduced the slope of shearing stress at the high shear angle. Due to the yielding and high rigidity, the asymmetry of -45º and 45º netted lines in two layers was amplified and then formed the wide tail of ID30 and ID50 to greatly increase 2HG in the minus shear angle area. When the infill density increased to ID70, the shear loads of the textile became maximum at low shear angles without yielding, and its 2HG decreased due to the low strain of lines for resilience. The ID70 had a fine round curve and exhibited high rigidity to resist the shear. The ID50 and ID70 exhibited similar shear properties in the warp and weft directions, which could be attributed to the symmetry of the textile structure. The symmetrical structures allowed the printed lines to deform similarly under the same shear stress in two directions. However, ID30 exhibited different properties in two directions. The lower rigidity of ID30 further amplified the asymmetry of two layers, which allowed yielding to appear at the lower shear angle in weft, causing the different curves. The 2HG was much higher in weft than warp. Thus, the ID50 and ID70 had similar load-shear angle curves (G and 2HG) in two directions, but they were different in the two directions of ID30. The results show that the increase in infill density increased the shear rigidity of the rPET/ADR4468 3D-printed textile, and moderate rigidity

amplified the asymmetry of two layers of ID30 to exhibit different shear properties in warp and weft.

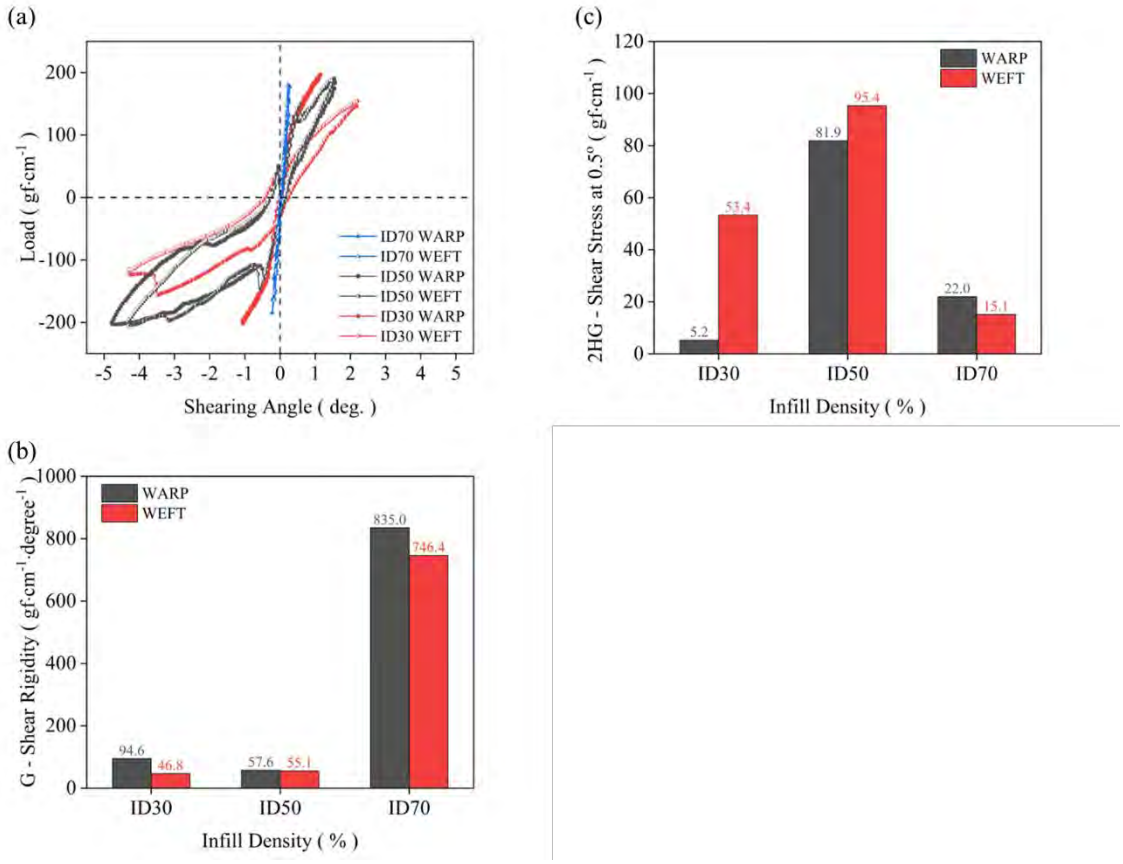

Figure 6.5. Shear properties of ID30, ID50, and ID70 in warp and weft directions: (a) load-shear angle curves; (b) G, shear rigidity; (c) 2HG, shear stress at 0.5º.

6.3.2.3 Bending properties

To evaluate infill density effects on bending properties of rPET/ADR4468 3D-printed textiles, the infill densities of the textiles were set at 30%, 50%, and 70% (ID30, ID50, and ID70). Fig. 6.6a shows the round curves of the textiles under the moment of force. As the infill density decreased, the curves tilted to higher K with lower slopes and B (bending rigidity, Fig. 6.6b). The low slope and bending rigidity indicate that the textiles can be easily bent under low moments of force and become

more flexible. The reduction in the number of lines in the cross-section could be attributed to the higher flexibility in ID30. Due to the low infill density, fewer lines were printed in ID30. These lines resisted less stress to be bent in the same K. The textile flexibility increased as the infill density decreased due to the fewer printed lines. Meanwhile, the increasing flexibility increased the 2HB (bending moment at 0.5 cm^{-1}, Fig. 6.6c) in warp and decreased the 2HB in weft. The difference indicated that the asymmetry of -45º and 45º netted lines in two layers impacted the bending resilience in warp and weft. Due to the high rigidity of rPET/ADR4468 textiles, the asymmetry of the textiles might induce high stress and strain in the other direction under the bending. Thus, the decrease in infill density increased the flexibility of rPET/ADR4468 3D-printed textile due to the decrease in printed lines, and high rigidity amplified the asymmetry of two layers of ID70 to exhibit different shear properties in warp and weft.

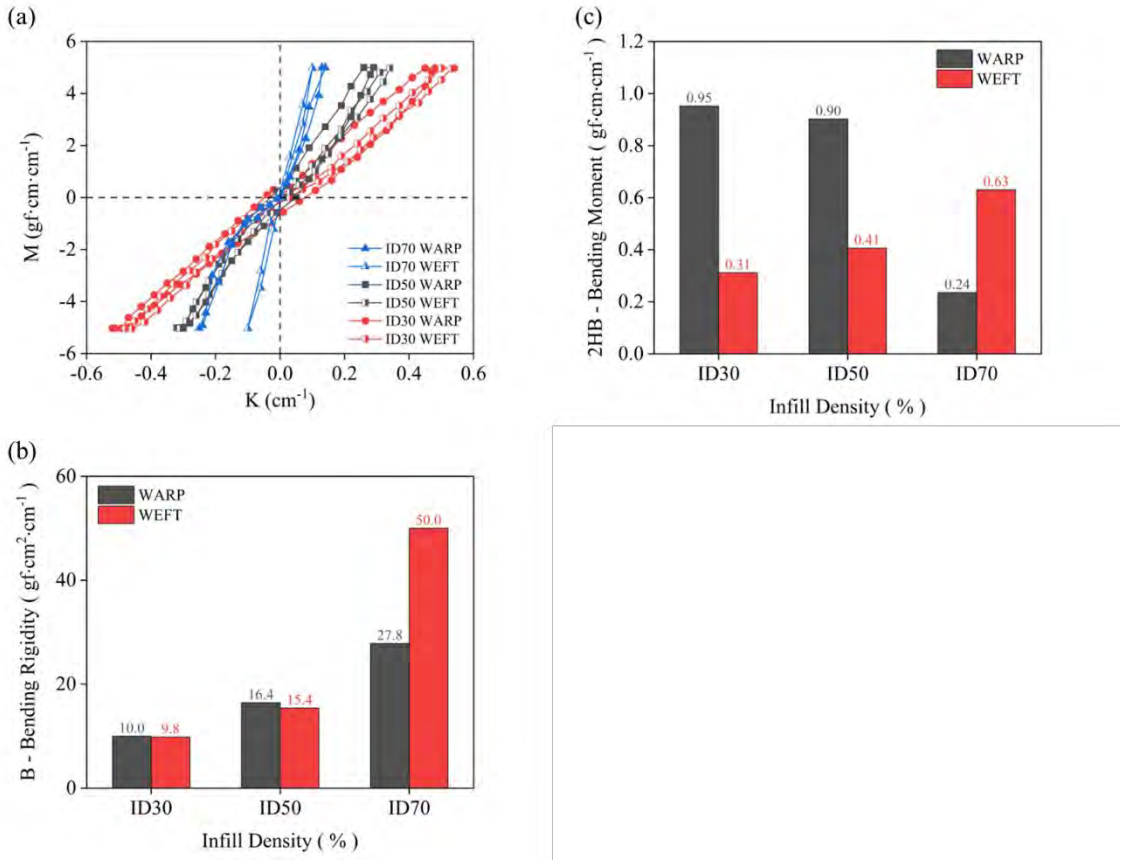

Figure 6.6. Bending properties of ID30, ID50, and ID70 in warp and weft directions: (a) M-K curves; (b) B, bending rigidity; (c) 2HB, the bending moment at half of the maximum K.

6.3.2.4 Compressive properties

To evaluate infill density effects on the compressive properties of rPET/ADR4468 3D-printed textiles, the infill densities were set at 30%, 50%, and 70% (ID30, ID50, and ID70). Compressional linearity (LC, Fig. 6.7a) slightly decreased from ID30 to ID70, indicating that the compressibility of textiles decreased with the increase in infill density because the increase in lines reduced the strain under the same compressive load. Compressional energy (WC, Fig. 6.7b) initially reduced in ID50 and then increased in ID70. The increase in knots increased the strain at low

stress, which increased the WC and further decreased the LC. As shown in Fig. 6.7c, the RC of textiles slightly increased with slight deviation, which could be attributed to less strain on increasing lines for the compressional resilience. Fabric thickness (T_0) at 0.5 gf·cm^{-2}) of textiles was almost close to 0.90 mm with slight deviation, indicating that textiles had high 3D printing quality with similar thickness in the three testing points. The slight increase in T_0 in ID70 might be attributed to the low line distance, which increased the knot height and slightly increased the line height. The results revealed that the decrease in infill density slightly increased the compressibility of the textile due to the decrease in printed lines, and the slight deviation of T_0 demonstrated the high 3D printing quality of rPET/ADR4468 textiles.

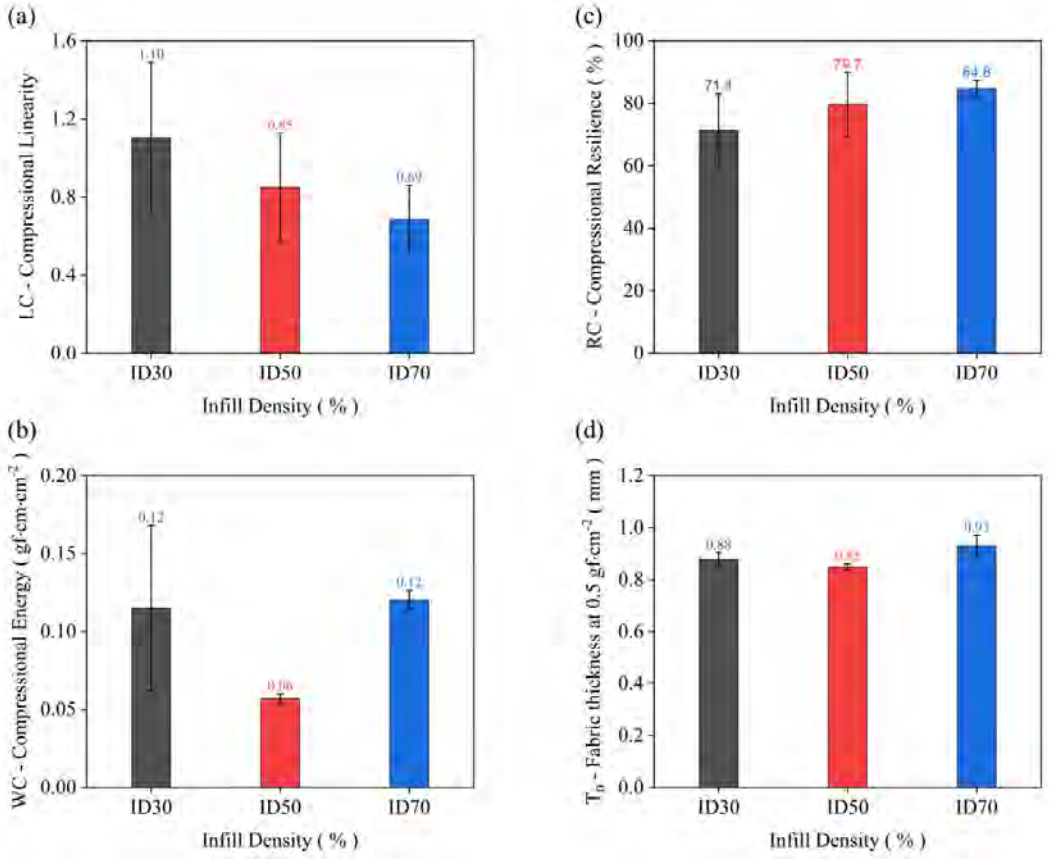

Figure 6.7. Compressive properties of ID30, ID50, and ID70: (a) LC, compression linearity; (b) WC, compressional energy; (c) RC, compressional resilience; (d) T_0,

Fabric thickness at 0.5 gf·cm^{-2}.

6.3.3 Rotation angle effect on rPET/ADR4468 textiles

6.3.3.1 Tensile properties

To evaluate rotation angle effects on the tensile properties of rPET/ADR4468 3D-printed textiles, the rotation angles of the textiles were at 0º, 15º, 30º, and 45º (RA0, RA15, RA30, and RA45). Fig. 6.8a shows the round curves of the textiles under the uniaxial force. As the rotation decreased, the curves tilted to higher strain with lower slopes and higher tensile extensibility (EMT, Fig. 6.8b). The low slope and high EMT indicate that the textiles can be stretched longer under the maximum load and become more elastic. The deformation of minimum repeat square units could be attributed to the increasing elasticity. The units were formed by four printed lines from two layers. As the square units rotated, the tensile stress switched from stretching lines in the tensile direction to deforming the square unit. The units extended in the tensile direction shrank in the vertical direction and rotated to a higher angle. The structure deformation increased the strain in the tensile direction with less strain of lines. However, the lack of unit rotation reduced the tensile strain to deduce the elasticity in RA45. In addition, as the deformation of units increased, the WT (Fig. 7.8c) increased because the deformation of units consumed more energy to reach the same maximum loads. As shown in Fig. 7.8d, the RT of rPET/ADR4468 textiles decreased to approximately 45% in RA30 and returned to 70%. This phenomenon might be attributed to the high strains in RA30, rapidly releasing the internal stress for

rPET/ADR4468. The RA0 exhibited similar tensile properties in the warp and weft directions due to the symmetry of the textile structure. The symmetrical structures in two directions allowed the printed lines and square units to deform similarly under the same loadings in two directions. However, RA15, RA30, and RA45 exhibited different properties in two directions. The high rigidity amplified the asymmetry of two layers and allowed the rotation deformation of units in warp, causing the different curves. The EMT and WT were much higher in warp than in weft. Thus, the RA0 had a similar load-strain curves, EMT, RT, and WT in the two directions, but the curves, EMT, and WT were different in the two directions of RA15, RA30, and RA45. These results revealed that the increasing rotation angle reduced the modulus and improved the elasticity of the rPET/ADR4468 3D-printed textile, and high rigidity amplified the asymmetry of the repeat unit for rotation deformation to perform different tensile properties in warp and weft.

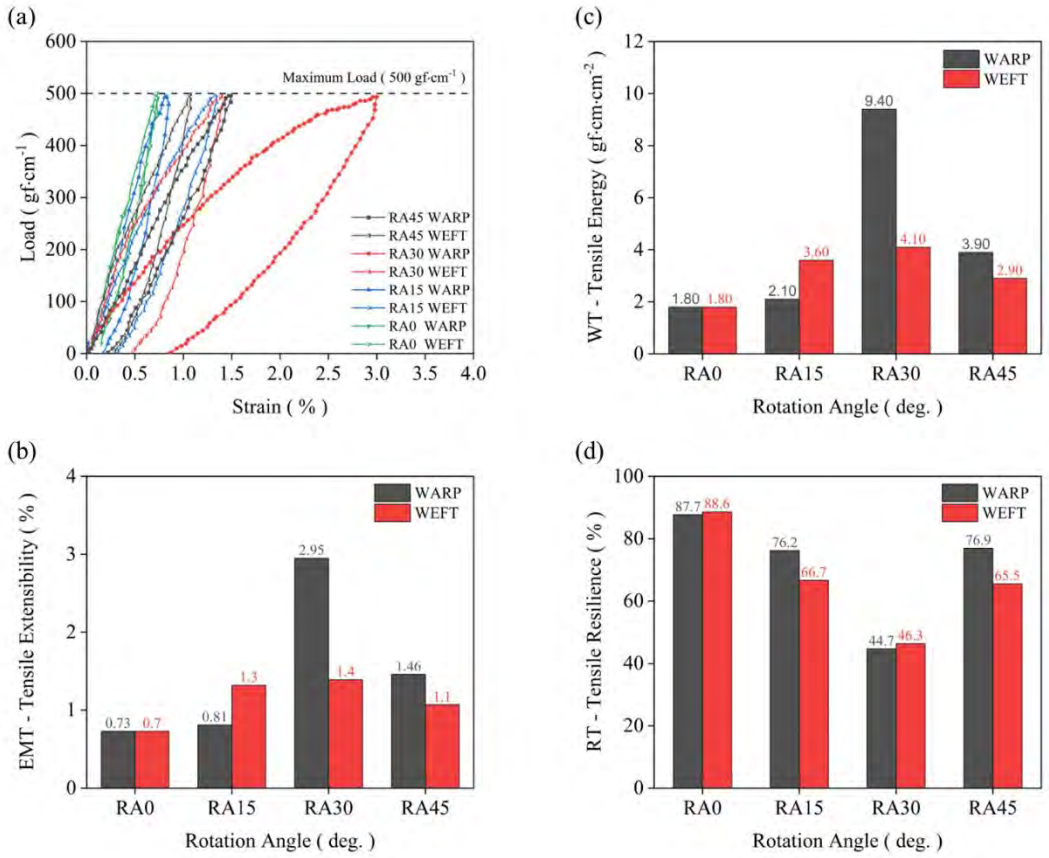

Figure 6.8. Tensile properties of RA0, RA15, RA30, and RA45 in warp and weft directions: (a) load-strain curves, (b) EMT, tensile extensibility, (c) WT, tensile resilience, and (d) RT, tensile energy.

6.3.3.2 Shear properties

To evaluate rotation angle effects on shear properties of rPET/ADR4468 3D-printed textiles, the rotation angles of the textiles were set at 0º, 15º, 30º, and 45º (RA0, RA15, RA30, and RA45). Fig. 6.9a shows the round curves of the textiles under shear stress. As the rotation angle increased, the curves turned to a lower shear angle with higher G (Fig. 6.9b). The high G indicates that the textiles are hard to be sheared and become more rigid as the rotation angle increases. The increasing deformation of the square units could be attributed to the higher rigidity in RA30. In

RA30, the units were rotated to a higher angle, which might reduce the rotation deformation and increase the tensile deformation in the diagonal direction. The tensile deformation of the units in the diagonal direction had more stress than rotation deformation at the same shear angle. To fulfill the shear deformation, the shear load increased to generate more stress for the tensile deformation of the units of RA30 at the same shear angle to increase its shear rigidity. In addition, the increase in rigidity increased the 2HG at 0.5º (Fig. 6.9c) in RA30 because the higher rigidity could resist more shear stress for more strain to resile at the same shear angle. Moreover, the out-plane deformation of textiles caused the yielding in textiles close to -0.5º. A bulge was formed at the top left corner when the textile started to yield for resisting high shear deformation, which reduced the slope of shearing stress at the high shear angle. Due to the yielding and high rigidity of textiles, the asymmetry of -45º and 45º netted lines in two layers was amplified and formed the wide tail of textiles to significantly increase 2HG in the minus shear angle area. However, in RA45, the G and 2HG decreased and increased respectively, which might be attributed to the yielding at 0.5º, thus reducing the G in plus shear area. The RA30 and RA45 exhibited similar shear properties in the warp and weft directions, which could be attributed to the symmetry of the textile structure. The symmetrical structures allowed the printed lines to deform similarly under the same shear stress in two directions. However, RA0 and RA15 exhibited different properties in two directions. The moderate rigidity further amplified the asymmetry of two layers and allowed yielding to appear at a lower shear angle in warp, generating the different curves. The G was much higher in weft than in

warp. These results show that the increasing rotation angle to 30º rigidized the rPET/ADR4468 3D-printed textile under shearing, and moderate rigidity amplified the asymmetry of two layers of RA0 and RA15 to exhibit different shear properties in warp and weft.

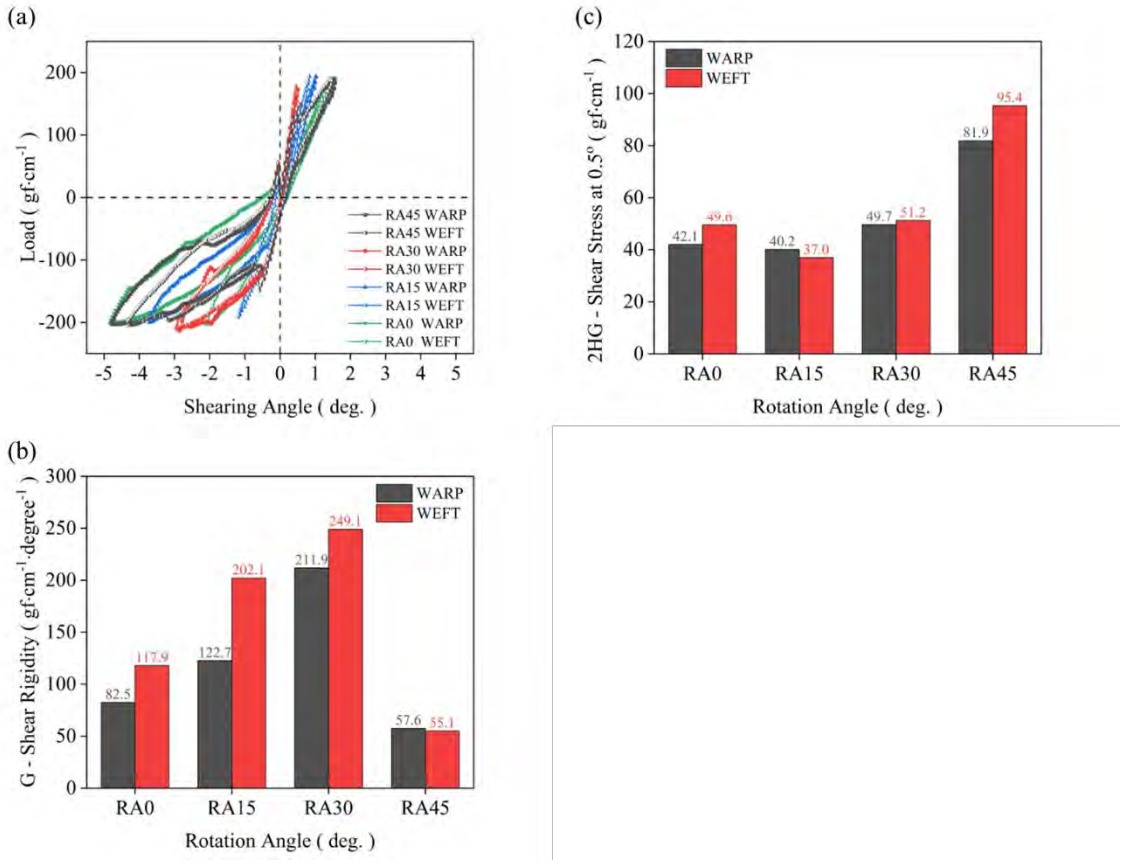

Figure 6.9. Shear properties of RA0, RA15, RA30, and RA45 in warp and weft directions: (a) load-shear angle curves; (b) G, shear rigidity; (c) 2HG, shear stress at 0.5º; (d) 2HG5, shear stress at 5º.

6.3.3.3 Bending properties

The rotation angles of the textiles were set at 0º, 15º, 30º, and 45º (RA0, RA15, RA30, and RA45) to evaluate rotation angle effects on bending properties of rPET/ADR4468 3D-printed textiles. Fig. 6.10a shows the round curves of the textiles

under the moment of force. The curves of bending rigidity (B) of textiles were almost the same in warp and weft directions (Fig. 6.10b), which could be attributed to the high rigidity of rPET/ADR4468 materials. The high rigidity of rPET/ADR4468 decreased the strain of textiles and reduced the effect of rotation angles on textiles under low moments of force. In addition, the less strain on lines for resiling kept the bending moment (2HB) at 0.5 cm^{-1} (Fig. 6.10c) low. The RA0 exhibited similar tensile properties in the warp and weft directions, which could be attributed to the symmetry of the textile structure. The symmetrical structures allowed the printed lines to deform similarly under the same loadings in two directions. Thus, the RA0 had similar M-K curves, B, and 2HB in warp and weft directions. However, RA15, RA30, and RA45 had different 2HB in two directions. The different 2HB in the warp and weft directions indicated that the amplified asymmetry of two layers might induce the moment to increase strains in the other direction, which could not be recorded in the K. These strains might reduce the maximum K, increase the 2HB, limit the further improvement of flexibility of RA30 and RA45, and cause the 2HB of RA15, RA30, and RA45 different in warp and weft. These results revealed that as the rotation angle increased to 15º, the flexibility of RA15 increased, and the strains in other directions reduced the maximum K and increased 2HB, restricting the further flexibility enhancement of RA30 and RA45.

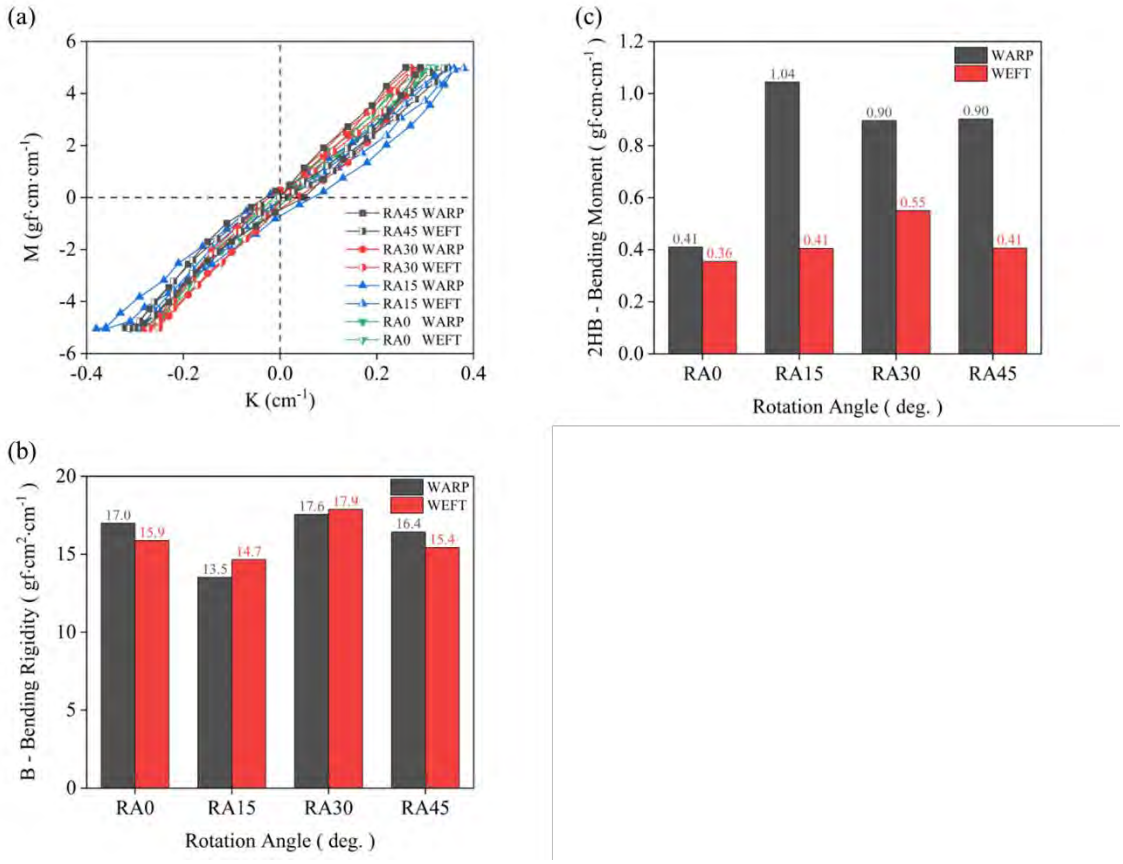

Figure 6.10. Bending properties of RA0, RA15, RA30, and RA45 in warp and weft directions: (a) M-K curves; (b) B, bending rigidity; (c) 2HB, the bending moment at the half of maximum K.

6.3.3.4 Compressive properties

The rotation angles of the textiles were set at 0º, 15º, 30º, and 45º (RA0, RA15, RA30, and RA45) to evaluate rotation angle effects on compressive properties of rPET/ADR4468 3D-printed textiles. Because the testing area of clamps is a circle, compression testing has no directionality, meaning the rotation of structures in the textile plane makes no difference in compression tests. LC (Fig. 6.11a), WC (Fig. 6.11b), RC (Fig. 66.11c), and T_0 at 0.5 gf·cm^{-2} (Fig. 6.11d) were almost the same in textiles with different rotation angles. Moreover, the textiles were 3D-printed with

high quality to have a low deviation in T_0 due to the high quality of rPET/ADR4468-1.0 wt% filaments. The results showed that the rotation angle had no effects on the compressibility of the textile, and the low deviation of T_0 demonstrated the high 3D printing quality of rPET/ADR4468 textiles.

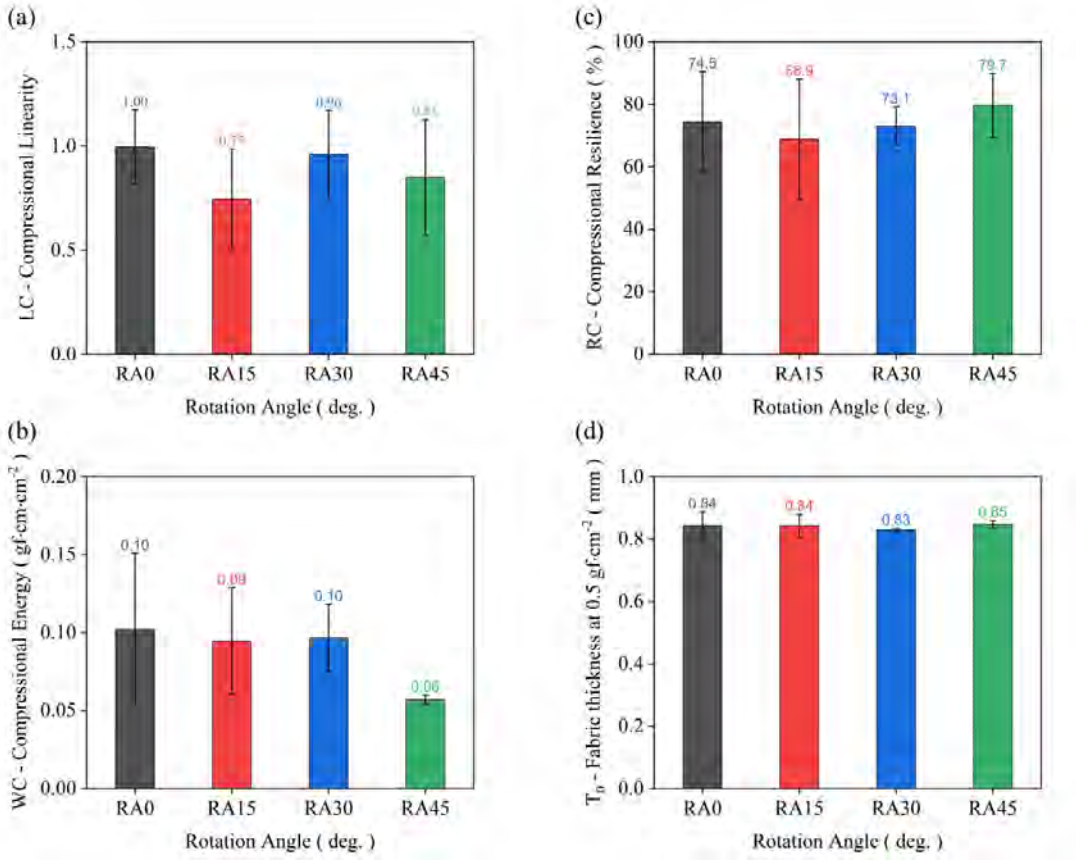

Figure 6.11. Compressive properties of RA0, RA15, RA30, and RA45: (a) LC, compression linearity; (b) WC, compressional energy; (c) RC, compressional resilience; (d) T_0, Fabric thickness at 0.5 gf·cm^{-2}.

6.3.4 Intersection angle effect on rPET/ADR4468 textiles

6.3.4.1 Tensile properties

The intersection angles of the textiles were set at 30º, 60º, and 90º (IA30, IA60, and IA90) to evaluate intersection angle effects on tensile properties of

rPET/ADR4468 3D-printed textiles. Fig. 6.12a shows the round curves of the textiles under the uniaxial force. As the intersection angle decreased, the curves tilted to higher strain with lower slopes and higher EMT (Fig. 6.12b) in the weft direction. The low slope and high EMT indicate that the textiles can be stretched longer under the maximum load and become more elastic. In addition, the increase in elasticity increased the WT (Fig. 6.12c) in IA30 in the weft direction because the higher elasticity consumed more energy in the tension zone. However, the elasticity of textiles significantly decreased in the warp with high slope and low EMT. The different tensile performances in two directions indicated that the increasing intersection angle led to tensile anisotropy in textiles. Repeat unit deformation might explain the anisotropy. As the intersection angle decreased, the units changed from square to rhombus with a shorter diagonal in the weft direction and a longer diagonal in the warp direction. The short diagonal significantly elongated with small strain for line rotation at the smaller angles of the units. In IA30, this tensile deformation of the unit increased the EMT in the shorter diagonal direction (weft) and decreased the EMT in the longer diagonal direction (warp). However, this deformation accelerated the increase in strain at the intersection angle with high strain and low stress of unit deformation. The acceleration made the rPET/ADR4468 3D-printed textiles attain the maximum strain and break at the intersection angle, causing fractures in IA30 in weft direction tension. Due to the fractures, the RT (Fig. 6.12d) of IA30 in the weft direction was zero. In warp, the RT increased over 80%, which might be attributed to the less strain under tension for rPET/ADR4468 resilience. The results showed that

the decreasing intersection angle enhanced the elasticity of the rPET/ADR4468 3D-printed textiles with low tensile strength in weft and reduced the elasticity in warp, forming the anisotropy in the tensile properties of textiles.

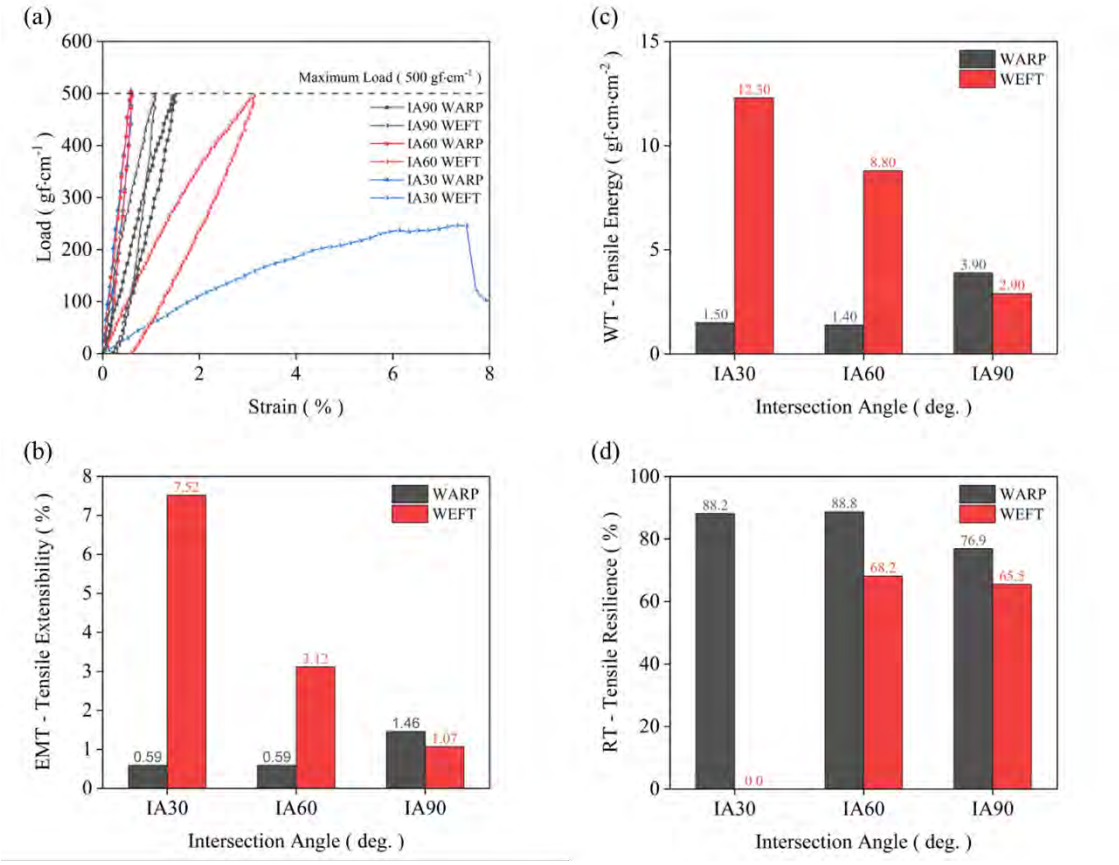

Figure 6.12. Tensile properties of IA30, IA60, and IA90 in warp and weft directions: (a) load-strain curves, (b) EMT, tensile extensibility, (c) WT, tensile resilience, and (d) RT, tensile energy.

6.3.4.2 Shear properties

The intersection angles of the textiles were set at 30º, 60º, and 90º (IA30, IA60, and IA90) to evaluate intersection angle effects on shear properties of rPET/ADR4468 3D-printed textiles. Fig. 6.13a shows the round curves of the textiles under shear stress. As the intersection angle increased, the load-strain curves rose to a

higher load and lower shear angle with higher G (Fig. 6.13b) in warp. The high G indicates that the textiles are hard to be sheared and become more rigid in warp direction with the increase in intersection angle. The increasing deformation of the rhombus units could be attributed to the higher rigidity of IA30 in the warp direction. The long-diagonal distance was held in the vertical direction of the shear. The long diagonal was stretched longer with less tensile deformation of units and more tensile strain of lines at the same shear angle. The more strain of lines increased the shear at the same shear angle to increase the shear rigidity of IA30 in warp. However, the shear rigidity of IA30 decreased in the weft direction. The different shear performances in two directions indicated that the decreasing intersection angle could lead to the anisotropy of the shear properties of textiles. Repeat unit deformation might be attributed to the anisotropy. The short diagonal significantly elongated with a small strain of line rotation at the smaller angles of the units. The IA30 had more tensile deformation of the unit with a less tensile strain of lines at the same shear in the weft direction.

Moreover, the out-plane deformation of textiles caused the yielding in two directions of IA60 and IA90 close to -0.5º. A bulge was formed at the top left corner when the textile started to yield for resisting high shear deformation, which reduced the slope of shearing stress at the high shear angle. Due to the yielding and moderate rigidity of the textiles, the asymmetry of -45º and 45º netted lines in two layers was amplified and formed the wide tail of IA60 and IA90, thus greatly increasing 2HG in the minus shear angle area. The IA30 in the warp direction reached the maximum

shear loads at low shear angles without yielding, and its 2HG decreased due to the low strain of lines for resilience. The IA30 had a fine round curve and exhibited high rigidity to resist the shear in warp. This result reveals that the decreasing intersection angle increased the shear rigidity of the rPET/ADR4468 3D-printed textiles in warp and reduced the shear rigidity in weft, forming the anisotropy in the shear properties of textiles.

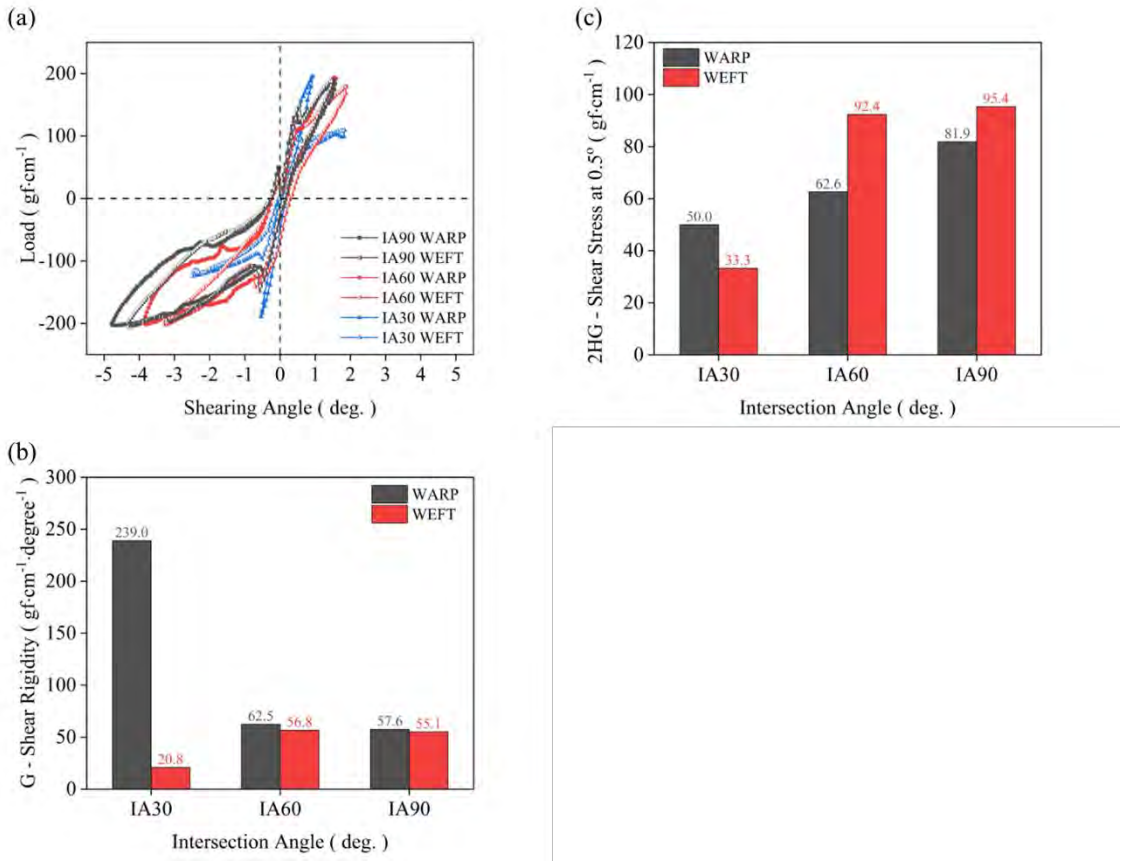

Figure 6.13. Shear properties of IA30, IA60, and IA90 in warp and weft directions: (a) load-Shear angle curves; (b) G, shear rigidity; (c) 2HG, shear stress at 0.5º.

6.3.4.3 Bending properties

The intersection angles of the textiles were set at 30º, 60º, and 90º (IA30, IA60, and IA90) to investigate the effects of intersection angle on bending properties of

rPET/ADR4468 3D-printed textiles. Fig. 6.14a shows the round curves of the textiles under the moment of force. As the intersection angle decreased, the curves significantly tilted to higher K with lower slopes and B (Fig. 6.14b) in the weft direction. The low slope and bending rigidity indicate that the textiles can be easily bent under low moments of force and become more flexible, which might be attributed to the less strain on the lines of the unit out-plane bending at the same curvature. As the intersection angle decreased, the bending deformation was less on lines in the weft direction at the same K, which reduced the line deformation and the strain of rPET/ADR4468. Because the decrease in strain decreased the stress of materials resisting the bending at the same K, IA30 exhibited higher flexibility in the weft direction. On the contrary, the flexibility of IA30 decreased in warp due to the more strain of increasing lines of M, which indicated that the decrease in intersection angle led to the anisotropy of bending properties of textiles. Meanwhile, the increase in flexibility increased the 2HB at 0.5 cm^{-1} (Fig. 6.14c) in the warp direction and decreased the 2HB in the weft direction, indicating a balanced 2HB of IA30 in two directions. The balanced 2HB suggested that the strains of rPET/ADR4468 in warp and weft directions were similar for resilience. The results showed that the decrease in intersection angle enhanced and reduced the flexibility of rPET/ADR4468 3D-printed textiles in weft and warp directions, respectively, forming the anisotropy in the bending properties of textiles.

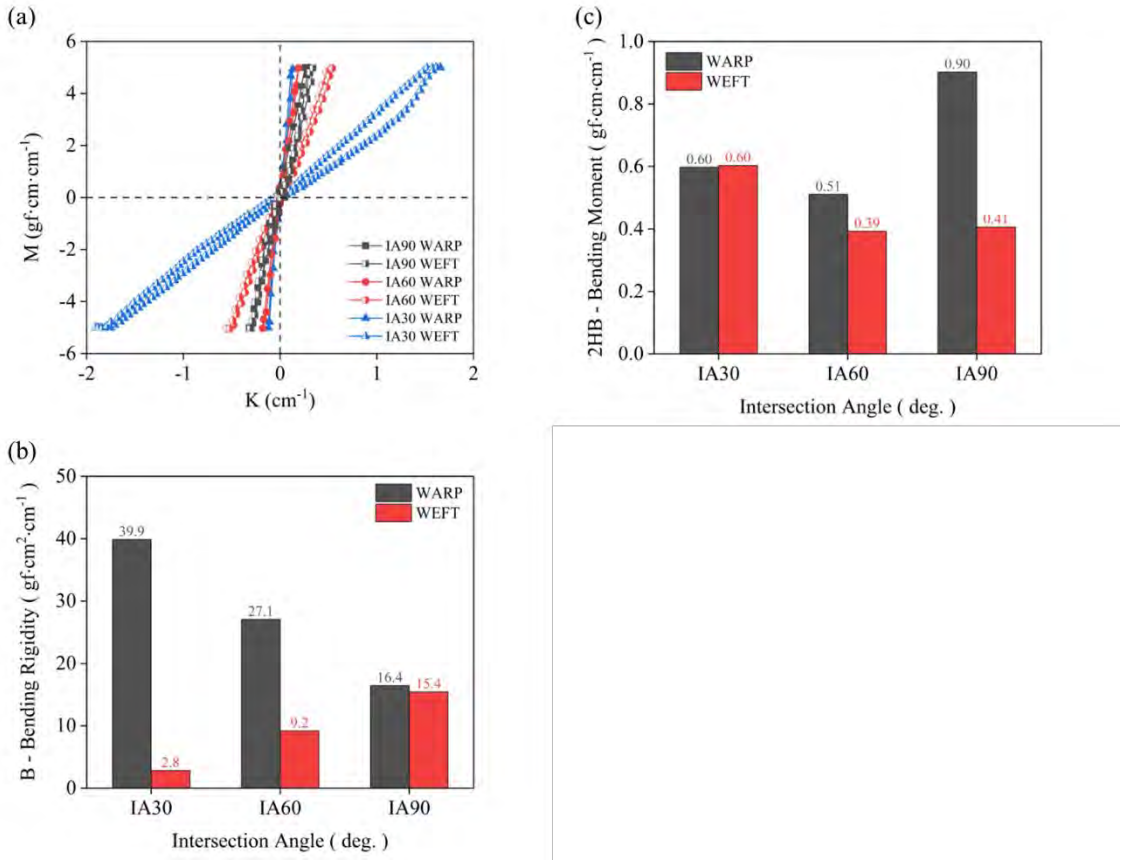

Figure 6.14. Bending properties of IA30, IA60, and IA90 in warp and weft directions: (a) M-K curves; (b) B, bending rigidity; (c) 2HB, bending moment at the half of the maximum K.

6.3.4.4 Compressive properties

The intersection angles of the textiles were set at 30º, 60º, and 90º (IA30, IA60, and IA90) to evaluate intersection angle effects on compressive properties of rPET/ADR4468 3D-printed textiles. LC (Fig. 6.15a) slightly decreased in IA30, which indicated its compressibility decreased. WC (Fig. 6.15b) increased in IA60 and then decreased in IA30. The high WC of IA60 was due to the high strain at low compressive stress. As shown in Fig. 6.15c, the RC of IA30 slightly increased, which could be attributed to less strain on the lines of the compressional resilience. T_0 at 0.5

gf·cm^{-2} of textiles significantly increased in IA60 and slightly increased in IA30. The low deviations indicated high 3D printing quality of IA30 and IA90 with similar thickness in the three testing points. The higher T_0 of IA60 might be attributed to the extrusion swelling at the intersection area, corresponding to the higher strain at low stress and higher WC. The results showed that the decrease in intersection slightly decreased the compressibility, and the low deviation of T_0 indicated the high 3D printing quality of IA30.

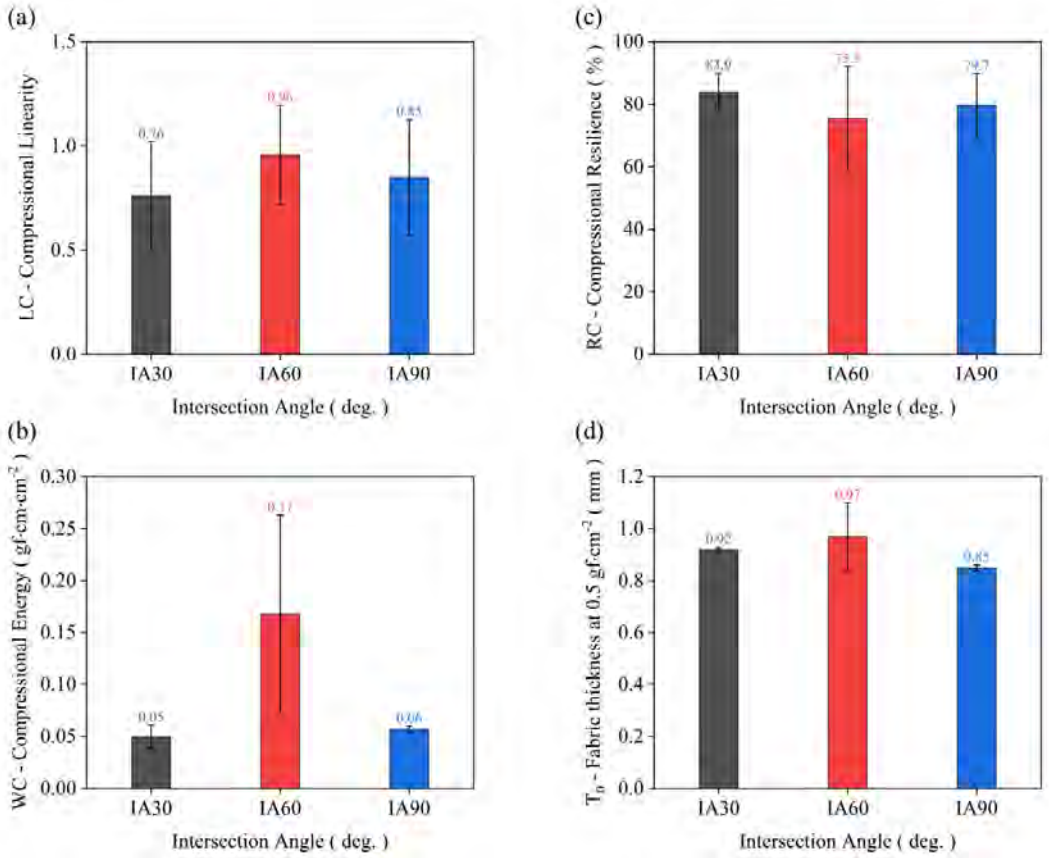

Figure 6.15. Compressive properties of IA30, IA60, and IA90: (a) LC, compression linearity; (b) WC, compressional energy; (c) RC, compressional resilience; (d) T_0, Fabric thickness at 0.5 gf·cm^{-2}.

6.4 Summary

Infill density, rotation angle, and intersection angle affected the flexibility and rigidity of rPET/ADR4468 3D-printed textiles and led to the anisotropy of mechanical properties in warp and weft directions. The low infill density enhanced tensile, shear, bending, and compressive properties due to the fewer lines in the textiles. The fewer lines concentrated the stress, significantly deformed under the same loads, and exhibited higher flexibility of textiles. The 30º and 45º rotation angles increased the flexibility in the tension zone due to the increase in deformation of minimum repeat unit with less strain on lines. Under the same strain, the RA30 and RA45 exhibited the tendency of greater deformation on units and less strain on the lines in the tensile direction, which reduced the stress resistance, resulting in higher flexibility. In shear, the high flexibility of RA45 was attributed to the high yielding with out-of-plane deformation. The low intersection angle greatly enhanced the flexibility in the weft direction and significantly increased the rigidity in the warp direction, resulting in the anisotropy of flexibility textiles in two directions. The anisotropy could be attributed to structural changes in the units. In the weft direction, the diagonal was shortened to increase the number of units with the decreasing intersection angle, indicating that the textile deformation was allocated into smaller deformations for each unit. The smaller deformation reduced the strain of lines and materials to resist lower loading. Because the numbers of lines of IA30, IA60, and IA90 were the same in the testing area, the less strain of each line significantly improved the flexibility of IA30 in the weft direction. The low infill density, rotation angle (30º and 45º), and low intersection

angle enhanced the flexibility of rPET/ADR4468 textiles.

Chapter 7. 3D Printing Flexible Textile Using TPU-Film-Recycled Filaments

This chapter discusses the mechanical performance of rTPU 3D printing flexible textiles. The rTPU filament was utilized to print flexible textiles, according to the designed textile structures. These textile structures were generated programmatically by modifying the infill pattern parameters within the Cura slicer software. To evaluate the mechanical performance and illustrate the connection between the 3D-printed structure and its mechanical properties, this study analyzed the impact of infill densities, rotation angles, and layer numbers on 3D-printed textiles.

7.1 Introduction

The circular economy approach not only involves recycling the TPU film into rTPU filaments but also applies these filaments to manufacture 3D-printed textiles, which form a circular approach for TPU film. To complete the TPU recycling loop, it is imperative to investigate the utilization of the rTPU filament in 3D printing textiles.

3D-printed textiles are created using 3D printing techniques that aim to replicate essential textile properties such as elasticity, flexibility, strength, and porosity[99]. These properties guide the structural design and 3D modeling process, mimicking traditional woven or knitted structures while also fostering the creation of innovative structures based on them[100]. Furthermore, with the development of 3D printing techniques, their heightened resolution, precision, and novel materials empower designers to tackle intricate textile structures on a small scale, exploring the enhancement of essential

textile properties and the potential for functionalization[101-109].

However, the production and development of 3D-printed textiles are hindered by cost and technical prerequisites. Woven and knitted textiles comprise numerous voids and necessitate layer-by-layer printing with supports. To circumvent the need for extensive post-processing of supports, the selective laser sintering (SLS) 3D printing technique has gained traction in producing these types of textiles[110]. However, compared with traditional textiles, the cost associated with SLS remains excessively high for producing 3D-printed textiles with essential structures. Thus, this technique is currently employed for crafting prototypes featuring intricate textile designs.

FDM 3D printing technique offers a plausible solution to the cost-related challenges. The affordability of materials and equipment makes it accessible for individuals to fabricate customized products, such as spectacle frames[17], tools, accessories, garage kits, gears[111], and more. Meanwhile, the economical supply chain associated with FDM has prompted manufacturing facilities to establish FDM 3D printing centers for producing consumer-specified products. Thus, this affordable technique holds the potential to produce 3D-printed textiles with essential structures, supplanting traditional textiles in certain applications as the cost of 3D-printed textiles decreases. Additionally, with open 3D model sources and the evolution of user-friendly slicers, 3D-printed textiles have become a pursuit for hobbyists and tech enthusiasts alike.

The infill pattern generation method can further lower the technical barriers and reduce the expenses associated with 3D-printed textiles. Furthermore, within the Cura

slicer, the infill area can be customized using several parameters, including infill density, infill pattern, and layer numbers. These parameters facilitate the automatic generation of 3D printing patterns via slicer programs applied to thin board models, thus forming the 3D-printed textiles without upper and lower layers. This approach streamlines the processes and minimizes technical hurdles by generating infill patterns, thereby bypassing the necessity for intricate 3D modeling of 3D-printed textiles.

In this study, the textile structure was created programmatically by configuring infill pattern parameters within the 3D printing slicer. After designing the structure, the textiles were 3D-printed using rTPU filaments to finish the circular approach. To investigate the impact of textile structures on mechanical performance, the KES-F system was employed to evaluate the mechanical attributes of textiles featuring different infill densities, rotation angles, and layer numbers.

7.2 Method

7.2.1 Materials

The rTPU filament was produced by The Biofuels Institute, School of the Environment and Safety Engineering, Jiangsu University. The filament was stored at 25℃ and 65% relative humidity for two days before 3D printing.

7.2.2 Textile structure design

Utilizing the Cura 3D printing slicer software (Ultimaker B.V., the Netherlands),

the textile structure was generated programmatically using different infill densities, rotation angles, and intersection angles (Fig. 7.1). Cura managed 3D printing paths and generated patterns on 0.6 mm high solid sheet 3D models. This model height allowed the creation of textile structures through 3D printing using two layers (each with a layer height of 0.3 mm). The default textile structure comprised a 50% infill density, 45° rotation angle, and 90° intersection angle. To evaluate the impact on textile mechanical properties, infill densities were set as 30%, 50%, and 70%. The rotation angles were set as 0°, 15°, 30°, and 45°, achieved by altering the infill line directions to [0, 90], [-15, 75], [-30, 60], and [-45, 45]. The layer numbers were configured as two, three, and four by adjusting the 3D model height to 0.6 mm, 0.9 mm, and 1.2 mm.

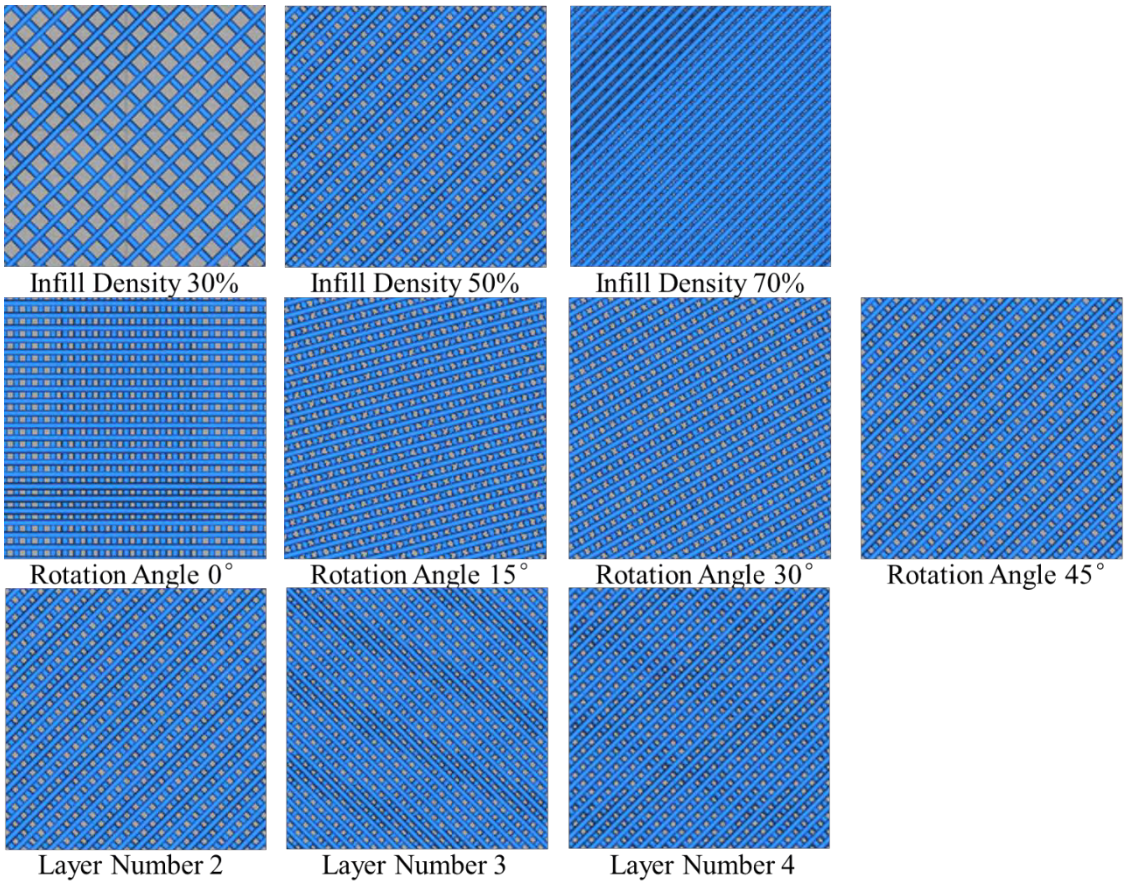

Figure 7.1. Program-generated textile structures of rTPU 3D-printed textile samples.

7.2.3 3D printing using rTPU filament

Fig. 7.2 presents the program-generated structures as patterned textiles that were 3D-printed, 100 mm in length, 100 mm wide, and a height of 0.6 mm. Thin solid sheet models were created using Fusion 360, a 3D modeling software (Autodesk Inc., San Francisco, USA). The Fusion 360 software exported these models as standard tessellation language (STL) files for the Cura slicer to generate patterns within the sheets. Infill patterns were configured according to structure design by adjusting the infill density and infill line directions. To concentrate on the structural effect, the layer number was set at zero, resulting in textiles without outer wall structures. The patterned lines determined the 3D printing or nozzle extrusion path. The slicer software also established material parameters according to the recommended settings for polyester filaments. These parameters directly impact the quality of 3D-printed textiles (Table 7.1). After the parameter setup, the slicer converted the models and printing parameters into geometric code (GCODE) files. The GCODE files planned the printing path along with printing parameters for the filament-based FDM 3D printer (JGMaker-A6, JG AURORA, Shenzhen, China) to fabricate the patterned textiles. After printing, the textiles were cooled down to 25℃ to prevent deformation during removal from the print plate.

Figure 7.2. 3D printing of rTPU textile samples with program-generated patterns.

Table 7.1. 3D printing parameters for rTPU 3D-printed textile samples

3D printing parameter	Value
Layer height	0.3 mm
Wall thickness	0 mm
Top/Bottom thickness	0 mm
Infill pattern	Lines
Printing temperature	180°C
Build plate temperature	60°C
Flow	110%
Printing speed	30 mm/s

7.2.4 Characterization

Mechanical assessments were conducted to investigate the effects of the infill density, rotation angle, and intersection angle on the mechanical properties of the textile structures. The textiles were stored at 20°C and 65% relative humidity over 24 hours to facilitate KES-F testing. The KES-F system evaluated the mechanical properties of

each textile structure in warp and weft directions at 20℃ and 65% relative humidity, including tensile, shear, bending, and compressive properties.

The tensile properties were measured on KESFB1-AUTO-A automatic tensile & shear tester (Kato Tech Co., LTD, Kyoto, Japan) under the optional condition. Sample testing dimensions were 5 cm in length, and 10 cm in width, with a maximum tensile load of 500 $gf \cdot cm^{-1}$, a tensile velocity of 0.2 $mm \cdot s^{-1}$, and a maximum elongation of 25 mm.

Shear properties were evaluated on KESFB1-AUTO-A automatic tensile & shear tester under standard conditions. Sample dimensions remained constant with a length of 5 cm and a width of 10 cm, with a shear tension of 10 $gf \cdot cm^{-1}$ and a maximum shear angle ranging from 8° to -8°.

Bending properties were assessed using the KES-FB2 pure bending tester (Kato Tech Co., LTD, Kyoto, Japan) under standard conditions. Sample dimensions were 1 cm in length and 20 cm in width, with a maximum bending load of 5 $gf \cdot cm \cdot cm^{-1}$ and a maximum curvature of 2.5 cm^{-1}.

Compressive properties were conducted using the KESFB3-AUTO-A Automatic compression tester (Kato Tech Co., LTD, Kyoto, Japan) under standard conditions. Compression was conducted at a velocity of 0.02 $mm \cdot s^{-1}$, over a compression area of 2 cm^2, with a maximum compression load of 50 $gf \cdot cm^{-2}$.

7.3 Results and discussion

7.3.1 rTPU 3D-printed textiles

Fig. 7.3 shows samples of rTPU 3D-printed textiles with different infill densities, rotation angles, and layer numbers. These textiles were 3D-printed according to the structural design to investigate the diverse impacts of different structures on mechanical properties, including infill density 30% (ID30), 50% (ID50), and 70% (ID70); rotation angle, 0° (RA0), 15° (RA15), 30° (RA30), and 45° (RA45); and layer number 2 (LN2), layer number 3 (LN3), and layer number 4 (LN4). Furthermore, within continuous printing areas, the textiles exhibited high-quality printing outcomes. The extruded printing lines followed smoothly from the nozzle and adhered firmly to the underlying layers. The fine lines on the textiles indicated that the printing parameters were optimally adjusted to accommodate the flow characteristics of rTPU melt, with a printing speed of 30 mm/s. Additionally, the rTPU filament maintained consistent high quality, ensuring stable flow rates during filament feeding. A minor printing defect appeared at the first line after the nozzle travel, originating from the corner of the textiles and diminishing toward the end of the line. This defect emerged due to the sudden release of extrusion pressure at the end of the nozzle during nozzle traveling. Given the elasticity of rTPU melt, the sudden release necessitated additional pressure to store elastic energy before commencing the flow. Consequently, a hysteresis effect occurred in conjunction with the designated printing process, causing the flow of rTPU to lag behind the extrusion. The rTPU continued to flow through the nozzle as the nozzle had already moved to the next position, leading

to a material deficiency at the first line after travel. Fortunately, this defect fell outside the testing area of the KES-F system, ensuring its negligible impact on the evaluation.

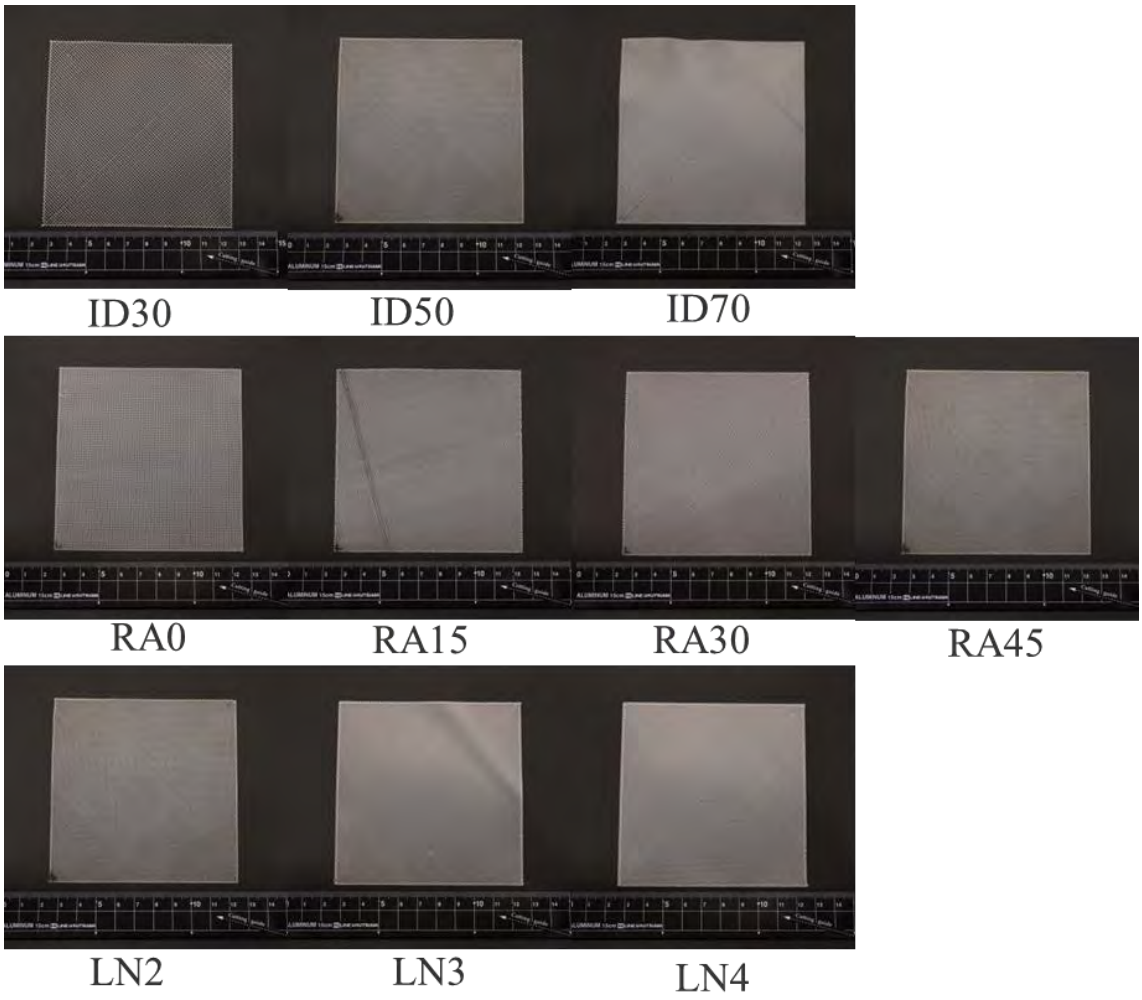

Figure 7.3. rTPU 3D-printed textiles

7.3.2 Infill density effect on rTPU 3D-printed textiles

7.3.2.1 Tensile properties

To evaluate infill density effects on tensile properties of rTPU 3D-printed textiles, the infill densities of the textiles were set to 30%, 50%, and 70% (designated as ID30, ID50, and ID70). Fig. 7.4a illustrates the rounded curves of the textiles subjected to uniaxial force. As the infill density decreased, the curves exhibited a tilt

toward higher strain levels, characterized by lower slopes and greater EMT values (Fig. 7.4b). The reduced slope and increased EMT indicated that the textiles with lower infill densities exhibited greater elongation under maximum loads, displaying enhanced elasticity. The decrease in the number of lines within the cross-section of ID30 elucidates the higher elasticity observed. The lower infill density led to fewer printed lines in ID30, intensifying the stress borne by each line and inducing pronounced deformation during stretching. Consequently, textile elasticity increased with decreasing infill density due to the fewer printed lines. This augmented elasticity, in turn, contributed to heightened tensile energy (WT) during stretching (Fig. 7.4c). The tensile resilience (RT) exhibited a consistent value of ~ 60% across various rTPU textiles, owing to the elastic property of rTPU materials (Fig 7.4d). The rTPU textiles exhibited similar tensile properties in the warp and weft directions, which was attributable to the symmetry of the textile structure. The symmetrical structures ensured comparable deformation of printed lines under identical loads across both directions. Thus, the ID30, ID50, and ID70 exhibited similar load-strain curves, EMT, RT, and WT in both directions. In consideration of these results, decreasing infill density resulted in lowered modulus and enhanced elasticity within rTPU 3D-printed textiles, with no observable effect on directional variation in warp and weft directions.

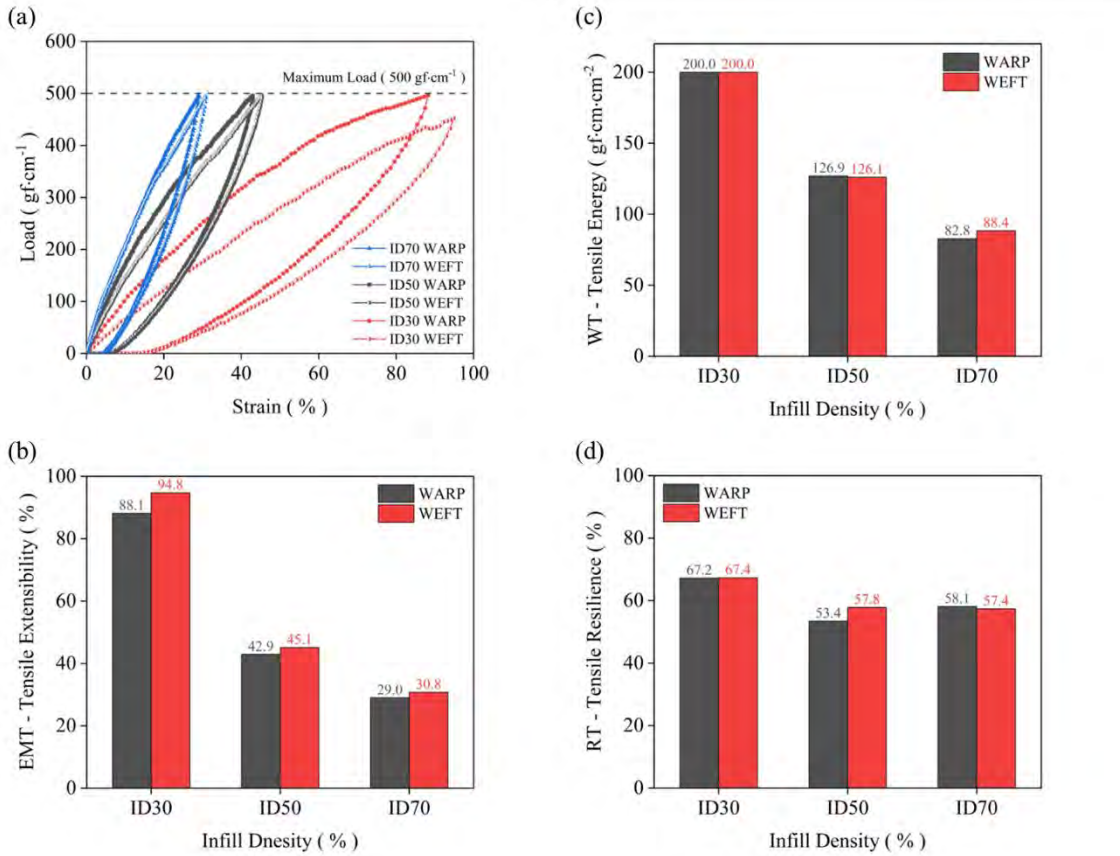

Figure 7.4. Tensile properties of ID30, ID50, and ID70 in warp and weft directions: (a) load-strain curves, (b) EMT, tensile extensibility, (c) WT, tensile energy, and (d) RT, tensile resilience.

7.3.2.2 Shear properties

To evaluate infill density effects on shear properties of rTPU 3D-printed textiles, the infill densities of the textiles were set as 30%, 50%, and 70% (designated ID30, ID50, and ID70). Fig. 7.5a illustrates the round curves of the textiles under shear stress. As the infill density increased, the curves exhibited higher stress levels and increased shear rigidity (G) (Fig. 7.5b). The increased G values indicated that the textiles exhibited increased resistance to shear forces and progressively stiffer with increasing infill density. The increased rigidity in ID70 was attributable to the

presence of more closely netted lines. The ID70 featured a greater number of printed lines, owing to the increased infill density. At the same deformation, these netted lines bore increased stress when subjected to shear forces. Accordingly, both the slope of the load-shear angle curve and the value of G increased as infill density increased. Simultaneously, the augmented rigidity led to an increased shear stress at 0.5° (2HG) and shear stress at 5° (2HG5) values within ID70, respectively (Fig. 7.4c and Fig. 7.4d). This result was attributable to the heightened rigidity, which countered the greater shear stress, accommodating more rTPU strain to resile at the same shear angle. Moreover, the high shear rigidity led to yielding in the ID70, which was attributable to the out-of-plane deformation of the textiles. The yielding phenomenon resulted in the formation of bulges at regular intervals on ID70 textiles when subjected to high shear deformation. Thus, reducing the slope of shearing stress at the high shear angle, and limiting further increase in 2HG5 values. Notably, rTPU textiles exhibited similar shear properties in the warp and weft directions, attributable to the symmetry of the textile structure. The symmetry ensured consistent deformation of printed lines under identical shear stress in both directions. Thus, the ID30, ID50, and ID70 exhibited comparable load-shear angle curves, G values, 2HG, and 2HG5 values in both directions. In conclusion, heightened infill density increased the shear rigidity of the rTPU 3D-printed textile, with no significant effect on directional variation in warp and weft directions.

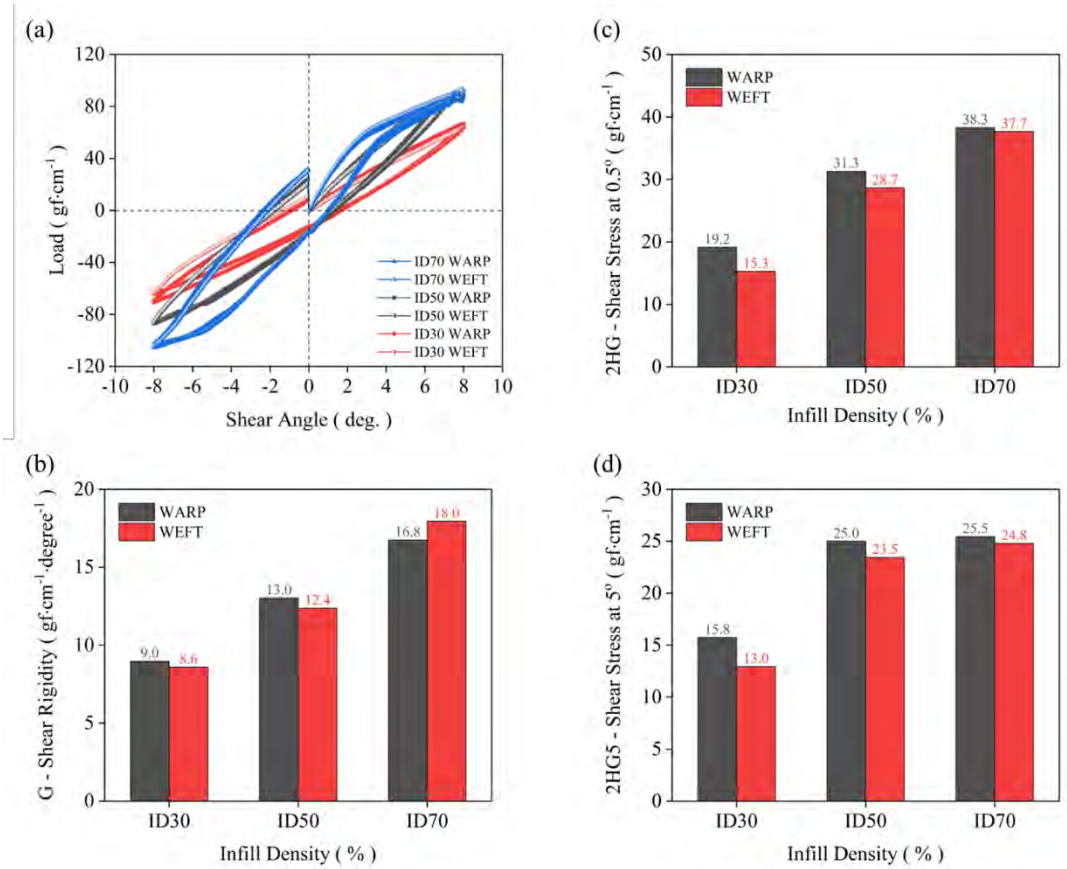

Figure 7.5. Shear properties of ID30, ID50, and ID70 in warp and weft directions: (a) load-Shear angle curves; (b) G, shear rigidity; (c) 2HG, shear stress at 0.5º; (d) 2HG5, shear stress at 5º.

7.3.2.3 Bending properties

To evaluate infill density effects on bending properties of rTPU 3D-printed textiles, the infill densities of the textiles were set to 30%, 50%, and 70% (designated ID30, ID50, and ID70). Fig. 7.6a depicts the curves of the textiles when subjected to a moment of force. As the infill density decreased, the curves exhibited a decline in bending moment (M) with lower slopes, along with reduced bending rigidity (B) values (Fig. 7.6b). The lower slope and bending rigidity suggest that textiles with lower infill density bent easily under lower moments of force, displaying enhanced

flexibility. The reduction in the number of lines within the cross-section of ID30 accounted for the heightened flexibility observed. Furthermore, due to the diminished infill density, ID30 featured fewer printed lines. These lines encountered less stress when subjected to bending under the same curvature (K). Accordingly, textile flexibility increased as infill density decreased, owing to the fewer printed lines. Simultaneously, the augmented flexibility led to a slight decrease in M at 0.5 cm^{-1} (2HB) within ID30 and a more significant reduction in ID50 (Fig. 7.6c). The difference indicated that the rigidity of ID50 was attributable to the high bending resilience of rTPU. As rigidity increased further, rTPU yielded slightly and released internal stress, generating additional strain. This strain could not recover in a short period, causing an increase in 2HB. The rTPU textiles exhibited similar bending properties in the warp and weft directions, which was attributable to the symmetry of the textile structure. This symmetry ensured consistent deformation of printed lines under identical loads across both directions. Consequently, ID30, ID50, and ID70 exhibited similar M–K curves, B, and 2HB values in both directions. Conclusively, the decreased printed lines resulting from lower infill density enhanced textile flexibility and maintained high bending resilience within the rTPU 3D-printed textiles. Thus, exhibiting no observable effect on directional variation in warp and weft directions.

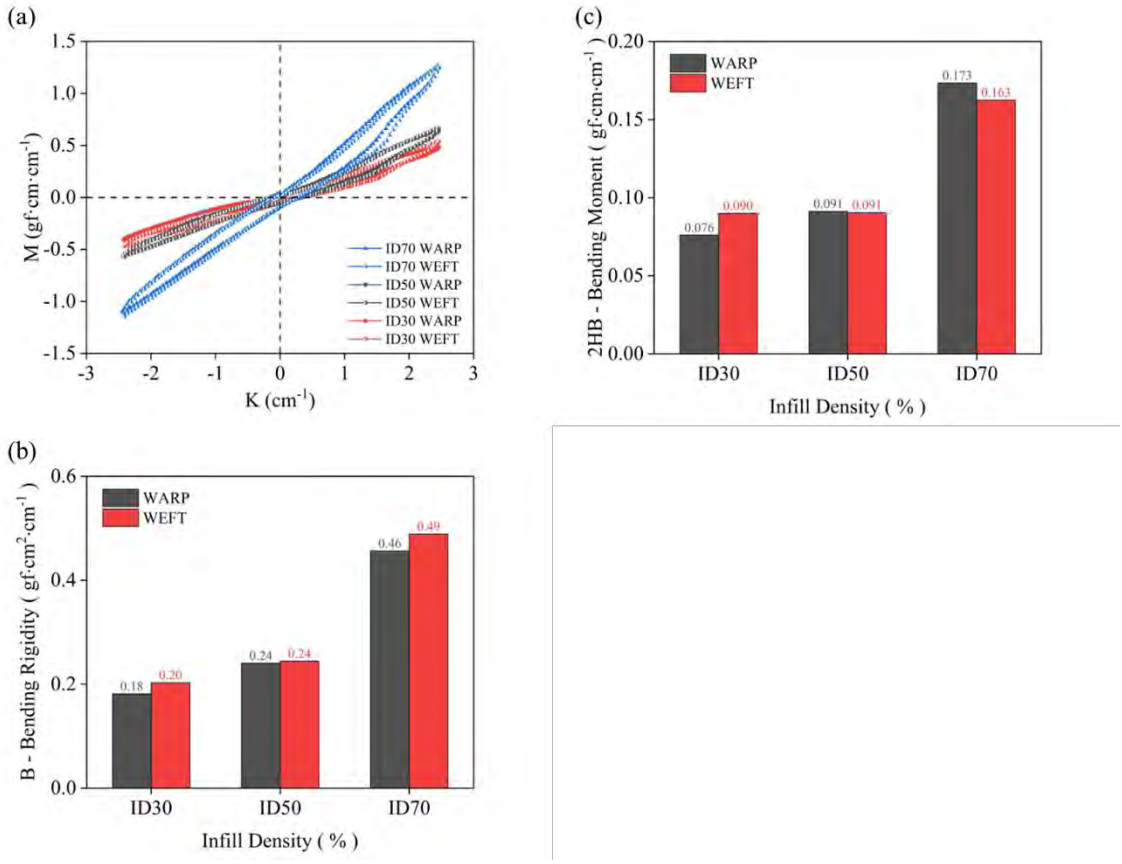

Figure 7.6. Bending properties of ID30, ID50, and ID70 in warp and weft directions: (a) M-K curves; (b) B, bending rigidity; (c) 2HB, bending moment at 0.5 cm^{-1}.

7.3.2.4 Compressive properties

To evaluate infill density effects on compressive properties of rTPU 3D-printed textiles, the infill densities of the textiles were set to 30%, 50%, and 70% (designated ID30, ID50, and ID70). Compressional Linearity (LC) and Compressional Energy (WC) slightly decreased from ID30 to ID70 (Fig. 7.7a and 7.7b) This indicated the compressibility of textiles decreased with increasing infill density due to the augmented number of lines, reducing the strain under the identical compressive load. The compressional resilience of the textiles remained almost consistent with minimal deviation (Fig. 7.7c). This suggests that the infill density did not affect the

compressional resilience related to the compressive properties of rTPU materials. Fabric thickness at 0.5 gf·cm^{-2} (T_0) for ID30 and ID50 was ~ 0.75 mm with low deviation, indicating high 3D printing quality with similar thickness at the three testing points. The slight increase of T_0 in ID70 was attributable to the die swelling of elastic rTPU melts at the end of the nozzle, resulting in a slight increase in the height of the printed line. In summary, the decrease in printed lines due to lower infill density led to a slight increase in textile compressibility, while the low T_0 deviation exhibited the high 3D printing quality of rTPU textiles.

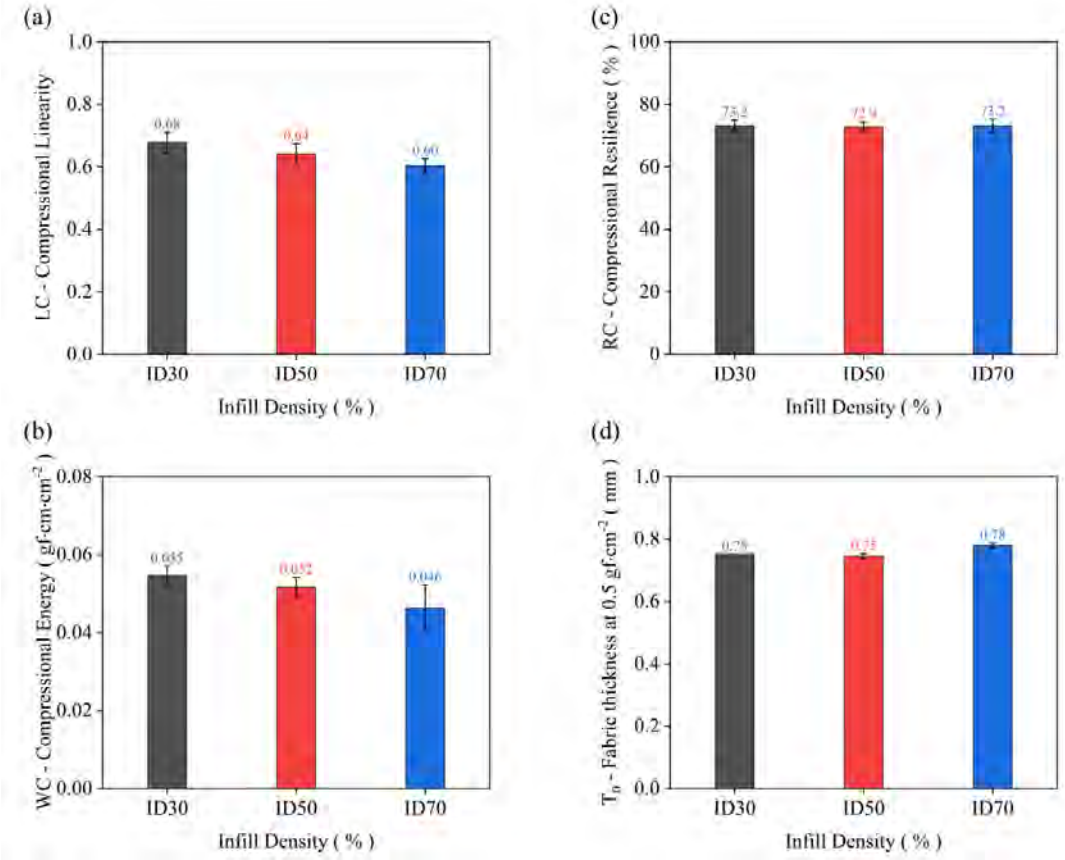

Figure 7.7. Compressive properties of ID30, ID50, and ID70: (a) LC, compression linearity; (b) WC, compressional energy; (c) RC, compressional resilience; (d) T_0, Fabric thickness at 0.5 gf·cm^{-2}.

7.3.3 Rotation angle effect on rTPU textiles

7.3.3.1 Tensile properties

To evaluate rotation angle effects on the tensile properties of rTPU 3D-printed textiles, the rotation angle (RA) of the textiles were set to 0º, 15º, 30º, and 45º (designated RA0, RA15, RA30, and RA45). Fig. 7.8a illustrates the round curves of the textiles under the uniaxial force. As RAs decreased, the curves tilted toward higher strain with lower slopes and increased EMT values (Fig. 7.8b). The lower slope and increased EMT indicated that the textiles exhibited higher elasticity, enabling them to stretch further under maximum load. Increased elasticity in RA45 elucidated the deformation of minimum repeat square units. These units were formed using four printed lines from two layers, and their rotation caused a shift in tensile stress from stretching lines to deforming the square unit. In this configuration, the units extended in the tensile direction and contracted vertically, resulting in higher strain along the tensile direction with lines exhibiting less strain. Simultaneously, enhanced structure deformation led to increased tensile energy (WT) consumption (Fig. 7.8c). The tensile resilience (RT) of rTPU textiles remained consistent near 55%, owing to the elastic characteristics of rTPU materials (Fig. 7.8d). The textiles exhibited similar tensile properties in the warp and weft directions, which was attributable to the symmetry of the textile structure. Symmetrical structures ensured uniform deformation of printed lines and square units under similar loads in both directions. Thus, the RA0, RA15, RA30, and RA45 exhibited similar load-strain curves, EMT, RT, and WT in both directions. Furthermore, increasing RAs reduced

the modulus and improved the elasticity of the rTPU 3D-printed textile. Thus, exhibiting no observable effect on directional variation in warp and weft directions.

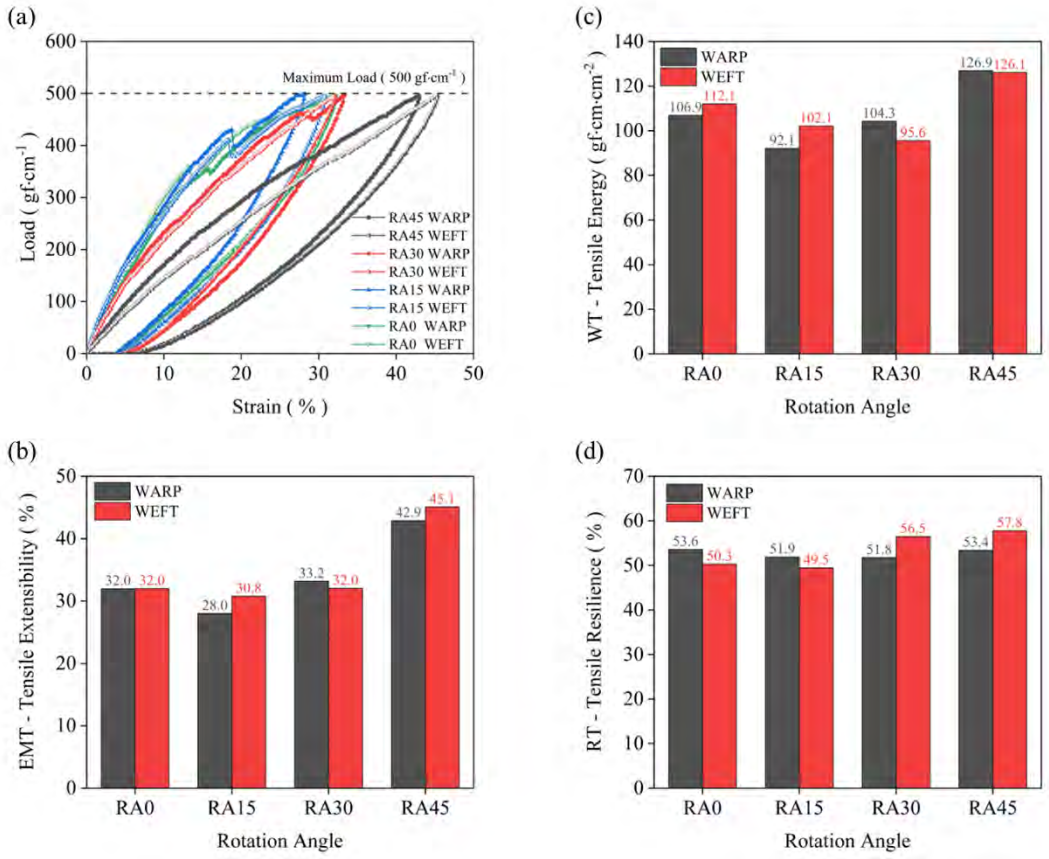

Figure 7.8. Tensile properties of RA0, RA15, RA30, and RA45 in warp and weft directions: (a) load-strain curves, (b) EMT, tensile extensibility, (c) WT, tensile energy, (d) RT, tensile resilience.

7.3.3.2 Shear properties

To evaluate rotation angle effects on shear properties of rTPU 3D-printed textiles, rotation angles of the textiles were set to 0º, 15º, 30º, and 45º (designated RA0, RA15, RA30, and RA45). Fig. 7.9a depicts the round curves of the textiles under shear stress. As the RA increased, the curves ascended to higher stress levels, correlating with increased shear rigidity (G)values (Fig. 7.9b). The heightened G

indicates increased resistance to shearing, rendering textiles more rigid with augmented RAs. The increased deformation of the square units elucidated the higher rigidity in RA45. In this configuration, units were rotated into a square-rhombus position, and one diagonal was aligned vertically to the shear direction. This positioning extended the vertical diagonal, resulting in more deformation than other textiles at the same shear angle. To accommodate this deformation, the shear stress increased to augment the shear rigidity of RA45 at the same shear angle. Simultaneously, the augmented rigidity increased the shear stress (2HG) at 0.5º, and shear stress (2HG5) at 5º in RA45, as higher rigidity resisted more shear stress under identical deformation and shear angles (Fig. 7.4c and Fig. 7.4d). Moreover, the high shear rigidity led to yielding in the RA45 due to the out-plane deformation of textiles. Bulges formed at fixed intervals on the RA45 when the textile yielded for resisting high shear deformation, reducing the slope of shearing stress at the high shear angle. Both warp and weft directions exhibited similar shear properties due to the symmetry of the textile structure, ensuring uniform deformation of printed lines under identical shear stress in both directions. Thus, the RA0, RA15, RA30, and RA45 exhibited similar load-shear angle curves, G, 2HG, and 2HG5 in both directions. In summary, increasing the RA to 45º augmented the rigidity of the rTPU 3D-printed textiles under shear stress. Thus, exhibiting no observable effect on directional variation in warp and weft directions.

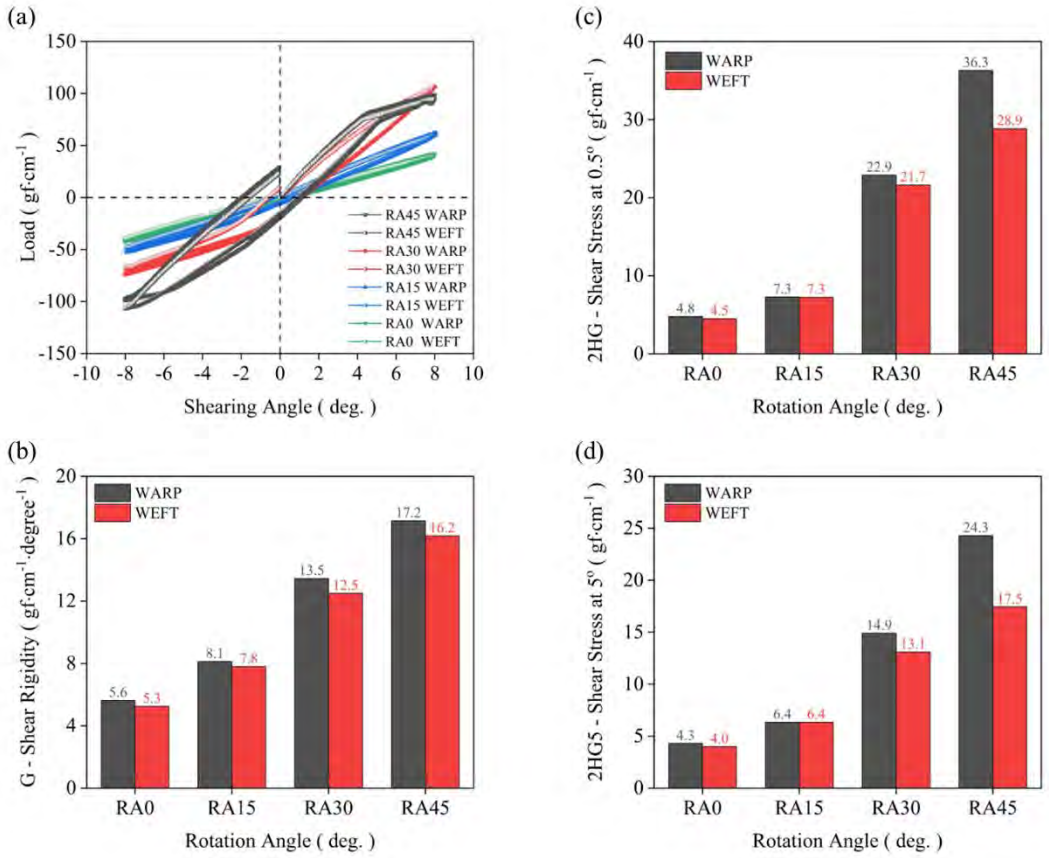

Figure 7.9. Shear properties of RA0, RA15, RA30, and RA45 in warp and weft directions: (a) load-Shear angle curves; (b) G, shear rigidity; (c) 2HG, shear stress at 0.5º; (d) 2HG5, shear stress at 5º.

7.3.3.3 Bending properties

To evaluate rotation angle effects on bending properties of rTPU 3D-printed textiles, rotation angles of the textiles were set to 0º, 15º, 30º, and 45º (designated RA0, RA15, RA30, and RA45). Fig. 7.10a illustrates the curves of the textiles under the applied moment of force. As the RA increased, the curves exhibited a decrease in M with lower slopes and bending rigidity (B) (Fig. 7.10b). The low slope and bending rigidity indicated that the textiles easily bent under low moments of force, becoming flexible. This enhanced flexibility was attributable to the increased deformation of the

unit and reduced strain on the 45º-rotated lines during unit out-plane bending at the same curvature. Simultaneously, the reduction in strain on lines for resiling decreased the bending moment (2HB) at 0.5 cm^{-1} (Fig. 7.10c). The textiles exhibited similar bending properties in the warp and weft directions, which was attributable to the symmetry of the textile structure. The symmetrical structure allowed the printed lines to deform similarly under the same loading conditions in both directions. Thus, the RA0, RA15, RA30, and RA45 exhibited similar M–K curves, B, and 2HB in both directions. In consideration of the results, the increase in RA up to 45º enhanced the flexibility and maintained the high bending resilience of the rTPU 3D-printed textile. Thus, exhibiting no observable effect on directional variation in warp and weft directions.

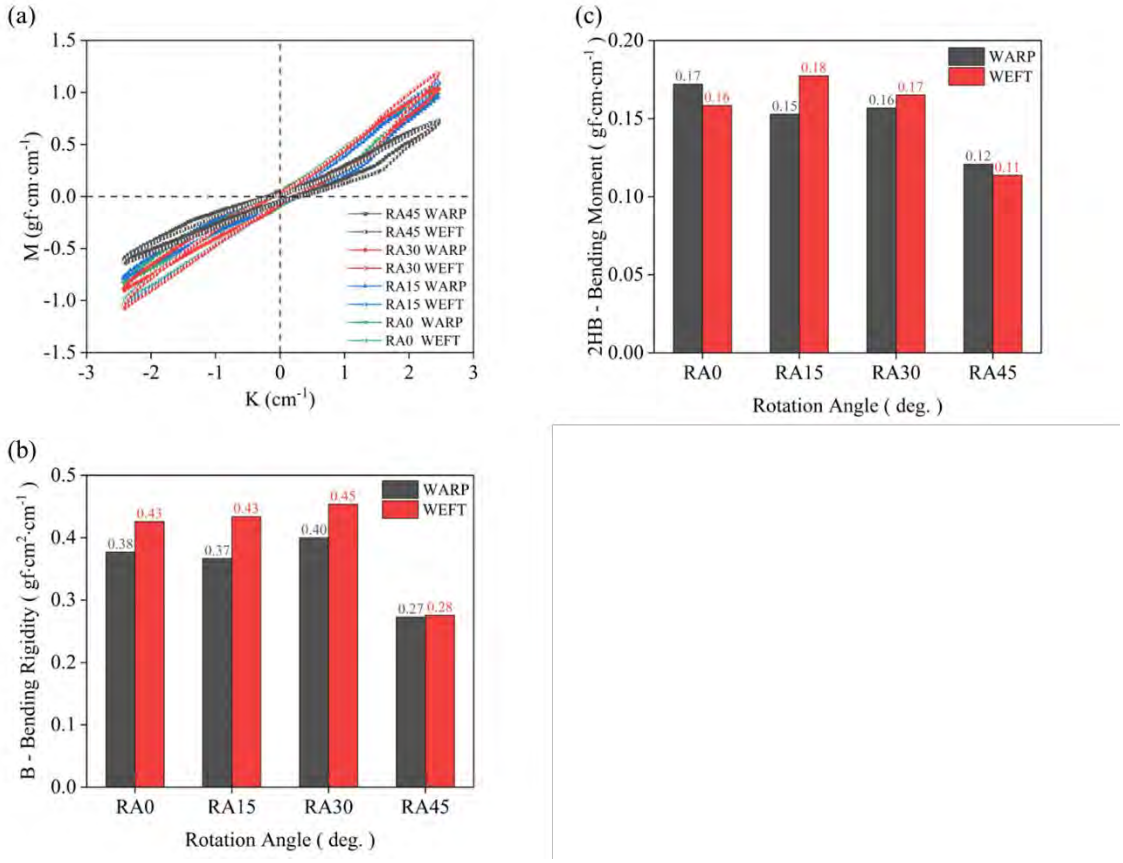

Figure 7.10. Bending properties of RA0, RA15, RA30, and RA45 in warp and weft

directions: (a) M-K curves; (b) B, bending rigidity; (c) 2HB, bending moment at 0.5 cm^{-1}.

7.3.3.4 Compressive properties

To evaluate rotation angle effects on compressive properties of rTPU 3D-printed textiles, rotation angles of the textiles were set to 0º, 15º, 30º, and 45º (designated RA0, RA15, RA30, and RA45). Given that the testing area of clamps is a circle, compression testing lacked directionality. Therefore, the rotation of structures in the textile plane made no difference in compression tests. Compressional linearity (LC), compressional energy (WC), compressional resilience (RC), and fabric thickness (T_0) at 0.5 $gf \cdot cm^{-2}$, remained consistent across textiles with different rotation angles (Fig. 7.11a–d). Moreover, the textiles were 3D-printed with high quality, resulting in low deviation in T_0 due to the high quality of rTPU filaments. Thus, based on the results, the rotation angle exerted no effects on the compressibility of the textile, and the minimal deviation in T_0 demonstrated the high 3D printing quality of rTPU textiles.

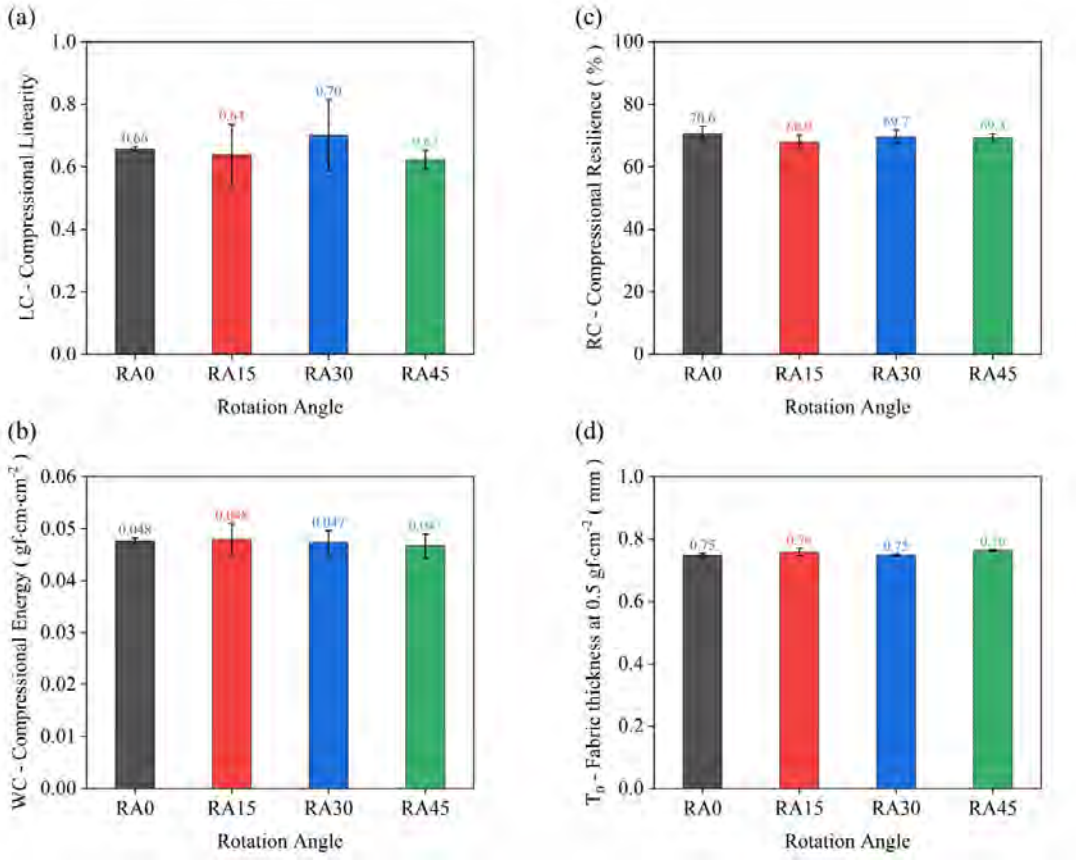

Figure 7.11. Compressive properties of RA0, RA15, RA30, and RA45: (a) LC, compression linearity; (b) WC, compressional energy; (c) RC, compressional resilience; (d) T_0, Fabric thickness at 0.5 gf·cm^{-2}.

7.3.4 Layer number effect on rTPU textiles

7.3.4.1 Tensile properties

To evaluate layer number effects on tensile properties of rTPU 3D-printed textiles, the layer number of the textiles was set to 2, 3, and 4 (designated LN2, LN3, and LN4). Figure 7.12a resents the curves of the textiles subjected to uniaxial force. As the layer numbers decreased, the curves exhibited a tilt toward higher strain with lower slopes and higher EMT values (Fig. 7.12b). The low slope and high EMT indicated that the textiles stretched further under the maximum load, displaying

enhanced elasticity. The reduction in lines within the cross-section elucidated the higher elasticity observed in LN2. In consideration of the low layer number, fewer layers with fewer lines were printed in LN2. Consequently, these lines experienced higher stress and exhibited significant deformation during the stretching of LN2. Accordingly, the textile elasticity increased with the decrease in layer number, owing to the presence of fewer printed lines. Simultaneously, the growing elasticity increased the tensile energy (WT) in LN2, considering that higher elasticity consumed more energy during stretching (Fig. 7.12c). The tensile resilience (RT) of rTPU textiles increased with higher layer numbers, which was attributable to the reduced strain in lines during the short period of tension (Fig. 7.12d). LN2 and LN4 exhibited similar tensile properties in the warp and weft directions, reflecting the symmetry of the textile structure. This symmetry allowed the printed lines to deform uniformly under the same loadings in both directions. However, the difference between the two directions increased in LN3, owing to the odd layer number. The odd layer number resulted in an uneven number of layers (-45º and 45º), leading to structural imbalances and asymmetry in textiles. Thus, LN3 exhibited distinct tensile properties in warp and weft directions. However, the LN2 and LN4 exhibited similar load-strain curves, EMT, RT, and WT in both directions, but they were slightly different in both directions of LN3. In consideration of these results, reducing the layer number decreased the modulus and improved the elasticity of the rTPU 3D-printed textile. Thus, the odd layer number marginally influenced the directional variation in warp and weft directions.

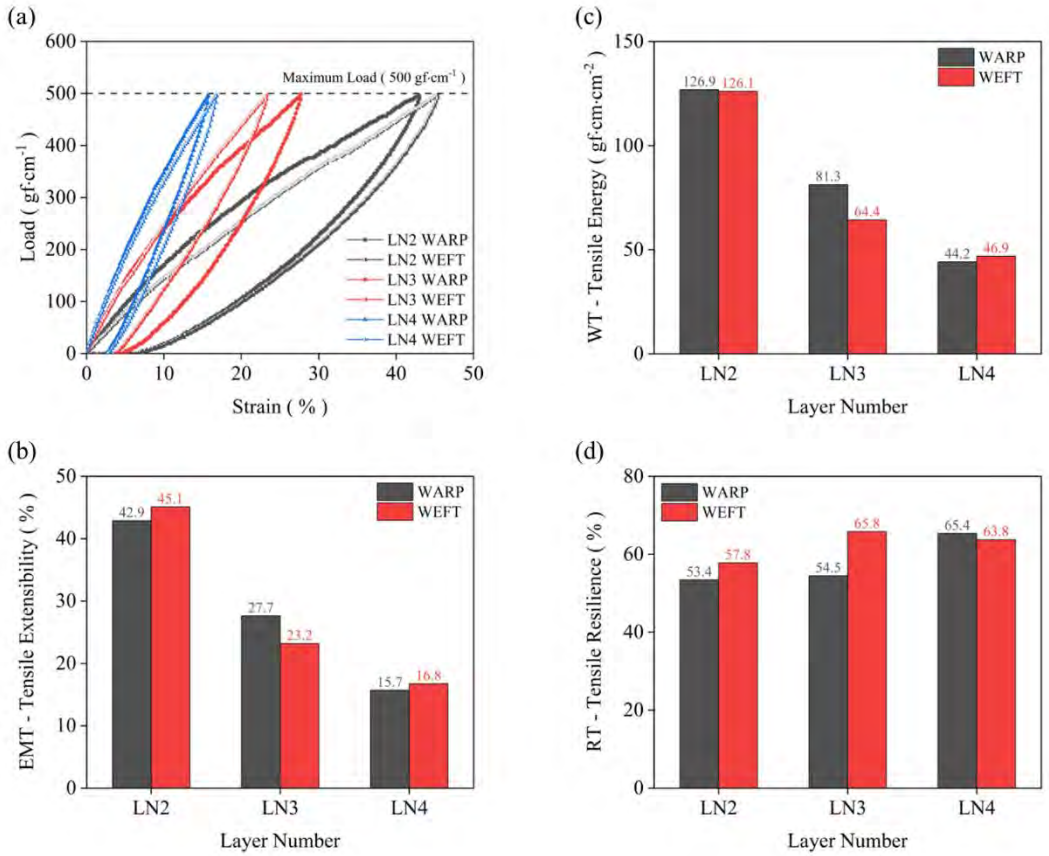

Figure 7.12. Tensile properties of LN2, LN3, and LN4 in warp and weft directions: (a) load-strain curves, (b) EMT, tensile extensibility, (c) WT, tensile energy, and (d) RT, tensile resilience.

7.3.4.2 Shear properties

To evaluate layer number effects on shear properties of rTPU 3D-printed textiles, the layer number of the textiles was set to 2, 3, and 4 (designated LN2, LN3, and LN4). Fig. 7.13a illustrates the curves of the textiles under shear stress. As the layer number increased, the curves exhibited higher stress levels with higher G values (Fig. 7.13b). The heightened G value suggests that the textiles exhibited increased shear resistance and became less prone to deformation with a higher number of layers. The increase in adhered and netted lines elucidated the higher rigidity observed in LN4.

Furthermore, considering the high layer number, more lines were printed in LN4. These netted lines exhibited greater stress in the shear direction at the same deformation. Accordingly, the slope of the load-shear angle curve, as well as G, increased with the increasing layer number. Simultaneously, the increasing rigidity led to increased 2HG at 0.5º and 2HG5 at 5º values in LN4 because the higher rigidity resisted more shear stress at the same deformation and shear angle. Moreover, the heightened shear rigidity led to yielding in the textiles due to the out-plane deformation. Bulges with a consistent spacing formed on the textiles as they began to yield in response to high shear deformation. Thus, reducing the slope of shearing stress at the high shear angle, limiting the increase of the 2HG5 value. The LN2 and LN4 exhibited similar shear properties in warp and weft directions, owing to the symmetry of the textile structure. The symmetry ensured consistent deformation of printed lines under identical shear stress in both directions. However, LN3 exhibited origin-symmetry load-shear angle curves of shear properties with similar values in G, 2HG, and 2HG5 in both directions due to its odd layer number with unbalanced lines in -45º and 45º. Thus, the LN2 and LN4 exhibited similar load-shear angle curves, G, 2HG, and 2HG5 in both directions, while the curves differed in both directions of LN3. Upon considering the results, increasing the layer number increased the shear rigidity of the rTPU 3D-printed textile. Additionally, the odd layer number exhibited origin-symmetry load-shear angle curves of shear properties with similar values in G, 2HG, and 2HG5 in warp and weft directions.

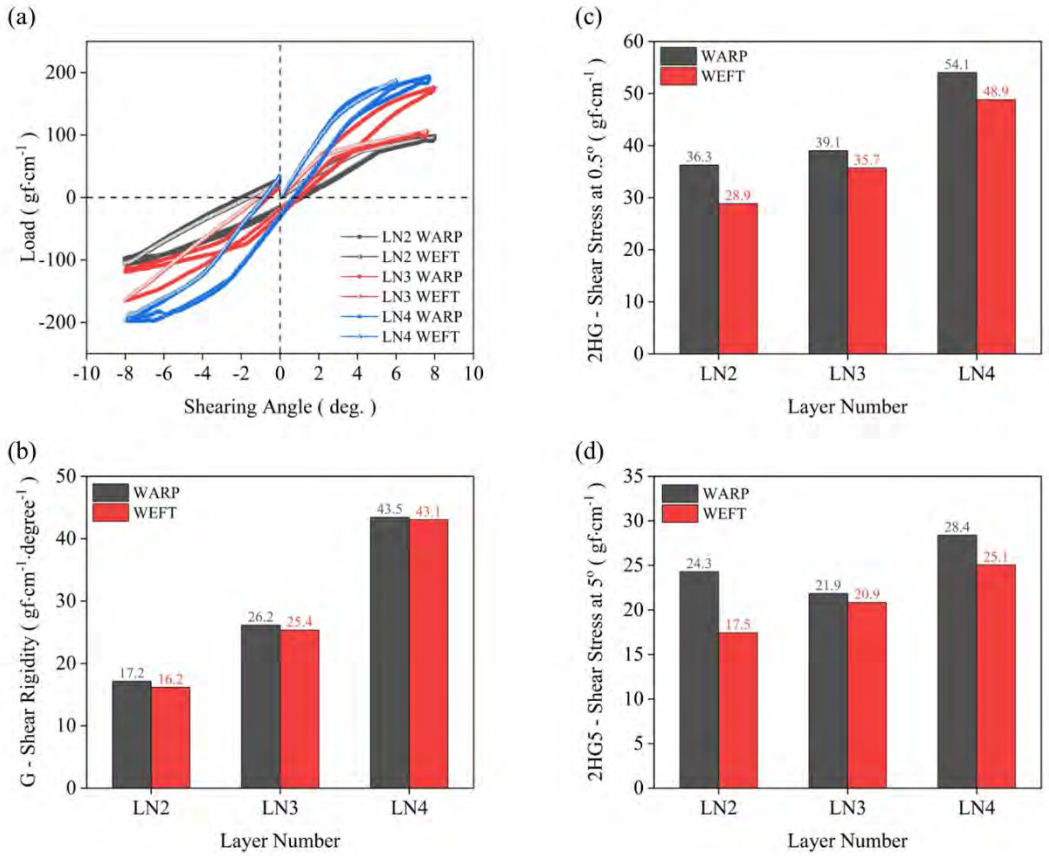

Figure 7.13. Shear properties of LN2, LN3, and LN4 in warp and weft directions: (a) load-Shear angle curves; (b) G, shear rigidity; (c) 2HG, shear stress at 0.5º; (d) 2HG5, shear stress at 5º.

7.3.4.3 Bending properties

To evaluate layer number effects on bending properties of rTPU 3D-printed textiles, the layer numbers of the textiles were set to 2, 3, and 4 (designated LN2, LN3, and LN4). Fig. 7.14a illustrates the curves of the textiles under the moment of force. As the layer decreased, the curves tilted toward lower M values with reduced slopes and increased B values (Fig. 7.14b). The low slope and increased B values indicated that the textiles bent easily under low moments of force, becoming more flexible. The increased flexibility in LN2 was attributable to the reduced number of

lines in the cross-section could As the layer number reduced, few layers with few lines were printed in LN2. Consequently, these lines resisted less stress while being bent into the same curvature K. As the maximum M reached 5 gf·cm·cm $^{-1}$, both LN3 and LN4 reached the maximum M and returned before reaching the maximum K. Simultaneously, the 2HB at 0.5 cm^{-1}, increased significantly from LN2 to LN3 but slightly from LN3 to LN4 (Fig. 7.14c). The difference in increasing speed indicated that the rigidity of LN3 was attributable to the high bending resilience of rTPU. Furthermore, with increased rigidity, rTPU yielded slightly, releasing its internal stress to generate additional strain. However, this strain could not recover within a short period, leading to an increase in 2HB. Both LN2 and LN4 exhibited similar bending properties in warp and weft directions, attributable to the symmetry of the textile structure. The symmetrical structures ensured that printed lines deformed slightly under the same loadings in both directions. Meanwhile, the asymmetrical structure of LN3 did not affect the bending properties. Thus, the LN2, LN3, and LN4 displayed similar M–K curves, B, and 2HB in both directions. Conclusively, reducing the layer number increased the flexibility and maintained the high bending resilience of the rTPU 3D-printed textile, with no effect on the directional variation in warp and weft.

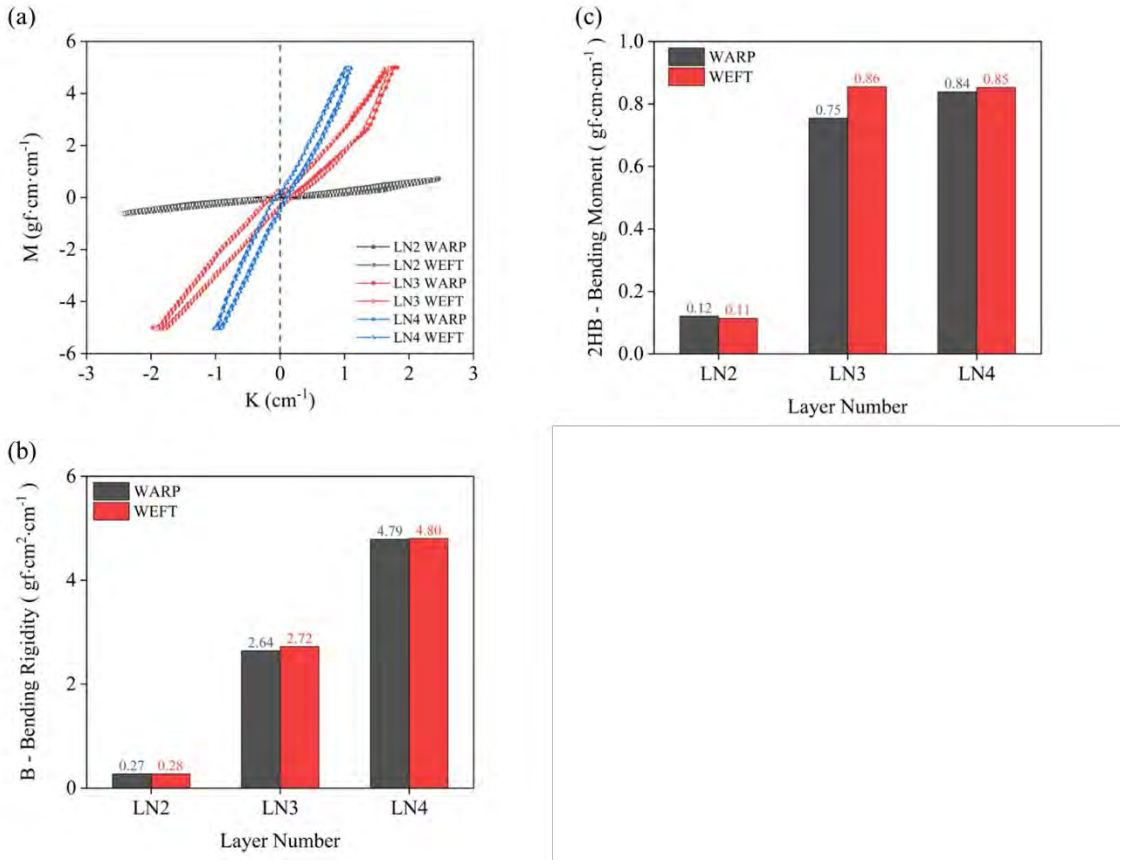

Figure 7.14. Bending properties of LN2, LN3, and LN4 in warp and weft directions: (a) M-K curves; (b) B, bending rigidity; (c) 2HB, bending moment at 0.5 cm^{-1}.

7.3.4.4 Compressive properties

To evaluate layer number effects on compressive properties of rTPU 3D-printed textiles, the layer numbers of the textiles were set to 2, 3, and 4 (designated LN2, LN3, and LN4). The LC decreased from LN2 to LN4, indicating a reduction in the compressibility of textiles with an increasing layer number (Fig. 7.7a). The decrease in compressibility was due to the addition of more layers and lines, resulting in a decreased strain under the same compressive load. However, the WC increase in LN4 was attributable to the presence of additional layers creating voids (Fig. 7.15b). These voids between the layers caused higher strains under lower stress levels, leading to an

increase in WC and further contributing to the reduction of LC in LN4. In Figure 7.15c, the RC of textiles increased slightly, attributable to the low strain under high-stress conditions inherent in rTPU resilience. Furthermore, T_0 at 0.5 gf·cm^{-2}, increased with an increase in the layer number. The low deviation of T_0 indicated that the textiles exhibited high-quality 3D printing, ensuring a consistent thickness across the three testing points. In consideration of the results, decreasing the layer number increased the compressibility of the textiles, while the low T_0 deviation demonstrated the high 3D printing quality of rTPU textiles.

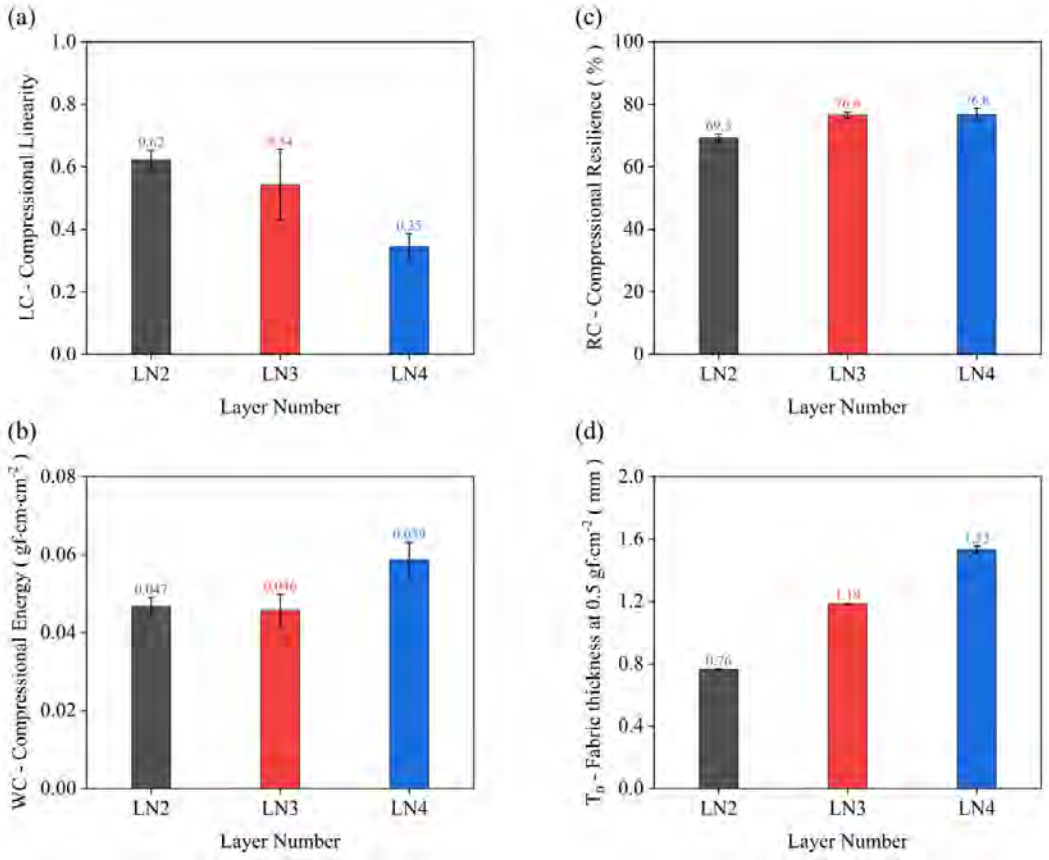

Figure 7.15. Compressive properties of LN2, LN3, and LN4: (a) LC, compression linearity; (b) WC, compressional energy; (c) RC, compressional resilience; (d) T_0, Fabric thickness at 0.5 gf·cm^{-2}.

7.4 Summary

The infill density, rotation angle, and layer number are exerted to control the flexibility of rTPU 3D-printed textiles, ranging from flexible to rigid. Low infill density enhanced flexibility in tensile, shear, bending, and compressive properties due to the fewer lines present in the textiles. This concentrated stress distribution resulted in more deformation under the same loads, yielding higher flexibility. The 45º rotation angle increased the flexibility in tension and bending due to the enhanced deformation of the minimum repeat unit with less strain on lines. Under the same strain, the RA45 exhibited increased unit deformation and less strain on the lines, thereby reducing the stress resistance and enhancing flexibility. However, the shear flexibility of RA45 decreased due to the heightened tensile deformation of units. Low layer numbers enhanced flexibility in the aforementioned properties by concentrating stress and increasing deformation under the same load. Accordingly, low infill density, a 45º rotation angle, and low layer numbers enhanced the heightened flexibility of rTPU textiles.

Chapter 8. Conclusions and Suggestions for Future Research

This chapter concludes the study of the novel approach to recycling thermoplastics from PCTW into 3D-printed products and makes the plan for further research. It includes the conclusions and suggestions for future research. The conclusions summarize all previous chapters to address the research objectives. The limitation of preliminary research is identified as a useful direction for future research.

8.1 Conclusions

8.1.1 Filament production recycled from polyester textiles

To increase the recycling rate of polyester textiles, this study has introduced a high value-added approach to recycling polyester textiles into 3D-printable materials. Polyester textile is modified by adding ADR 4468. This additive extends and crosslinks the PET chains, owing to the ring-opening reaction of the epoxy groups of ADR 4468. This reaction increases the elasticity of polyester melt, thus preventing melt dropping behavior at the end of the extrusion tip, which improves the flow of the filament extrusion. Moreover, the rPET/ADR 4468-1.0 wt% sample has optimal tensile and compressive properties. Its high mechanical performance could be attributed to fewer voids, extension of a fish-scale morphology, and good crystallization. Remarkably, internal compressive residual stress is found in the rPET/ADR 4468-2.0 wt% sample, which accounts for its high tensile properties with

low compressive properties. The residual stress reduces the complex viscosity in the area with low ω values (10^{-1} to 10^{0}), which allows more polymer melt to flow through the nozzle of the 3D printer to fill the printed area, thus reducing the number of voids and improving the mechanical performance. The internal compressive residual stress facilitates the potential application of using rPET/ADR 4468-2.0 wt% for using thermal energy to relax the residual stress for deformation to take place. With the development of the polyester textile recycling process and advances in the 3D-printing industry, this filament production approach is likely able to reduce energy and materials use, increase the recycling ratio, and reduce the environmental load of polyester-based textile waste.

8.1.2 Filament production recycled from TPU films

The MDI-polyester-based rTPU filament can be directly produced by TPU films without additional additives, which suggests that the material of the TPU film has high filament extrusion processability and is suitable for mechanical recycling. The high elongation at break of the 3D-printed products demonstrates the elasticity of rTPU still has attractive elastic properties with high competitiveness after recycling and 3D printing processes. The similar FTIR and DSC results of the TPU film and TPU 3D-printed samples also demonstrate their thermal stability to maintain their chemical structures stable during filament extrusion and 3D printing. Additionally, the 3D-printed samples using 48-hour-dried TPU filament presented higher tensile strength and lower standard deviation with undried filament. Therefore, drying the

filament before 3D printing can improve the mechanical performance and quality of the rTPU 3D-printed products. Additionally, the small voids between the printed lines (SEM results) support the high quality of the rTPU 3D-printed products using dried filaments. Thus, the TPU film is suitable for mechanical recycling into filaments for 3D printing, while the filament drying process can further improve the mechanical performance and quality of the rTPU 3D-printed products. Moreover, the high competitiveness of the soft rTPU 3D-printed products can stimulate the recycling of TPU films from post-consumer textile waste, saving material resources and reducing the environmental load of waste disposal.

8.1.3 3D-printed textiles using the rPET/ADR4468 filament

The infill density, rotation angle, and intersection angle would control the flexibility of rPET/ADR4468 3D-printed textiles from flexible to rigid even formed anisotropy of mechanical properties in warp and weft directions. The low infill density enhanced the flexibility in the tensile, shear, bending, and compressive properties due to the fewer lines in the textiles. The fewer lines would concentrate the stress and have more deformation under the same loads to exhibit higher flexibility of textiles. The 30º and 45º of rotation angle increased the flexibility in tension due to the deformation increasing of minimum repeat unit with less strain on lines. Under the same strain, the RA30 and RA45 tended to have more deformation on units and less strain on the lines in the tensile direction, reducing the stress resistance to perform higher flexibility. In shear, the high flexibility of RA45 was attributed to the great

yielding with out-of-plane deformation. The low intersection angle enhanced the flexibility greatly in weft direction and increased the rigidity greatly in warp direction, which formed an anisotropy of flexibility in two directions of textiles. The anisotropy could be attributed to structure changes in the units. With the intersection angle decreasing, in weft direction, the diagonal was shortened to increase the number of units, which meant that the textile deformation was allocated into smaller deformation for each unit. The smaller deformation reduced the strain of lines and materials to resist lower loading. Since the line numbers of IA30, IA60, and IA90 were the same in the testing area, the less strain of each line would greatly improve the flexibility of IA30 in weft direction. Accordingly, the low infill density, 30º and 45º of rotation angle, and low intersection angle enhanced the flexibility of rPET/ADR4468 textiles.

8.1.4 3D-printed textiles using the rTPU filament

The infill density, rotation angle, and layer number would control the flexibility of rTPU 3D-printed textiles from flexible to rigid. The low infill density enhanced the flexibility in the tensile, shear, bending, and compressive properties due to the fewer lines in the textiles. The fewer lines would concentrate the stress and have more deformation under the same loads to exhibit higher flexibility of textiles. The 45º of rotation angle increased the flexibility in tension and bending due to the deformation increasing of minimum repeat unit with less strain on lines. Under the same strain, the RA45 tended to have more deformation on units and less strain on the lines in the tension and bending, reducing the stress resistance to perform higher flexibility.

However, the shear flexibility of RA45 reduced due to the more tensile deformation of units. The low layer number enhanced the flexibility in the tensile, shear, bending, and compressive properties due to the fewer layers with fewer lines in the textiles. The fewer lines would concentrate the stress and have more deformation under the same loads to exhibit higher flexibility of textiles. Accordingly, low infill density, 45º of rotation angle, and low layer number enhanced the flexibility of rTPU textiles.

8.2 Suggestions for future research

In this study, the processes of recycling polyester textiles and TPU films into 3D-printable filaments for 3D-printed textiles were optimized and applied to fabricate sustainable printable filaments from PCTW for novel 3D-printed flexible textiles. The optimizations improve the mechanical properties of the 3D-printed materials using the filaments. The flexibility of the 3D-printed textiles was enhanced by changing the textile parameters, including infill density, rotation angle, intersection angle, and layer number. With the development of this approach, increasing research problems were encountered, limiting the application of this approach. The following suggestions might further solve the application problems of this approach in the future.

(1) Blended textiles widely used in clothing increase the accumulation of blended textile waste kept for further recycling. The polyester-based blended textiles might be recycled using the recycling approach in this study. The blended textile can be folded with various textiles to control polyester contents, heat-pressed into composite boards, and ground with additives for further extrusion of 3D-printable

filaments. These methods will prevent the separation of polyester and blended other fibers, simplify the recycling processes, and even produce powder- or fiber-reinforced polyester materials for 3D-printable filaments. Suitable additives need to be selected for recycling polyester textiles and enhancing the interfaces of polyester and other components. The TPU-based blended textiles can also be recycled using the approach, which needs a novel grinding method for elastic materials.

(2) The approach can be used for other thermoplastic textiles because the thermoplastics from PCTW are almost designed to fabricate fibers with high flowability of polymer melts. More compatible chain extenders can be investigated to reduce the flowability for the extrusion of 3D-printable filaments, providing more sustainable 3D-printable filaments for FDM 3D printing and further increasing the recycling rate of thermoplastics from PCTW.

(3) There are many other parameters that can change the mechanical properties of 3D-printed textiles. The textile structures can be program-generated by setting various infill parameters, including patterns, densities, and directions. These parameters can change the textile structures and the mechanical properties of the textiles for further applications. Different textiles can be printed with aesthetic and functional patterns.

References

1. Krishnanand; Soni, S.; Taufik, M., Design and assembly of fused filament fabrication (FFF) 3D printers. *Materials Today: Proceedings* **2021,** *46*, 5233-5241.

2. Bekas, D. G.; Hou, Y.; Liu, Y.; Panesar, A., 3D printing to enable multifunctionality in polymer-based composites: A review. *Composites Part B: Engineering* **2019,** *179*, 107540.

3. Rayna, T.; Striukova, L., From rapid prototyping to home fabrication: How 3D printing is changing business model innovation. *Technological Forecasting and Social Change* **2016,** *102*, 214-224.

4. Khabia, S.; Jain, K., Comparison of mechanical properties of components 3D printed from different brand ABS filament on different FDM printers. *Materials Today: Proceedings* **2020,** *26*, 2907-2914.

5. Savi, M.; Andrade, M. A.; Potiens, M. P., Commercial filament testing for use in 3D printed phantoms. *Radiation Physics and Chemistry* **2020,** *174*, 108906.

6. Lin, X.; Gao, J.; Wang, J.; Wang, R.; Gong, M.; Zhang, L.; Lu, Y.; Wang, D.; Zhang, L., Desktop printing of 3D thermoplastic polyurethane parts with enhanced mechanical performance using filaments with varying stiffness. *Additive Manufacturing* **2021,** *47*, 102267.

7. Andronov, V.; Beránek, L.; Krůta, V.; Hlavůňková, L.; Jeníková, Z., Overview and Comparison of PLA Filaments Commercially Available in Europe for FFF Technology. *Polymers* **2023,** *15* (14), 3065.

8. Silva, A.; Carneiro, O.; Gomes, R. In *3D printing of polypropylene using the fused filament fabrication technique*, AIP Conference Proceedings, AIP Publishing: 2017.

9. Woern, A. L.; Byard, D. J.; Oakley, R. B.; Fiedler, M. J.; Snabes, S. L.; Pearce, J. M., Fused Particle Fabrication 3-D Printing: Recycled Materials' Optimization and Mechanical Properties. *Materials (Basel)* **2018,** *11* (8), 1413.

10. Reich, M. J.; Woern, A. L.; Tanikella, N. G.; Pearce, J. M., Mechanical Properties and Applications of Recycled Polycarbonate Particle Material Extrusion-Based Additive Manufacturing. *Materials (Basel)* **2019,** *12* (10), 1642.

11. Peeters, B.; Kiratli, N.; Semeijn, J., A barrier analysis for distributed recycling of 3D printing waste: Taking the maker movement perspective. *Journal of Cleaner Production* **2019,** *241*, 118313.

12. Woern, A. L.; McCaslin, J. R.; Pringle, A. M.; Pearce, J. M., RepRapable Recyclebot: Open source 3-D printable extruder for converting plastic to 3-D printing filament. *HardwareX* **2018,** *4*, 00026.

13. Zander, N. E.; Gillan, M.; Lambeth, R. H., Recycled polyethylene terephthalate as a new FFF feedstock material. *Additive Manufacturing* **2018,** *21*, 174-182.

14. Hart, K. R.; Frketic, J. B.; Brown, J. R., Recycling meal-ready-to-eat (MRE) pouches into polymer filament for material extrusion additive manufacturing. *Additive Manufacturing* **2018,** *21*, 536-543.

15. Zander, N. E.; Gillan, M.; Burckhard, Z.; Gardea, F., Recycled polypropylene blends as novel 3D printing materials. *Additive Manufacturing* **2019,** *25*, 122-130.

16. Vettese Forster, S., 3D Printable Recycled Textiles: Material Innovation and a

Resurrection of the Forgotten “shoddy” Industry. *Journal of Textile Design Research and Practice* **2018,** *5* (2), 138-156.

17. Maldonado-García, B.; Pal, A. K.; Misra, M.; Gregori, S.; Mohanty, A. K., Sustainable 3D printed composites from recycled ocean plastics and pyrolyzed soy-hulls: Optimization of printing parameters, performance studies and prototypes development. *Composites Part C: Open Access* **2021,** *6*, 100197.

18. Audi Upcycling at Audi: a new lease on life for packaging. https://www.audi-mediacenter.com/en/press-releases/upcycling-at-audi-a-new-lease-on-life-for-packaging-14185.

19. Olympic TOKOLO Asao: Designer of the victory ceremony podiums and emblem. https://olympics.com/en/news/tokolo-asao-designer-of-the-victory-ceremony-podiums-and-emblem.

20. P&G P&G and Tokyo 2020 Announce The Podium Project – The First-Ever Medals Podiums Created From Recycled Plastic for Upcoming Olympic Games and Paralympic Games. https://news.pg.com/news-releases/news-details/2019/PG-and-Tokyo-2020-Announce-The-Podium-Project--The-First-Ever-Medals-Podiums-Created-From-Recycled-Plastic-for-Upcoming-Olympic-Games-and-Paralympic-Games/default.aspx.

21. Sandin, G.; Peters, G. M., Environmental impact of textile reuse and recycling – A review. *Journal of Cleaner Production* **2018,** *184*, 353-365.

22. Qin, Y.; Sun, H.; Hao, P.; Wang, H.; Wang, C.; Ma, L.; Wei, H.; Yu, S., Transcriptome analysis reveals differences in the mechanisms of fiber initiation and

elongation between long- and short-fiber cotton (Gossypium hirsutum L.) lines. *BMC Genomics* **2019,** *20* (1), 633.

23. Bello, D. C.; Barczak, G. J., Using Industrial Trade Shows to improve New Product Development. *Journal of Business & Industrial Marketing* **1990,** *5* (2), 43-56.

24. Niinimäki, K.; Peters, G.; Dahlbo, H.; Perry, P.; Rissanen, T.; Gwilt, A., The environmental price of fast fashion. *Nature Reviews Earth & Environment* **2020,** *1* (4), 189-200.

25. Degenstein, L. M.; McQueen, R. H.; McNeill, L. S.; Hamlin, R. P.; Wakes, S. J.; Dunn, L. A., Impact of physical condition on disposal and end-of-life extension of clothing. *International Journal of Consumer Studies* **2020,** *44* (6), 586-596.

26. Kozlowski, A.; Bardecki, M.; Searcy, C., Environmental Impacts in the Fashion Industry: A Life-cycle and Stakeholder Framework. **2012,** *45*, 17-36.

27. Laitala, K.; Boks, C., CLOTHING DESIGN FOR SUSTAINABLE USE: Social and technical durability. In *Knowledge Collaboration & Learning for Sustainable Innovation ERSCP-EMSU conference*, 2010.

28. Muthu, S. S.; Li, Y.; Hu, J.-Y.; Mok, P.-Y., Recyclability Potential Index (RPI): The concept and quantification of RPI for textile fibres. *Ecological Indicators* **2012,** *18*, 58-62.

29. MacArthur, E., Beyond plastic waste. *Science* **2017,** *358* (6365), 843.

30. Adrien, B.; Debora, D.; Laura, F.; Thomas, G.; Yannick, L. G.; Marie, D.; Anne, P.; Ines, B.; Oliver, W.; Jiannis, K., Environmental improvement potential of textiles (IMPRO-Textiles). *European Commission* **2014**, EUR 26316 EN.

31. Utebay, B.; Celik, P.; Cay, A., Effects of cotton textile waste properties on recycled fibre quality. *Journal of Cleaner Production* **2019,** *222*, 29-35.

32. Yalcin-Enis, I.; Kucukali-Ozturk, M.; Sezgin, H., Risks and management of textile waste. *Nanoscience and biotechnology for environmental applications* **2019**, 29-53.

33. Khattab, T. A.; Abdelrahman, M. S.; Rehan, M., Textile dyeing industry: environmental impacts and remediation. *Environmental Science and Pollution Research* **2020,** *27*, 3803-3818.

34. Weinmayr, G.; Pedersen, M.; Stafoggia, M.; Andersen, Z. J.; Galassi, C.; Munkenast, J.; Jaensch, A.; Oftedal, B.; Krog, N. H.; Aamodt, G., Particulate matter air pollution components and incidence of cancers of the stomach and the upper aerodigestive tract in the European Study of Cohorts of Air Pollution Effects (ESCAPE). *Environment international* **2018,** *120*, 163-171.

35. Nørup, N.; Pihl, K.; Damgaard, A.; Scheutz, C., Evaluation of a European textile sorting centre: Material flow analysis and life cycle inventory. *Resources, Conservation and Recycling* **2019,** *143*, 310-319.

36. PlanetAidUK Clothes Collection. https://www.planetaid-uk.org/what-we-do/fundraising-activites/clothes-collection.

37. Hawley, J., Digging for diamonds: A conceptual framework for understanding reclaimed textile products. **2006,** *24* (3), 262-275.

38. Raheem, A. B.; Noor, Z. Z.; Hassan, A.; Abd Hamid, M. K.; Samsudin, S. A.; Sabeen, A. H., Current developments in chemical recycling of post-consumer polyethylene terephthalate wastes for new materials production: A review. *Journal of*

Cleaner Production **2019,** *225*, 1052-1064.

39. Hoang, C. N.; Dang, Y. H., Aminolysis of poly(ethylene terephthalate) waste with ethylenediamine and characterization of α,ω-diamine products. *Polymer Degradation and Stability* **2013,** *98* (3), 697-708.

40. Sinha, V.; Patel, M. R.; Patel, J. V., Pet Waste Management by Chemical Recycling: A Review. *Journal of Polymers and the Environment* **2008,** *18* (1), 8-25.

41. Abdullah, N. M.; Ahmad, I., Potential of using polyester reinforced coconut fiber composites derived from recycling polyethylene terephthalate (PET) waste. *Fibers and Polymers* **2013,** *14* (4), 584-590.

42. Ramamoorthy, S. K.; Persson, A.; Skrifvars, M., Reusing textile waste as reinforcements in composites. *Journal of Applied Polymer Science* **2014,** *131* (17).

43. Ahmed, H. U.; Faraj, R. H.; Hilal, N.; Mohammed, A. A.; Sherwani, A. F. H., Use of recycled fibers in concrete composites: A systematic comprehensive review. *Composites Part B: Engineering* **2021,** *215*, 108769.

44. Yousef, S.; Tatariants, M.; Tichonovas, M.; Kliucininkas, L.; Lukošiūtė, S.-I.; Yan, L., Sustainable green technology for recovery of cotton fibers and polyester from textile waste. *Journal of Cleaner Production* **2020,** *254*, 120078.

45. Lee, J. H.; Lim, K. S.; Hahm, W. G.; Kim, S. H., Properties of recycled and virgin poly(ethylene terephthalate) blend fibers. *Journal of Applied Polymer Science* **2013,** *128* (2), 1250-1256.

46. Singh, A. K.; Bedi, R.; Kaith, B. S., Composite materials based on recycled polyethylene terephthalate and their properties – A comprehensive review. *Composites*

Part B: Engineering **2021,** *219*, 108928.

47. Scelsi, L.; Hodzic, A.; Soutis, C.; Hayes, S. A.; Rajendran, S.; AlMa'adeed, M. A.; Kahraman, R., A review on composite materials based on recycled thermoplastics and glass fibres. *Plastics, Rubber and Composites* **2013,** *40* (1), 1-10.

48. Baek, Y.-M.; Shin, P.-S.; Kim, J.-H.; Park, H.-S.; Kwon, D.-J.; DeVries, K. L.; Park, J.-M., Investigation of Interfacial and Mechanical Properties of Various Thermally-Recycled Carbon Fibers/Recycled PET Composites. *Fibers and Polymers* **2018,** *19* (8), 1767-1775.

49. Dairi, B.; Djidjelli, H.; Boukerrou, A.; Migneault, S.; Koubaa, A., Morphological, mechanical, and physical properties of composites made with wood flour-reinforced polypropylene/recycled poly(ethylene terephthalate) blends. *Polymer Composites* **2017,** *38* (8), 1749-1755.

50. Thumsorn, S.; Yamada, K.; Leong, Y. W.; Hamada, H., Thermal decomposition kinetic and flame retardancy of CaCO3filled recycled polyethylene terephthalate/recycled polypropylene blend. *Journal of Applied Polymer Science* **2013,** *127* (2), 1245-1256.

51. Sharma, A. K.; Mahanwar, P. A., Effect of particle size of fly ash on recycled poly (ethylene terephthalate) / fly ash composites. *International Journal of Plastics Technology* **2010,** *14* (1), 53-64.

52. Yang, B.; Chen, J.; Su, L.-F.; Miao, J.-B.; Chen, P.; Qian, J.-S.; Xia, R.; Shi, Y., Melt crystallization and thermal properties of graphene platelets (GNPs) modified recycled polyethylene terephthalate (RPET) composites: The filler network analysis.

Polymer Testing **2019,** *77*, 105869.

53. Pires, H. M.; Mendes, L. C.; Cestari, S. P.; Cucinelli Neto, R. P.; Rodrigues, D. C.; Mattos, G. C., nZnO as Barrier to Ultraviolet Radiation on rPET/PC Nanocomposites. *Journal of Nanoscience and Nanotechnology* **2016,** *16* (9), 9987-9996.

54. Gopalan, A. M.; Naskar, K., Ultra-high molecular weight styrenic block copolymer/TPU blends for automotive applications: Influence of various compatibilizers. *Polymers for Advanced Technologies* **2019,** *30* (3), 608-619.

55. Johnson, L.; Samms, J., Thermoplastic polyurethane technologies for the textile industry. *Journal of coated fabrics* **1997,** *27* (1), 48-62.

56. Lambertz, A.; Vogels, R. R.; Binnebösel, M.; Schöb, D. S.; Kossel, K.; Klinge, U.; Neumann, U. P.; Klink, C. D., Elastic mesh with thermoplastic polyurethane filaments preserves effective porosity of textile implants. *Journal of Biomedical Materials Research Part A* **2015,** *103* (8), 2654-2660.

57. Mistry, P.; Chhabra, R.; Muke, S.; Narvekar, A.; Sathaye, S.; Jain, R.; Dandekar, P., Fabrication and characterization of starch-TPU based nanofibers for wound healing applications. *Materials Science and Engineering: C* **2021,** *119*, 111316.

58. Mishra, A.; Aswal, V. K.; Maiti, P., Nanostructure to microstructure self-assembly of aliphatic polyurethanes: the effect on mechanical properties. *J Phys Chem B* **2010,** *114* (16), 5292-300.

59. Schneider, N. S.; Sung, C. S. P.; Matton, R. W.; Illinger, J. L., Thermal Transition Behavior of Polyurethanes Based on Toluene Diisocyanate. *Macromolecules* **2002,** *8*

(1), 62-67.

60. Brunette, C. M.; Hsu, S. L.; MacKnight, W. J., Hydrogen-bonding properties of hard-segment model compounds in polyurethane block copolymers. *Macromolecules* **2002,** *15* (1), 71-77.

61. Hentschel, T.; Münstedt, H., Kinetics of the molar mass decrease in a polyurethane melt: a rheological study. *Polymer* **2001,** *42* (7), 3195-3203.

62. Kwiatkowski, K.; Nachman, M., The Abrasive Wear Resistance of the Segmented Linear Polyurethane Elastomers Based on a Variety of Polyols as Soft Segments. *Polymers (Basel)* **2017,** *9* (12).

63. Yanagihara, Y.; Osaka, N.; Murayama, S.; Saito, H., Thermal annealing behavior and structure development of crystalline hard segment domain in a melt-quenched thermoplastic polyurethane. *Polymer* **2013,** *54* (8), 2183-2189.

64. Kemona, A.; Piotrowska, M., Polyurethane Recycling and Disposal: Methods and Prospects. *Polymers (Basel)* **2020,** *12* (8).

65. Simon, D.; Borreguero, A. M.; de Lucas, A.; Rodriguez, J. F., Recycling of polyurethanes from laboratory to industry, a journey towards the sustainability. *Waste Manag* **2018,** *76*, 147-171.

66. Kanaya, K.; Takahashi, S., Decomposition of polyurethane foams by alkanolamines. *Journal of Applied Polymer Science* **1994,** *51* (4), 675-682.

67. Wang, X.; Chen, H.; Chen, C.; Li, H., Chemical degradation of thermoplastic polyurethane for recycling polyether polyol. *Fibers and Polymers* **2011,** *12* (7), 857-863.

68. Wolfel, B.; Seefried, A.; Allen, V.; Kaschta, J.; Holmes, C.; Schubert, D. W., Recycling and Reprocessing of Thermoplastic Polyurethane Materials towards Nonwoven Processing. *Polymers (Basel)* **2020,** *12* (9).

69. Kunchimon, S. Z.; Tausif, M.; Goswami, P.; Cheung, V., Polyamide 6 and thermoplastic polyurethane recycled hybrid Fibres via twin-screw melt extrusion. *Journal of Polymer Research* **2019,** *26* (7).

70. Zia, K. M.; Bhatti, H. N.; Ahmad Bhatti, I., Methods for polyurethane and polyurethane composites, recycling and recovery: A review. *Reactive and Functional Polymers* **2007,** *67* (8), 675-692.

71. H&M H&M's autumn 2021 recycled denim collection our most recycled collection to date. https://about.hm.com/news/general-news-2021/h-m-s-autumn-2021-recycled-denim-collection-our-most-recycled-co.html.

72. H&M From old to new with Looop. https://www2.hm.com/en_gb/life/culture/inside-h-m/meet-the-machine-turning-old-into-new.html.

73. Bianchi, S.; Bartoli, F.; Bruni, C.; Fernandez-Avila, C.; Rodriguez-Turienzo, L.; Mellado-Carretero, J.; Spinelli, D.; Coltelli, M.-B., Opportunities and Limitations in Recycling Fossil Polymers from Textiles. *Macromol* **2023,** *3* (2), 120-148.

74. Nike Nike Space Hippie challenges prospects by changing norms. https://news.nike.com/news/space-hippie.

75. Takahashi, H.; Kim, J. In *3D printed fabric: techniques for design and 3D weaving programmable textiles*, Proceedings of the 32nd Annual ACM Symposium on User

Interface Software and Technology, 2019; pp 43-51.

76. Melnikova, R.; Ehrmann, A.; Finsterbusch, K. In *3D printing of textile-based structures by Fused Deposition Modelling (FDM) with different polymer materials*, IOP conference series: materials science and engineering, IOP publishing: 2014; p 012018.

77. Sun, L. In *Daring to Sprint: 3D printing textile*, International Textile and Apparel Association Annual Conference Proceedings, Iowa State University Digital Press: 2017.

78. Grain, E., 3D printing fashion with recycled polyester: A sustainable journey. **2015**.

79. Peleg, D. A 3D-Printed Garment That You Can Buy Online. https://danitpeleg.com/.

80. Nofar, M.; Oğuz, H., Development of PBT/Recycled-PET Blends and the Influence of Using Chain Extender. *Journal of Polymers and the Environment* **2019,** *27* (7), 1404-1417.

81. Piribauer, B.; Bartl, A. J. W. M.; Research, Textile recycling processes, state of the art and current developments: A mini review. **2019,** *37* (2), 112-119.

82. Zhang, Y.; Ying, L.; Wang, Z.; Wang, Y.; Xu, Q.; Li, C., Unexpected hydrophobic to hydrophilic transition of PET fabric treated in a deep eutectic solvent of choline chloride and oxalic acid. *Polymer* **2021,** *234*, 124246.

83. Oh, J.; Kim, S. S.; Kim, K. H.; Lee, J.; Kang, C., Structural and physico-chemical properties change of polyethylene terephthalate (PET) fibers after supercritical fluid dyeing with C.I. disperse red 167. *The Journal of Supercritical Fluids* **2021,** *170*, 105131.

84. Ren, X.; Meng, N.; Zhang, H.; Wu, J.; Abrahams, I.; Yan, H.; Bilotti, E.; Reece,

M. J., Giant energy storage density in PVDF with internal stress engineered polar nanostructures. *Nano Energy* **2020,** *72*, 104662.

85. Simons, W. W., *Sadtler handbook of infrared spectra*. Sadtler Research Laboratories: 1978.

86. Nakayama, D.; Wu, F.; Mohanty, A. K.; Hirai, S.; Misra, M., Biodegradable Composites Developed from PBAT/PLA Binary Blends and Silk Powder: Compatibilization and Performance Evaluation. *ACS Omega* **2018,** *3* (10), 12412-12421.

87. Saeb, M. R.; Bakhshandeh, E.; Khonakdar, H. A.; Mader, E.; Scheffler, C.; Heinrich, G., Cure kinetics of epoxy nanocomposites affected by MWCNTs functionalization: a review. *ScientificWorldJournal* **2013,** *2013*, 703708.

88. McMurry, J., *Organic chemistry*. Ninth edition.. ed.; Boston, MA : Cengage Learning: Boston, MA, 2016.

89. Park, C. K.; Jang, D. J.; Lee, J. H.; Kim, S. H., Toughening of polylactide by in-situ reactive compatibilization with an isosorbide-containing copolyester. *Polymer Testing* **2021,** *95*, 107136.

90. Shangguan, Y.; Zhang, C.; Xie, Y.; Chen, R.; Jin, L.; Zheng, Q., Study on degradation and crosslinking of impact polypropylene copolymer by dynamic rheological measurement. *Polymer* **2010,** *51* (2), 500-506.

91. Takeshita, H.; Shiomi, T.; Takenaka, K.; Arai, F., Crystallization and higher-order structure of multicomponent polymeric systems. *Polymer* **2013,** *54* (18), 4776-4789.

92. Zhao, L.; Yu, Y.; Huang, H.; Yin, X.; Peng, J.; Sun, J.; Huang, L.; Tang, Y.;

Wang, L., High-performance polyphenylene sulfide composites with ultra-high content of glass fiber fabrics. *Composites Part B: Engineering* **2019,** *174*, 106790.

93. Samy, A. A.; Golbang, A.; Harkin-Jones, E.; Archer, E.; Tormey, D.; McIlhagger, A., Finite element analysis of residual stress and warpage in a 3D printed semi-crystalline polymer: Effect of ambient temperature and nozzle speed. *Journal of Manufacturing Processes* **2021,** *70*, 389-399.

94. Sakamoto, N.; Hashimoto, T., Ordering Dynamics of a Symmetric Polystyrene-block-polyisoprene. 2. Real-Space Analysis on the Formation of Lamellar Microdomain. *Macromolecules* **1998,** *31* (12), 3815-3823.

95. Li, L.; Aoki, Y., Rheological Images of Poly(vinyl chloride) Gels. 1. The Dependence of Sol−Gel Transition on Concentation. *Macromolecules* **1997,** *30* (25), 7835-7841.

96. Ji, L. B.; Zhou, T. R., Finite Element Simulation of Temperature Field in Fused Deposition Modeling. *Advanced Materials Research* **2010,** *97-101*, 2585-2588.

97. Li, C.; Liu, J.; Li, J.; Shen, F.; Huang, Q.; Xu, H., Studies of 4,4′-diphenylmethane diisocyanate (MDI)/1,4-butanediol (BDO) based TPUs by in situ and moving-window two-dimensional correlation infrared spectroscopy: Understanding of multiple DSC endotherms from intermolecular interactions and motions level. *Polymer* **2012,** *53* (23), 5423-5435.

98. Boubakri, A.; Elleuch, K.; Guermazi, N.; Ayedi, H., Investigations on hygrothermal aging of thermoplastic polyurethane material. *Materials & Design* **2009,** *30* (10), 3958-3965.

99. Chatterjee, K.; Ghosh, T. K., 3D printing of textiles: potential roadmap to printing with fibers. *Advanced Materials* **2020,** *32* (4), 1902086.

100. Bloomfield, M.; Borstrock, S., Modeclix. The additively manufactured adaptable textile. *Materials Today Communications* **2018,** *16*, 212-216.

101. Ballard, D. H.; Jammalamadaka, U.; Tappa, K.; Weisman, J. A.; Boyer, C. J.; Alexander, J. S.; Woodard, P. K., 3D printing of surgical hernia meshes impregnated with contrast agents: in vitro proof of concept with imaging characteristics on computed tomography. *3D Print Med* **2018,** *4* (1), 13.

102. Cao, W. T.; Ma, C.; Mao, D. S.; Zhang, J.; Ma, M. G.; Chen, F., MXene-Reinforced Cellulose Nanofibril Inks for 3D-Printed Smart Fibres and Textiles. *Advanced Functional Materials* **2019,** *29* (51), 1905898.

103. Chatterjee, K.; Ghosh, T. K., 3D Printing of Textiles: Potential Roadmap to Printing with Fibers. *Adv Mater* **2020,** *32* (4), 1902086.

104. Ding, S.; Zou, B.; Wang, P.; Huang, C.; Liu, J.; Li, L., Geometric modeling and recycling of 3D printed fiber reinforced thermoplastic composite plain weft knitted structures. *Composites Part A: Applied Science and Manufacturing* **2021,** *149*, 106528.

105. Dip, T. M.; Emu, A. S.; Nafiz, M. N. H.; Kundu, P.; Rakhi, H. R.; Sayam, A.; Akhtarujjman, M.; Shoaib, M.; Ahmed, M. S.; Ushno, S. T.; Asheque, A. I.; Hasnat, E.; Uddin, M. A.; Sayem, A. S. M., 3D printing technology for textiles and fashion. *Textile Progress* **2021,** *52* (4), 167-260.

106. Dominguez-Robles, J.; Mancinelli, C.; Mancuso, E.; Garcia-Romero, I.; Gilmore, B. F.; Casettari, L.; Larraneta, E.; Lamprou, D. A., 3D Printing of Drug-

Loaded Thermoplastic Polyurethane Meshes: A Potential Material for Soft Tissue Reinforcement in Vaginal Surgery. *Pharmaceutics* **2020,** *12* (1), 63.

107. Lacey, S. D.; Kirsch, D. J.; Li, Y.; Morgenstern, J. T.; Zarket, B. C.; Yao, Y.; Dai, J.; Garcia, L. Q.; Liu, B.; Gao, T.; Xu, S.; Raghavan, S. R.; Connell, J. W.; Lin, Y.; Hu, L., Extrusion-Based 3D Printing of Hierarchically Porous Advanced Battery Electrodes. *Adv Mater* **2018,** *30* (12), 1705651.

108. Lei, M.; Hong, W.; Zhao, Z.; Hamel, C.; Chen, M.; Lu, H.; Qi, H. J., 3D Printing of Auxetic Metamaterials with Digitally Reprogrammable Shape. *ACS Applied Materials & Interfaces* **2019,** *11* (25), 22768-22776.

109. Sitotaw, D. B.; Ahrendt, D.; Kyosev, Y.; Kabish, A. K., Additive Manufacturing and Textiles—State-of-the-Art. *Applied Sciences* **2020,** *10* (15), 5033.

110. Lee, C. H.; Hong, S. Y. J. 한., A Characteristic Analysis on 3D printing materials for Textiles. **2016,** *24*, 343-350.

111. Zhang, X.; Fan, W.; Liu, T., Fused deposition modeling 3D printing of polyamide-based composites and its applications. *Composites Communications* **2020,** *21*, 100413.